Magnetoconvection at Very Strong Magnetic Fields

by

Ruslan Akhmedagaev

A dissertation submitted in partial fulfillment
of the requirements for the degree of
Doctor of Philosophy
(Mechanical Sciences and Engineering)
in The University of Michigan-Dearborn
2022

Doctoral Committee:

Professor Oleg Zikanov, Chair
Assistant Professor Hugo Casquero Penelas
Professor Subrata Sengupta
Professor Ya Sha Yi

Ruslan Akhmedagaev

rusakhm@umich.edu

ORCID iD: 0000-0001-8798-2462

ACKNOWLEDGEMENTS

I would like to express my deepest appreciation to my advisor Prof. Oleg Zikanov for his invaluable advice, continuous encouragement, and patience during my Ph.D. study. His immense knowledge and vast experience have been a great inspiration for me.

My gratitude extends to Prof. J. Schumacher, Prof. D. Krasnov, Prof. Cheol W. Lee, Prof. Y. Listratov, and Prof. I. Belyaev for providing valuable ideas and treasured support at every stage of this study. I am thankful to Dr. Xuan Zhang for her assistance with the numerical model.

Warmest thanks should also go to the Fluid Mechanics Group at the Technische Universität Ilmenau and to the Department of Thermophysics at National Research University "MPEI" for hospitality during my research stay in Ilmenau and in Moscow, respectively.

I had the pleasure of working with my fellow lab-mates and I am grateful for the enthusiastic discussions and a great time spent together.

Lastly, I would be remiss in not mentioning my family. Their faith in me has kept my spirits and motivation strong.

Thanks for the financial support from US NSF (grant CBET 1803730 ‘Extreme magnetoconvection’).

TABLE OF CONTENTS

LIST OF TABLES

TABLE

LIST OF FIGURES

FIGURE

LIST OF ABBREVIATIONS

FFT fast Fourier transform

DNS direct numerical simulations

RBC Rayleigh-Bénard convection

PRBF Poiseuille-Rayleigh-Bénard flow

LSC large-scale circulation

MCFs magneto-convective fluctuations

MHD magnetohydrodynamics

Q2D quasi-two-dimensional

2D two-dimensional

3D three-dimensional

SEM spectral element method

FVM finite volume method

FDM finite difference method

POD proper orthogonal decomposition

DMD dynamic mode decomposition

ROM reduced-order modelling

ABSTRACT

Magnetoconvection is the type of flows in which the effects of thermal convection and magnetohydrodynamics (MHD) are combined. Magnetoconvection dramatically affects the nature of flows of electrically conducting fluids such as liquid metals and plasmas. This physical phenomenon is investigated in the dissertation for two configurations.

The first is the Rayleigh-Bénard convection (RBC), which plays an important role in numerous systems found in technology and nature. The results are consistent with those of earlier experimental and numerical data. As anticipated, the heat transfer rate and kinetic energy are suppressed by a strong magnetic field. At the same time, their growth with the Rayleigh number is found to be faster in flows at higher values of Hartmann numbers. Exceptionally high values of the Nusselt number are observed in such flows. This behavior is attributed to the newly discovered flow regime that is explored in high-resolution direct numerical simulations (DNS). The regime is characterized by prominent quasi-two-dimensional (Q2D) structures reminiscent of vortex sheets observed earlier in simulations of magnetohydrodynamic turbulence.

Another studied case is the mixed convection in a horizontal duct (Poiseuille-Rayleigh-Bénard flow (PRBF)), in which unique regimes characterized by extreme temperature gradients and high-amplitude fluctuations (the so-called magneto-convective fluctuations (MCFs)) have been recently discovered. DNS and linear stability analysis are carried out to further explore this phenomenon which is relevant to the design of liquid-metal components of future nuclear fusion reactors. Also, the two-dimensional (2D) approximation is validated and applied in the asymptotic limit of a very strong magnetic field effect in

order to investigate the instability in the previously unexplored range of control parameters corresponding to the typical conditions of a liquid metal blanket of a nuclear fusion reactor.

Additionally, the modal analysis of magnetoconvection is performed to seek for an effective low-dimensional representation and retrieve physically dominant features of the fluid flows. The modal decomposition technique provides an efficient approach to exploring the common flow features that emerge over a range of flow parameters that can be utilized to facilitate reduced-order flow modeling.

CHAPTER 1

Magnetoconvection at Low Magnetic Reynolds and Prandtl Numbers

1.1 Introduction

Magnetoconvection, i.e. combined thermal convection and significant electromagnetic effects, dramatically changes the nature of flows of electrically conducting fluids. The phenomenon is known to play an important role in numerous systems found in technology and nature [1].

The dynamics of stellar convective shells and planetary cores are the examples of astrophysical and geophysical systems [2]. A notable example is the convective zone of the Sun illustrated in figure 1.1. The structure of the Sun contains the following layers: (1) fusion core − region of energy generation; (2) radiative zone − the zone where energy transport is by radiation flow; (3) convective zone − the zone where energy transport is by convection cells; (4) photosphere − the surface where photons are emitted; (5) chromosphere − the atmosphere of the Sun; (6) corona − the superhot region where the solar wind originates. The corresponding temperatures of the Sun's regions are presented in table 1.1.

One of the main physical concepts determining the structure of the Sun is the energy transport. Energy is transported from the core to the photosphere by convection or radiation. The solar plasma is not dense enough or hot enough to transfer the heat energy of

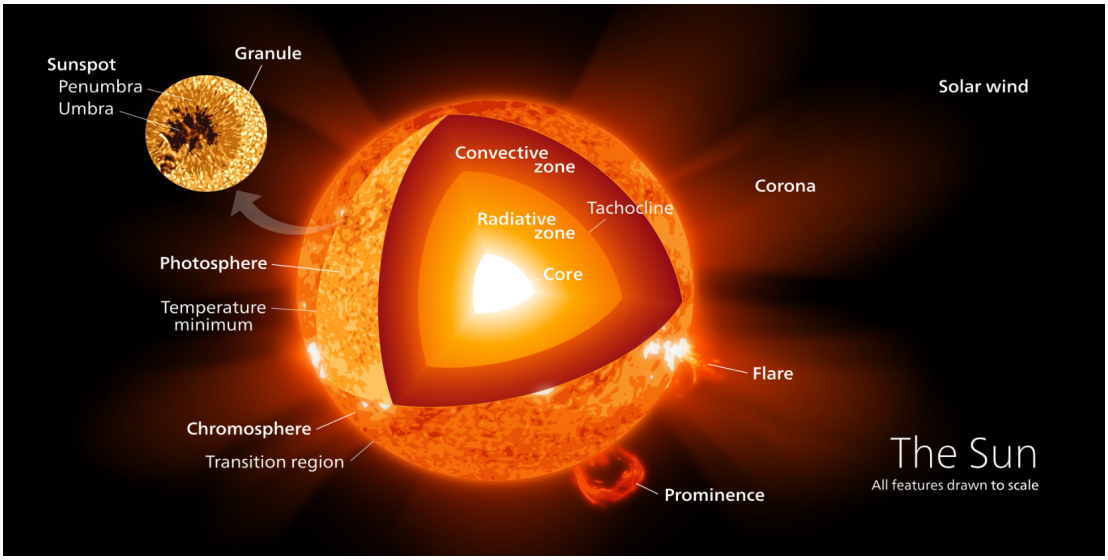

Figure 1.1: The structure of the Sun (www.wikipedia.org). The corresponding temperatures are shown in table 1.1.

Region	Temperature (K)
core	1×10^7
radiative zone	6×10^6
convective zone	1×10^6
photosphere	6×10^3
chromosphere	3×10^4
corona	1×10^6

Table 1.1: The temperatures of the Sun's regions.

the interior outward via radiation in the convective zone. Instead, the plasma density is low enough for convection currents to form and transfer energy outward towards the surface. Material at the bottom layer of the convective zone is heated by radiation that reduces its density. The plasma is cooled diffusively and radiatively just beneath the photospheric surface. The result is the convection cells that transport the majority of the heat to the photosphere. These cells are observed as solar granules. The lighter/darker color in the granules corresponds to hotter/colder regions and, thus, to ascending/descending zones of the convection cells.

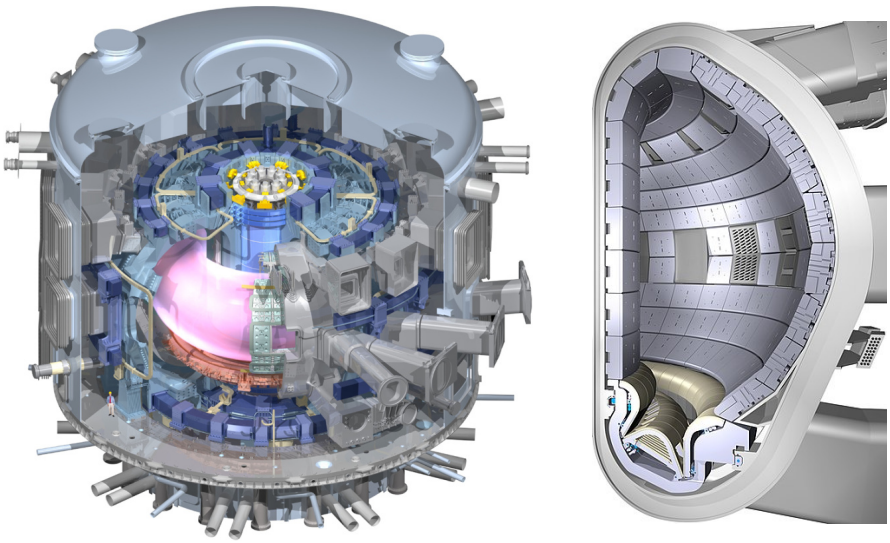

Figure 1.2: The ITER system and the blanket cross section on the left and right, respectively (www.iter.org).

Another important phenomenon visible on the surface of the Sun is the sunspots - dark spots, representing areas of strong magnetic fields. The strong magnetic fields inhibit convection in the photosphere (the mechanism is discussed in section 1.6). As a result, the energy flux from the Sun's core decreases, as does surface temperature, making the area through which the magnetic field passes colder and darker.

The technological examples are the liquid metal batteries [3], the growth of semiconductor crystals [4], and manufacturing of high-quality steels [5]. Another prominent example is the liquid metal blankets of nuclear fusion reactors, where an electrically conducting fluid (e.g., a PbLi alloy) serves as a coolant, radiation shield, and tritium breeder [6]. A distinctive feature of this system is that the convection and magnetic field effects are both exceptionally strong. The system will be, for the first time, tested in the International Thermonuclear Experimental Reactor (ITER) - ongoing massive international collaboration to develop technology of controlled thermonuclear fusion power production. It aims to prove that the carbon-free fusion energy can be produced on an industrial scale. The ITER and the blanket cross section are shown in figure 1.2.

The main fusion reaction in the blanket is when two nuclei come together to form an

alpha particle and a high-energy neutron [7]:

$$ {}^{2}_{1}D \ + \ {}^{3}_{1}T \longrightarrow \ {}^{4}_{2}He \ + \ {}^{1}_{0}n \ + \ 17.59MeV, \tag{1.1} $$

where D is the deuterium and T is the tritium. These nuclei are the most appealing for energy generation because they have the lowest activation energy, while providing the most energy per unit weight. While deuterium is abundant in nature, one of the main obstacles to the practical utilization of fusion energy is the scarcity of tritium. Experimental blanket modules will be utilized in the ITER and later projects to explore the possibility of breeding tritium for fuel from lithium-bearing material included within the blanket module using the following reactions:

$$ {}^{1}_{0}n \ + \ {}^{6}_{3}Li \longrightarrow \ {}^{3}_{1}T \ + \ {}^{4}_{2}He, \tag{1.2} $$

$$ {}^{1}_{0}n \ + \ {}^{7}_{3}Li \longrightarrow \ {}^{3}_{1}T \ + \ {}^{4}_{2}He + {}^{1}_{0}\, n, \tag{1.3} $$

where the reactant neutron is supplied by the D-T fusion reaction (1.1).

The energy carried by fast neutrons is removed and transferred to the main coolant. In future energy generating fusion plants, this heat energy would be utilized to power an electricity-generating turbine.

The blanket system is an an essential part of a fusion reactor (see figure 1.2). It provides the physical boundary for the plasma, contributes to the thermal and nuclear shielding of the vacuum vessel and the external components of the reactor from the heat and high-energy neutrons produced by the fusion reactions, and will be utilized later to produce tritium through reaction with neutrons from the plasma.

Several concepts of blanket modules are under current development: lead-lithium cooled ceramic breeder (LLCB), helium-cooled lithium-lead (HCLL), self-cooled lead-lithium (SCLL), dual coolant lithium-lead (DCLL) and others [8, 9]. The DCLL blanket module design with a lithium-lead eutectic as the neutron multiplier and tritium generating material is shown in figure 1.3.

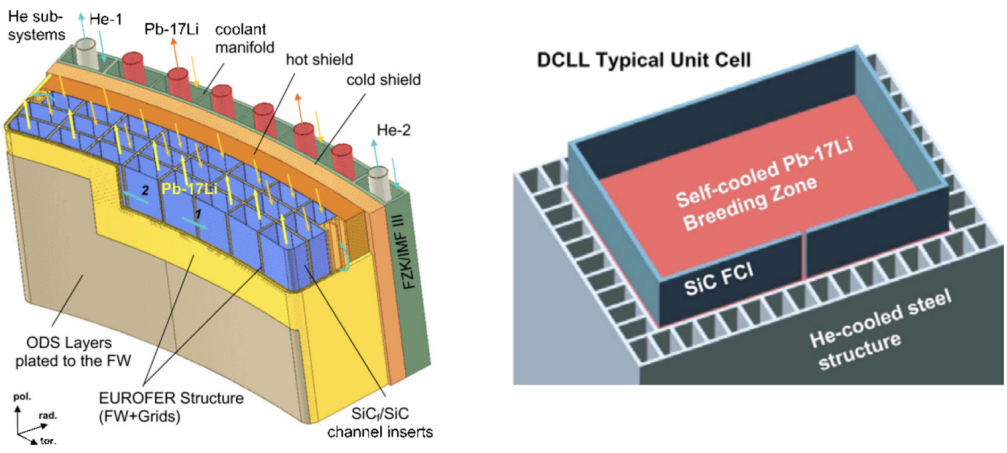

Figure 1.3: The EU He/Pb-Li dual-cooled fusion blanket concept module (left) and SiC/SiC flow channel insert in the proposed U.S. DCLL test blanket module (right) [8].

In the DCLL module, PbLi flow is utilized simultaneously for cooling, shielding and breeding, while other module types may serve only for some of these purposes. The main structural material of the blanket is low activation martensitic steel (Eurofer) with flow channel inserts (FCIs) made of composite or porous silicon carbide (SiC) as insulators between the steel and the lithium-lead. Eurofer is used with a small layer of oxide dispersion-strengthened (ODS) steel on the zone of the highest temperature, i.e. the plasma-facing zone of the first wall. The modules are large, stiff boxes with a grid structure inside, which are used as flow channels for the Pb-17Li and helium. The liquid-metal Pb-17Li serves as a coolant as well as the tritium-generating material. The lithium-lead flow channels are lined by silicon carbide composite inserts, providing thermal and electrical insulation. The thermal insulation allows higher temperature operation of the liquid metal for improved thermodynamic efficiency, whilst the electrical insulation avoids strong MHD pressure drop when pumping it at high velocity.

No preference can be given to any of the proposed concepts at this moment because tests and experiments with them are impossible in true reactor conditions until such reactors are built.

1.2 General Laws

The equations, in general, include conservation of mass, momentum and energy, and the MHD electrodynamic equations.

The conservation principles for the incompressible liquid metal flow are:

$$\frac{\partial \boldsymbol{u}}{\partial t} + (\boldsymbol{u} \cdot \nabla)\boldsymbol{u} = -\frac{1}{\rho}\nabla P + \nu \nabla^2 \boldsymbol{u} + \boldsymbol{f}, \tag{1.4}$$

$$\nabla \cdot \boldsymbol{u} = 0, \tag{1.5}$$

$$\rho c_p \left[\frac{\partial T}{\partial t} + \boldsymbol{u} \cdot \nabla T\right] = \kappa \nabla^2 T + Q. \tag{1.6}$$

where $\boldsymbol{u}$, P, and T are the fields of velocity, pressure, and temperature; $\boldsymbol{f}$ is the force which consists of buoyancy and Lorentz forces; ρ and ν are the density and kinematic viscosity of the liquid metal, respectively; Q represents the internal heating source, c_p is the heat capacity and κ is the heat conductivity of the flow. Conservation of momentum, mass and energy are (1.4), (1.5) and (1.6), respectively.

The Maxwell's equations for the electromagnetic effects are:

$$\nabla \cdot \boldsymbol{E} = \frac{\rho_e}{\varepsilon_0}, \tag{1.7}$$

$$\nabla \cdot \boldsymbol{B} = 0, \tag{1.8}$$

$$\nabla \times \boldsymbol{E} = -\frac{\partial \boldsymbol{B}}{\partial t}, \tag{1.9}$$

$$\nabla \times \boldsymbol{B} = \mu_0 \left(\boldsymbol{J} + \varepsilon_0 \frac{\partial \boldsymbol{E}}{\partial t}\right), \tag{1.10}$$

where ε_0 is the electric constant (also called the permittivity of free space), μ_0 is the magnetic constant (also called the permeability of free space), and ρ_e is the charge density; $\boldsymbol{J}$ is the electric current density; $\boldsymbol{E}$ and $\boldsymbol{B}$ are the electric and magnetic fields, respectively. The Gauss's Law is (1.7), the solenoidal nature of magnetic field is (1.8), the Faraday's law

in differential form is (1.9), and the Ampére-Maxwell equation is (1.10).

In addition to the equations (1.7) $-$ (1.10), we have

$$\nabla \cdot \boldsymbol{J} = -\frac{\partial \rho_e}{\partial t}, \tag{1.11}$$

$$\boldsymbol{J} = \sigma(\boldsymbol{E} + \boldsymbol{u} \times \boldsymbol{B}), \tag{1.12}$$

$$\boldsymbol{F}_L = q(\boldsymbol{E} + \boldsymbol{u} \times \boldsymbol{B}), \tag{1.13}$$

where σ is is the electrical conductivity and q is the charge. The charge conservation is (1.11), the Ohm's law is (1.12), and the Lorentz force is (1.13).

Not all of these laws are independent, for example, the solenoidal nature of magnetic field (1.8) follows from the divergence of Faraday's law (1.9), while the divergence of the Ampére-Maxwell equation (1.10), combined with charge conservation, yields Gauss' law (1.7).

The Maxwell's equations can be significantly simplified in MHD. The charge density ρ_e is extremely small in a conducting fluid and plays no significant part. It is assumed that any positive and negative charges are equilibrated on the time scale related to the speed of light, i.e., practically immediately in comparison to the typical time scale of the flow. The electric force $q\boldsymbol{E}$ is small by comparison with the Lorentz force. Therefore, the Guass's law may be dropped and the charge conservation equation may be reduced to the simplified statement. The displacement currents are negligible by comparison with the current density in conducting fluids. Thus, the Ampére-Maxwell equation reduces to the differential form of Ampére's law. Detailed derivations can be found in many textbooks, such as [1, 10].

The (pre-Maxwell) form of the electrodynamic equations used in MHD can be written as follows:

$$\nabla \cdot \boldsymbol{J} = 0, \tag{1.14}$$

$$\nabla \times \boldsymbol{B} = \mu_0 \boldsymbol{J}, \tag{1.15}$$

$$\nabla \cdot \boldsymbol{B} = 0, \tag{1.16}$$

$$\nabla \times \boldsymbol{E} = -\frac{\partial \boldsymbol{B}}{\partial t}, \tag{1.17}$$

$$\boldsymbol{J} = \sigma(\boldsymbol{E} + \boldsymbol{u} \times \boldsymbol{B}), \tag{1.18}$$

$$\boldsymbol{F}_L = \boldsymbol{J} \times \boldsymbol{B}. \tag{1.19}$$

1.3 Simplifying Approximations

Flows of an incompressible, Newtonian, viscous, non-magnetizable, electrically conducting fluid (a liquid metal) with constant physical properties are considered. The fluids are contained in a vertical cylinder with an unstable temperature stratification and a uniform axial magnetic field (Chapter 2: RBC) or moving through a horizontal duct heated from below with a uniform horizontal transverse magnetic field (Chapter 3: PRBF) are considered. Natural convection is the key mechanism of the flow physics for the former. For the latter, the focus is on the mixed convection.

Three approximations are typically made in numerical and theoretical studies of magnetoconvection of liquid metal flows [9]. The first is the Boussinesq approximation, according to which variations of physical properties of the liquid with pressure and temperature are neglected, with the exception of density, for which linear variation with temperature is assumed in the buoyancy force term in the momentum equation. One may question the validity of this approximation because temperature may vary by many tens of degrees within the flow domain as it is demonstrated below. However, analysis of physical properties reveals that such concerns are rarely warranted. For example, considering the Pb-17Li alloy and taking $870K$ as a reference point, we find that an increase of temperature by $50K$ results in relatively low changes of all properties, except the dynamic viscosity and thermal conductivity, for which the change is 10% and 5%, respectively.

The second approximation neglects the heat sources corresponding to the Joule and viscous dissipations in the energy equation. This is justified by the typically very high ($\sim 10^6$) values of the electrical conductivity σ, very low ($\sim 10^{-7}$) values of the Eckert numbers $Ec \equiv U^2(c_p\Delta T)^{-1}$ and/or by high applied thermal load. The Eckert number is defined as the ratio of the advective mass transfer to the heat dissipation potential. The thermoelectric Thomson, Peltier, and Seebeck effects can also be neglected with exception of the applications characterized by extreme temperature gradients.

The last commonly used asymptotic approximation is the quasi-static (inductionless) model utilized to describe the electromagnetic interactions [1, 10, 11]. Let us consider the case when a steady magnetic field $\boldsymbol{B}_0$ is imposed in the flow domain. The electric currents induced in the flow $\boldsymbol{j}_0 \sim \sigma \boldsymbol{u} \times \boldsymbol{B}_0$ generate perturbations of the magnetic field $\boldsymbol{b}$. Thus, the total magnetic field can be written as $\boldsymbol{B} = \boldsymbol{B}_0 + \boldsymbol{b}$ that satisfies the MHD equations in section 1.2. These equations can be simplified with the use of the quasi-static approximation. The approximation is accurate when the magnetic Reynolds and Prandtl numbers are both small:

$$Re_m \equiv \frac{Ud}{\eta} \ll 1, \tag{1.20}$$

$$Pr_m \equiv \frac{\nu}{\eta} = \frac{Re_m}{Re} \ll 1, \tag{1.21}$$

where Re_m is the ratio of advection to magnetic diffusivity and Pr_m is the ratio of the viscosity to the magnetic diffusivity; U and d are the typical scales of velocity and length, respectively; $\eta = (\sigma\mu_0)^{-1}$ is the magnetic diffusivity; $Re = Ud/\nu$ is the hydrodynamic Reynolds number.

The magnetic Reynolds and Prandtl numbers are both small for practically all technical liquid metal flows, including flows in the liquid metal blankets of nuclear fusion reactors. For example, $Pr_m = 0.28 \times 10^{-6}$ for Pb, $Pr_m = 0.21 \times 10^{-6}$ for PbLi or $Pr_m = 1.3 \times 10^{-6}$ for Ga [12]. Small values of Re_m can be found and the quasi-static approximation can be applied in the majority of laboratory experiments and technological flows. The model

remains accurate at Re_m up to ~ 0.1. Its applicability thus extends to flows with Reynolds numbers Re up to $\sim 10^5$.

The quasi-static approximation amounts to two simplifications valid in the conditions of $Re_m \ll 1$ and $Pr_m \ll 1$ [1, 10, 11]. The applied magnetic field $\boldsymbol{B}_0$ is much stronger than the perturbations of the magnetic field $\boldsymbol{b}$ induced by the electric currents flowing with the fluid. Furthermore, it can be assumed that the induced field adjusts instantaneously to changes of flow velocity. Thus, under the quasi-static approximation, diffusion of the magnetic field dominates its advection. The flow-field interaction is reduced from the two-way coupling between the fluid motion and the magnetic field to a one-way influence of the magnetic field on the flow. Theoretical analysis and validation studies (experimental and numerical) [1, 9] confirm that.

The Ohm's law and the Lorentz force can be written as follows:

$$\boldsymbol{J} \approx \sigma(\boldsymbol{E}_0 + \boldsymbol{u} \times \boldsymbol{B}_0), \tag{1.22}$$

$$\boldsymbol{F}_L \approx \boldsymbol{J} \times \boldsymbol{B}_0. \tag{1.23}$$

The electric field $\boldsymbol{E}_0$ is irrotational (see (1.17)) and may be written as $-\nabla\phi$, where ϕ is the electric potential. Ohm's law now takes the particularly simple form

$$\boldsymbol{J} = \sigma(-\nabla\phi + \boldsymbol{u} \times \boldsymbol{B}_0), \tag{1.24}$$

with the potential being the solution of the Poisson equation:

$$\nabla^2\phi = \nabla \cdot (\boldsymbol{u} \times \boldsymbol{B}_0). \tag{1.25}$$

which expresses the electric neutrality of the liquid (1.14).

Moreover, $\boldsymbol{J}$ is uniquely determined by (1.22) since $\nabla\cdot\boldsymbol{J} = 0$, $\nabla\times\boldsymbol{J} = \sigma\nabla\times(\boldsymbol{u}\times\boldsymbol{B}_0)$ and a vector field is unambiguously determined if its divergence and curl are known. From

now on the subscript on $\boldsymbol{B}_0$ will be dropped on the understanding that $\boldsymbol{B}$ represents the imposed magnetic field.

1.4 Governing Equations and Non-dimensional Parameters

With the mentioned above approximations, the non-dimensional governing equations are:

$$\frac{\partial \boldsymbol{u}}{\partial t} + (\boldsymbol{u} \cdot \nabla)\boldsymbol{u} = -\nabla p + \frac{1}{Re}\nabla^2 \boldsymbol{u} + \boldsymbol{F}_b + \boldsymbol{F}_L, \tag{1.26}$$

$$\nabla \cdot \boldsymbol{u} = 0, \tag{1.27}$$

$$\frac{\partial T}{\partial t} + \boldsymbol{u} \cdot \nabla T = \frac{1}{Pe}\nabla^2 T + q. \tag{1.28}$$

where $\boldsymbol{u}$, p, and T are the fields of velocity, pressure, and perturbation of temperature with respect to a reference value. There can be internal heating of volumetric rate q. The non-dimensional buoyancy and Lorentz forces are computed as:

$$\boldsymbol{F}_b = GrRe^{-2}T\boldsymbol{e}_g, \tag{1.29}$$

$$\boldsymbol{F}_L = Ha^2Re^{-1}\boldsymbol{j} \times \boldsymbol{B}, \tag{1.30}$$

where $\boldsymbol{e}_g$ is the unit-length vector in the direction of gravity and $\boldsymbol{B}$ is the nondimensionalized imposed magnetic field. The electric current $\boldsymbol{j}$ is determined by the Ohm's law

$$\boldsymbol{j} = -\nabla\phi + (\boldsymbol{u} \times \boldsymbol{B}), \tag{1.31}$$

where the electric potential ϕ is a solution of the Poisson equation expressing the instantaneous electric neutrality of the fluid:

$$\nabla^2\phi = \nabla \cdot (\boldsymbol{u} \times \boldsymbol{B}). \tag{1.32}$$

The specific typical scales leading to the non-dimensional system (1.26)−(1.32) and formulation of the system will be presented in Chapter 2 for the RBC and in Chapter 3 for the PRBF. The non-dimensional parameters are:

$$Re = \frac{Ud}{\nu} - \text{Reynolds number} \tag{1.33}$$

$$Pr = \frac{\nu}{\chi} - \text{Prandtl number} \tag{1.34}$$

$$Pe \equiv RePr = \frac{Ud}{\chi} - \text{Peclet number} \tag{1.35}$$

$$Ha = Bd\sqrt{\frac{\sigma}{\rho\nu}} - \text{Hartmann number} \tag{1.36}$$

$$N \equiv \frac{Ha^2}{Re} = \frac{\sigma B^2 d}{\rho U} - \text{Stuart number} \tag{1.37}$$

$$Gr = \frac{g\beta\Delta T d^3}{\nu^2} - \text{Grashof number} \tag{1.38}$$

$$Ra \equiv GrPr - \text{Rayleigh number} \tag{1.39}$$

with the temperature diffusivity χ, the mass density ρ, the acceleration due to gravity g, the coefficient of thermal expansion β, the specific temperature scale ΔT, and the typical scale of the imposed magnetic field B.

The Reynolds number can be viewed as the typical ratio between the inertial forces to viscous forces. The Prandtl number is defined as the ratio of momentum diffusivity to thermal diffusivity. The Peclet number estimates the ratio between the rate of advection to the rate of diffusion of heat. The Rayleigh number can be used instead of the Grashof number. It may be viewed as the ratio of buoyancy and viscosity forces multiplied by the ratio of momentum and thermal diffusivities. The strength of the magnetohydrodynamic effect is evaluated by the Hartmann number. More specifically, Ha^2, which is sometimes referred to as the Chandrasekhar number, estimates the typical ratio between the Lorentz and viscous forces. Alternatively, one can use the Stuart number (the ratio between the

Lorentz and inertial forces).

1.5 Numerical Method

The governing equations (1.26) – (1.32) with appropriate boundary and initial conditions are solved using the finite difference scheme introduced in [13], and later developed and applied to high-Ha flows and flows with thermal convection in numerous works including, for example in [9, 14–18]. Performance of the method in applications to magnetoconvection was analyzed in comparison with other methods, in particular with the finite volume method (FVM) in [19].

The new computational model for MHD convection flows in cylindrical geometries based on the highly conservative finite-difference scheme [13, 20] have been developed for the work presented in Chapter 2 of this dissertation. The model underwent successful verification based on comparison with finite difference method (FDM) and spectral element method (SEM). The details and results of the model for the RBC are presented in Chapter 2.

Another 2D model has been validated and applied, together with full 3D analysis, for magnetoconvective flows in a horizontal duct. The flows are approximated in the asymptotic limit of a very strong magnetic field effect according to the 2D model proposed in [21]. The details and results of the models for the PRBC are presented in Chapter 3.

1.5.1 Time Discretization and Projection Algorithm

The time discretization is semi-implicit and based on the Adams-Bashforth (Backward) differentiation method of the second order. The time discretization uses the standard projection algorithm [22]. The nonlinear convection and body force terms are treated explicitly. For the PRBF, the time discretization is implicit for the viscosity terms. For the RBC, implicit treatment is applied to the the azimuthal derivative part of the velocity Laplacian in (1.26) in order to avoid the time-step limitations due to diffusive stability limit in the

narrow grid cells near the axis. The radial and axial parts of the viscous term in (1.26) are treated explicitly.

The use of the implicit scheme for temperature is more important. It allows us to avoid the strong numerical instability limitations on the size of the time step that arise at strong near-wall clustering at small number of Pr typical for the liquid metals.

The time step from t^n to $t^{n+1} = t^n + \Delta t$ consists of the following substeps:

(i) Solving the Poisson equation for electric potential, computing the electric current and the body forces:

$$\nabla^2 \phi^n = \nabla \cdot (\boldsymbol{u}^n \times \boldsymbol{e}_b)\,, \tag{1.40}$$

$$\boldsymbol{j}^n = -\nabla \phi^n + \boldsymbol{u}^n \times \boldsymbol{e}_b, \tag{1.41}$$

$$\boldsymbol{F}_b^n = GrRe^{-2}T^n \boldsymbol{e}_g, \tag{1.42}$$

$$\boldsymbol{F}_L^n = Ha^2 Re^{-1} \boldsymbol{j}^n \times \boldsymbol{e}_b. \tag{1.43}$$

(ii) Finding the intermediate velocity field $\boldsymbol{u}^*$ for the next time layer using:

$$\frac{3\boldsymbol{u}^* - 4\boldsymbol{u}^n + \boldsymbol{u}^{n-1}}{2\Delta t} = 2\boldsymbol{F}^n - \boldsymbol{F}^{n-1} + \frac{1}{Re}\nabla^2 \boldsymbol{u}^*, \tag{1.44}$$

$$\boldsymbol{F}^n = -\boldsymbol{M}(\boldsymbol{u}^n, \boldsymbol{u}^n) + \boldsymbol{F}_b^n + \boldsymbol{F}_L^n, \tag{1.45}$$

where $\boldsymbol{M}(\boldsymbol{u}^n, \boldsymbol{u}^n)$ is the nonlinear term in divergence form, and the viscosity term is treated in the just way described above.

(iii) Solving the Poisson equation for pressure fluctuations and applying the pressure correction to the velocity field to secure mass conservation:

$$\nabla^2 p^{n+1} = \frac{3}{2\Delta t}\nabla \cdot \boldsymbol{u}^*, \tag{1.46}$$

$$\boldsymbol{u}^{n+1} = \boldsymbol{u}^* - \frac{2}{3}\Delta t \nabla p^{n+1}. \tag{1.47}$$

(iv) Solving the implicit equation for temperature:

$$\frac{3T^{n+1} - 4T^n + T^{n-1}}{2\Delta t} = 2G^n - G^{n-1} + \frac{1}{Pe}\nabla^2 T^{n+1}, \tag{1.48}$$

where $G^n = -\nabla \cdot (T^n \boldsymbol{u}^n) - q^n$, with the boundary conditions.

As described in detail in section 3.2.1, the procedure is modified in simulations of the fully developed PRBF. Decomposition of temperature and pressure into mean-mixed and perturbation components is used.

The elliptic equations for potential, pressure, temperature and velocity components are solved using the fast Fourier transform (FFT) in the azimuthal direction for the RBC or in the streamwise direction for the PRBF, and the direct cyclic reduction solution of the 2D equations for Fourier components conducted on the transformed grid (see [13]).

The algorithm is parallelized using the hybrid (MPI-OpenMP) approach for the RBC (in the cylindrical coordinates) and for the PRBF (in the Cartesian coordinates). The MPI memory distribution is along the z-coordinate for the RBC and the y-coordinate for the PRBF in the physical space, and along the azimuthal wavenumber for the RBC and the streamwise wavenumber for the PRBF in the Fourier space.

1.5.2 Spatial Discretization

Finite difference discretization of the second order on a structured non-uniform grid is applied (see, e.g., figures 1.4 and 1.5). An important feature of the discretization is its conservative properties [13, 20]. Spatial derivatives are evaluated using the velocity and current fluxes. The fluxes are obtained by special interpolations to half-integer grid points. This renders the scheme perfectly conservative in the non-viscous non-conductive limit in regards of mass, momentum, electric charge and thermal energy. The conservation of kinetic energy is satisfied with a dissipative error of the third order.

For the RBC, the spatial discretization is implemented in the cylindrical coordinates

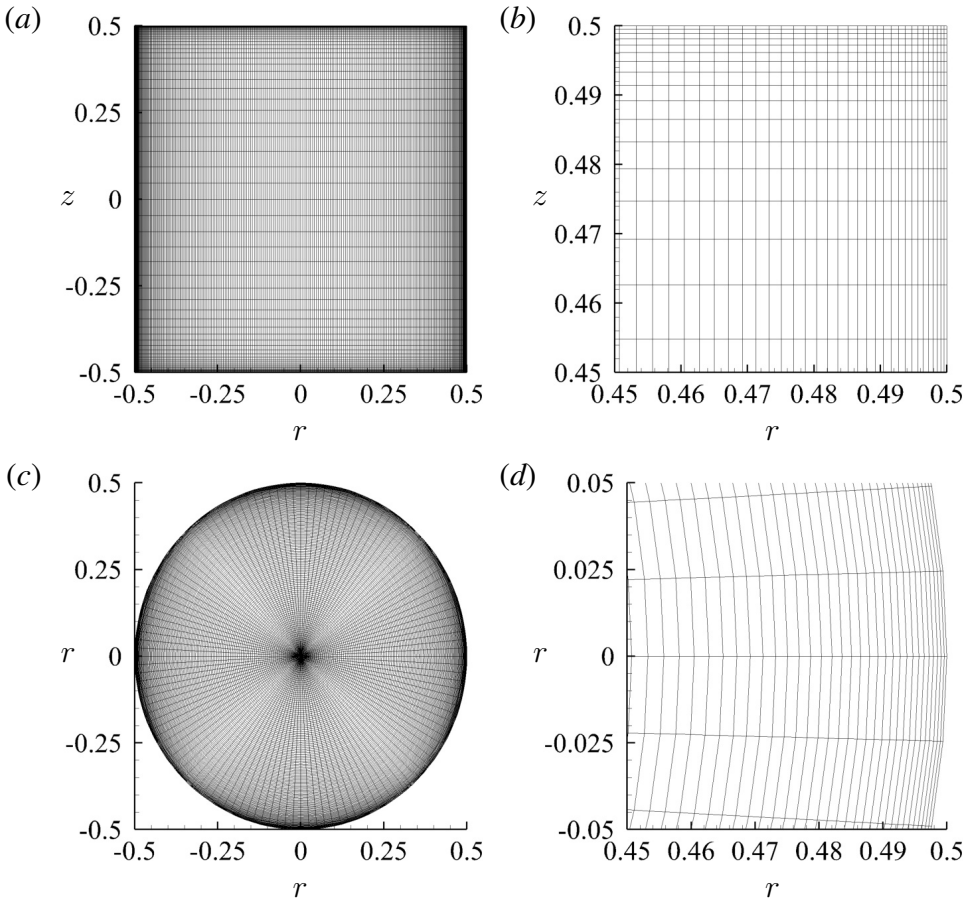

Figure 1.4: Grid resolution in the vertical (a, b) and horizontal mid-plane (c, d) cross-sections used in the RBC simulations at $Ra = 10^8$, $Ha = 450$ with $N_r \times N_z \times N_\theta = 256 \times 128 \times 256$, $A_z = 3.5$, $C_r = 0.9$ (different scales of z and r are used in the zoom-in plots (b, d)). The magnetic field is in the z-direction (see the flow configuration in figure 2.2 in Chapter 2).

with the boundary conditions at the axis specified as discussed in [16]. The computational grid is clustered towards the walls according to the coordinate transformation in the axial direction z and in the radial direction r:

$$z = \frac{\tanh(A_z \zeta)}{\tanh(A_z)}, \tag{1.49}$$

$$r = C_r \sin\left(\frac{\eta\pi}{2}\right) + (1 - C_r)\eta, \tag{1.50}$$

where $-1 \leq \zeta \leq 1$ and $0 \leq \eta \leq 1$ are the transformed coordinates, in which the grid

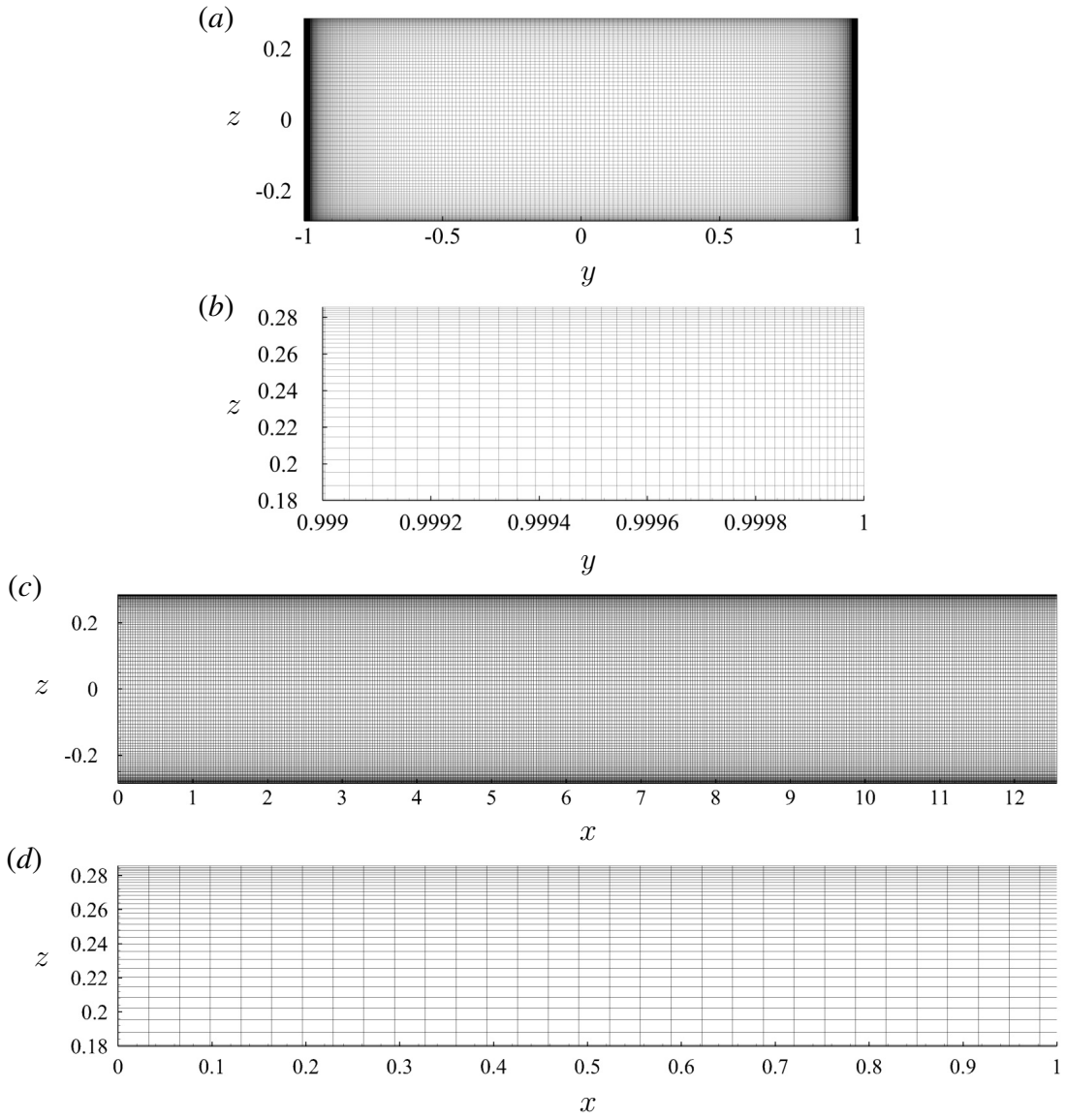

Figure 1.5: Grid resolution used in the $z-y$ plane for the base flow (a, b) and in the $z-x$ plane for the nonlinear regime (c, d) in the PRBC simulations at $Gr = 10^8$, $Ha = 10^4$. For the base flow, the grid $N_y \times N_z = 512 \times 96$ with $A_z = 2.0$, $A_y = 4.3$ is applied (different scales of z and y are used in the zoom-in plot (b)). For the nonlinear flow, the grid $N_x \times N_z = 384 \times 96$ with $A_z = 2.0$ is utilized (different scales of z and x are used in the zoom-in plot (d)). The wall heating is at the wall at $z = -0.2857$, and the magnetic field is in the y-direction (see the flow configuration in figure 3.1 in Chapter 3).

is uniform; A_z is the coefficient determining the degree of clustering; C_r is the blending coefficient of the Chebyshev and identity transformation.

The spatial discretization for the PRBF is built on the Cartesian coordinates following

the earlier studies [13–15, 17]. The computational grid is clustered towards the walls according to the coordinate transformation in the horizontal direction y and in the vertical direction z

$$y = \frac{\tanh(A_y \eta)}{\tanh(A_y)}, \tag{1.51}$$

$$z = \frac{\tanh(A_z \xi)}{\tanh(A_z)}, \tag{1.52}$$

where η and ξ are the transformed coordinates, in which the grid is uniform; A_y and A_z are the coefficients determining the degrees of clustering.

The thorough verification of the algorithms and grid sensitivity studies have been conducted to identify proper resolution for RBC (see sections 2.2.2, 2.2.4) and for PRBF (see sections 3.2.4, 3.3.2).

1.6 Effects of Magnetic Field

The principal physical mechanisms by which an imposed magnetic field transforms a flow of an electrically conducting fluid are briefly discussed here. The discussion is valid for flows satisfying the quasi-static approximation (low Re_m and Pr_m).

The well-known effects of very strong magnetic fields on flows of electrically conducting fluids is the suppression of turbulence and transformation of the flow into an anisotropic state [1, 11]. The Joule dissipation of the electric currents created when an electrically conducting fluid flows in a magnetic field is directly related to these phenomena. The dissipation serves as an additional (to the viscous dissipation) mechanism of conversion of the flow's kinetic energy into heat. The result of the mechanism is MHD flows in a laminar or transitional state at much higher control parameters (such as, e.g., Re or Ra) than hydrodynamic flows of the same type.

The special nature of MHD flows is related to the fact that the Joule dissipation is anisotropic. Its rate is proportional to the square of the velocity gradient in the direction of

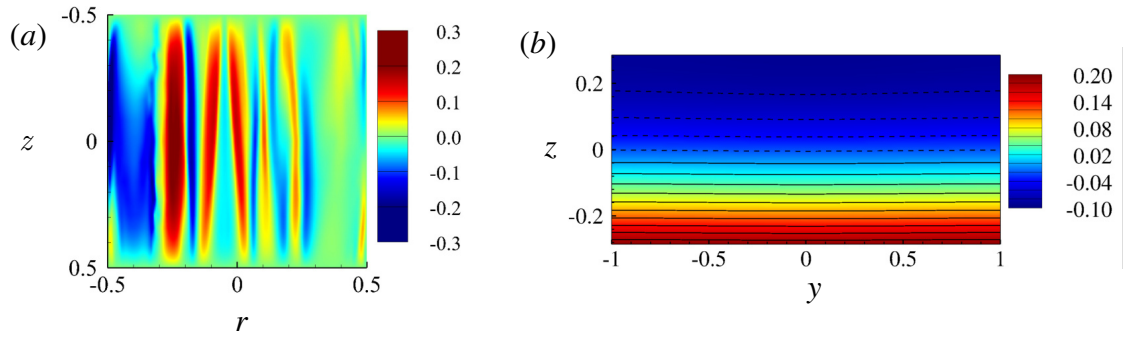

Figure 1.6: (a) The result of the RBC study: Snapshot of the vertical velocity in the vertical cross-section at $Ra = 10^8$, $Ha = 1400$. The magnetic field is in the z-direction. (b) The result of the PRBF study. Distribution of temperature Θ in the base flow at $Ha = 1000$, $Gr = 10^8$. The wall heating is at the wall at $z = -0.2857$, and the magnetic field is in the y-direction.

the magnetic field (see, e.g., [21, 23]). Flow structures with largest gradients generate the strongest currents and experience the strongest suppression due to the Joule dissipation. The flow becomes anisotropic as a whole, with its structures elongated along magnetic field lines (see, e.g, figure 1.6: the results of the study are discussed in details in Chapters 2 and 3). The anisotropy is used here with the meaning of dependence of velocity gradients and typical length scales of the flow on the spatial direction. The anisotropy of magnitude of velocity components (and the Reynolds stresses) usually follows, but it is not caused directly by the magnetic field and has a nonuniversal nature, strongly influenced by initial conditions, boundaries, and other specific flow features.

The value of the Stuart number has a big impact on the degree of flow transformation. In general, flow remains turbulent at moderate values of $N \sim 1$, but it acquires noticeable anisotropy and modified statistical properties [24, 25]. At large values of N, the flow undergoes a transformation that involves full turbulence suppression and quasi two-dimensionality (Q2D). The latter term refers to a flow in which all of its variables are uniform (or nearly uniform with extremely weak gradients) along the magnetic field lines in the flow's core. The uniformity ceases within the boundary layers at the walls crossing the field lines, where sharp gradients appear to satisfy the boundary conditions.

The additional anisotropic dissipation mechanism changes the instabilities and dynamics of common flows. It must be stressed that only the instability modes that have significant non-zero velocity gradients along the magnetic field lines are suppressed by the Joule dissipation. Modes with zero or weak such gradients (2D or Q2D) are either not influenced at all or influenced only slightly. This has serious implications for systems where geometry and physics allow for such modes to exist. The typical situation is when a conventional hydrodynamic instability is suppressed, but the flow does not retain its base form. Instead, it becomes unstable to 2D or Q2D modes at higher control parameters.

The modification of the flow in the systems with large Ha and N is strong to such a degree that its behavior changes in a profound, counterintuitive, or even paradoxical way. Growth of 2D or Q2D modes and the subsequent evolution of resulting flow structures may be observed on the background of fully suppressed conventional 3D turbulence when the effect of magnetic field is strong. In addition, secondary 3D instabilities of the 2D or Q2D structures are either fully or partially suppressed and result in flow regimes dominated by large-scale 2D or Q2D coherent structures.

The manifestations of their evolution is still not fully explored effect of an imposed magnetic field on the flow configurations. For example, complex and sometimes spectacular dynamics including appearance of vertical cells, columns or wall modes have been observed in flows with a vertical magnetic field in the RBC (see, e.g., [26,27]). Moreover, the presence of the vertical large-scale circulation (LSC) modes results in an unusually strong heat transfer in comparison to the conventional turbulent RBC. In PRBC, the anomalous temperature fluctuations in fully suppressed turbulence in Q2D flows were identified (see, e.g., [16]). The properties of such fluctuations extremely depend on the flow's configuration and values of the control parameters (such as Re, Ha, etc.).

The counterintuitiveness of aforementioned magnetoconvective effects on the fluid flows sets up the general goal of this dissertation that is to explore the principal physical mechanisms determining these phenomena in the framework of high-resolution DNS.

1.7 Outline of the Dissertation

There are three main chapters in the dissertation. The RBC is discussed in Chapter 2. The PRBC is presented in Chapter 3 with the modal analysis to the PRBC flow in Chapter 4. Chapters 2 and 3 follow the same structure. They start with the motivation and literature review, followed by the presentation of the problem that includes the physical model with the governing equations and boundary conditions, its verification and validation by performing grid sensitivity studies and experimental comparison, and finally, the results.

In Chapter 2, the spatial structure of the flow and global transport properties are explored at very strong magnetic fields in the RBC. The focus of the discussion is on the novel flow regime dominated by wall modes. We demonstrate that the peculiar phenomenon of significant increase of the heat transfer rate at Ha and Ra observed in earlier experiments can be attributed to this regime.

In Chapter 3, the analysis of the base flow, linear stability and the structure of the nonlinear flow is performed in PRBC. The effect of the anomalously strong temperature fluctuations at the values of Ha and Gr typical for a nuclear fusion reactor is thoroughly explored. The parametric study is conducted to understand the influence of various magnetoconvective parameters on the liquid metal flow in a horizontal duct. Moreover, the PRBC flow is explored with the use of modal decomposition technique in Chapter 4. The results of the analysis show an effective low-dimensional representation of magnetoconvective flows that captures the physically dominant features in the spatial modes.

Finally, the concluding remarks of the research and ideas for future work are presented in Chapter 5.

CHAPTER 2

Rayleigh-Bénard Convection

The computational results presented later in this chapter are published in [28, 29].

2.1 Motivation and Review

The configuration of the RBC in a vertical cylinder with thermally insulating sidewalls and an imposed vertical magnetic field is considered (see figure 2.2). Systems with lateral walls add the aspect ratio $\Gamma = d/h$ as a control parameter to Ra, Ha, and Pr (determined in 1.4), where d is the typical horizontal size, the diameter of the cylinder in our case. The effect of a vertical magnetic field on RBC has been previously studied experimentally [30–35], numerically [26–29] and theoretically [36–38].

The classical picture of the effect of a magnetic field on RBC in an infinite horizontal layer includes suppression of turbulence [30] and increase of the critical Rayleigh number Ra_c for the onset of convection. The latter effect is given by [36] in the asymptotic form at high Ha as $Ra_c \approx \pi^2 Ha^2$. The dominance of Q2D cellular and columnar structures in the flows at $Ra > Ra_c$ within a layer with stress-free boundary conditions was observed in [27]. The flow regimes are identified as Q2D when the velocity and temperature fields are virtually independent of the axial direction outside of the boundary layers near the top and bottom walls. These regimes are uniquely identified by the slope of the Nusselt number $Nu(Ra)$ and Reynolds number $Re(Ra)$ numbers, the physical structure of the flows,

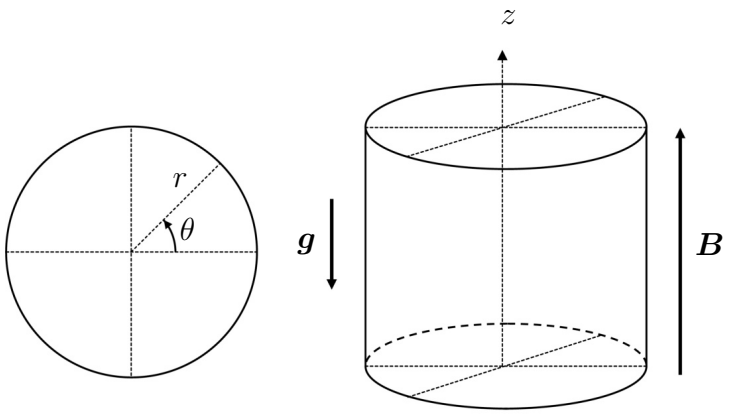

Figure 2.1: RBC cell and coordinate system. The arrows marked by letters $\boldsymbol{g}$ and $\boldsymbol{B}$ denote, respectively, the orientations of the gravity acceleration and magnetic field.

and the relative sizes of terms in the governing equations (regimes are considered to be magnetically constrained in the sense that the Lorentz force plays a leading-order role in the dynamics). The first regime is reminiscent of convection, with cellular flow structures and a heat transport that increases rapidly but cannot be characterized by a single power-law scaling. The second regime is characterized by localized, quasi-laminar convection columns that align with the imposed magnetic field and shows a $Nu \backsim (Ra/Ha)^{\gamma}$ scaling. The value of γ increases toward unity with an increasing effect of magnetic field.

The theoretical analysis of [38] predicts that the presence of the sidewalls leads to the onset of convection at a much lower Ra than in an infinite layer. The heat transfer in that case is concentrated near the walls. Recent numerical simulations [26] of RBC in a rectangular cell at $Ra \sim Ra_c$ and $Ra < Ra_c$ confirmed the existence of this so-called wall-mode regime, in which significant flow and heat transfer are limited to narrow zones near the sidewalls (the wall modes). These modes have a form of planar jets that fill the entire cell at moderate Ha. A sufficiently strong magnetic field expels convective motion from the enterior of the cell where heat is then transported solely by diffusion at high Hartmann numbers, higher than $Ha_c \equiv \sqrt{Ra}/\pi \approx 1000$ (see figure 2.2). The complex two-layer structure at high Ha consists of alternating up- and downwelling flow regions attached to

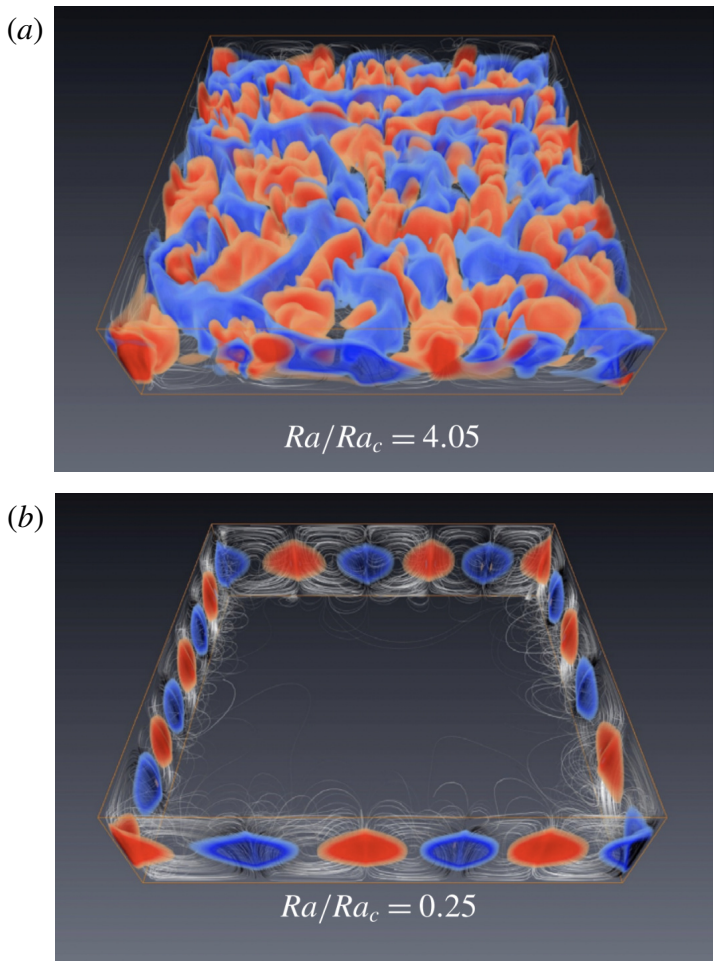

Figure 2.2: Snapshots of the magnetoconvection flow at $Ha = 500$ (a) and $Ha = 2000$ (b) [26]. The isosurfaces of $u_z = \pm 0.01$ together with field lines of the velocity field that highlight the circulation rolls at the sidewalls are displayed. The ratio Ra/Ra_c is indicated in each of the panels. For ratio of $Ra/Ra_c < 1$ the linear stability theory predicts a purely diffusive transport in a fluid layer with $\boldsymbol{u} = 0$.

the sidewalls. Wall modes have also been found in simulations of RBC in a cylindrical cell at $\Gamma = 4$, $Pr = 0.025$, $Ha \leq 1000$ and $Ra = 10^7$ [28]. The simulation results are consistent with the recent extensive measurements of RBC with a vertical magnetic field in a vertical cylinder with moderate Ra and Ha by [35, 39].

The focus of the chapter is on the RBC with vertical magnetic field and sidewalls at $Ra \gg Ra_c$. High-resolution DNS of flows in a cylindrical cavity with $\Gamma = 1$, $Pr = 0.025$, $10^7 \leq Ra \leq 10^9$ and $0 \leq Ha \leq 1400$ are performed. The work follows the experiments [31] carried out at the same Γ and Pr (mercury) and at $Ra \leq 3 \times 10^9$ and $Ha \leq 2000$

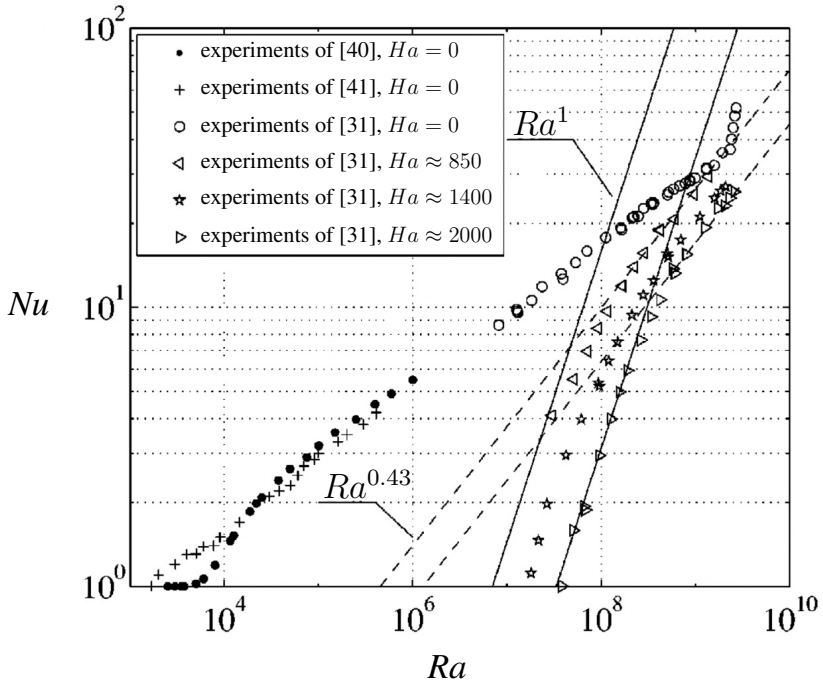

Figure 2.3: Nusselt number Nu vs Ra with and without magnetic field [31]. The two dashed lines represent the $Ra^{0.43}$ scaling and the solid ones represent the Ra^1 scaling.

(the highest Ra and Ha achieved so far). The experiments have shown that the slope β of the asymptotic power law $Nu \backsim Ra^{\beta}$ increases from $\beta \approx 0.26$ in non-magnetic flows to up to $\beta \approx 1$ at high Ha. The result is that the heat transfer rate in high-Ra flows in very strong magnetic fields becomes comparable to the rate in turbulent flows without the magnetic field (see $Ra \approx 10^9$ in figure 2.3). The physical mechanisms determining this counterintuitive behavior remain to be understood.

Interestingly, a certain similarity between the behavior found in RBC with vertical magnetic field and that in convection with rotation around vertical axis should also be mentioned. Experiments and DNS reveal formation of Q2D structures, faster growth of heat transfer rate with Ra at high rotation rates, and wall modes in rotating systems [42–44].

To the best of my knowledge, this study is the first to analyze turbulent RBC at high Ha and realistically low Pr in the framework of high-resolution DNS [28, 29]. The only related simulations have been performed by [45] in a cubic convection cell at unrealistic $Pr = 8$ with Ra up to 10^{10} and Ha up to 800.

2.2 Presentation of the Problem

2.2.1 Physical Model

The flow of an incompressible, viscous, electrically conducting fluid (a liquid metal) with constant physical properties contained in a cylinder with a uniform axial magnetic field is considered. The governing equations are made dimensionless by using the cylinder's height H, the free-fall velocity $U = \sqrt{g\alpha\Delta T H}$, the external magnetic field strength B_0 and the imposed temperature difference $\Delta T = T_{bottom} - T_{top}$ as the scales of length, velocity, magnetic field and temperature, respectively. The Boussinesq and quasi-static approximations are used. The equations are

$$\nabla \cdot \boldsymbol{u} = 0, \tag{2.1}$$

$$\frac{\partial \boldsymbol{u}}{\partial t} + (\boldsymbol{u} \cdot \nabla)\boldsymbol{u} = -\nabla p + \sqrt{\frac{Pr}{Ra}}(\nabla^2 \boldsymbol{u} + Ha^2\,(\boldsymbol{j} \times \boldsymbol{e}_z)) + T\boldsymbol{e}_z, \tag{2.2}$$

$$\frac{\partial T}{\partial t} + \boldsymbol{u} \cdot \nabla T = \sqrt{\frac{1}{RaPr}}\nabla^2 T, \tag{2.3}$$

$$\boldsymbol{j} = -\nabla\phi + (\boldsymbol{u} \times \boldsymbol{e}_z), \tag{2.4}$$

$$\nabla^2\phi = \nabla \cdot (\boldsymbol{u} \times \boldsymbol{e}_z), \tag{2.5}$$

where p, $\boldsymbol{u}$, ϕ and T are the fields of non-dimensionalized pressure, velocity, electric potential, and deviation of temperature from a reference value. The top and bottom walls are maintained at constant temperatures $T = -0.5$ and $T = 0.5$, respectively. The lateral wall is thermally insulated, so having $\partial T/\partial n = 0$. No-slip boundary conditions for velocity are applied at the walls. All walls are perfectly electrically insulated, which implies $\partial\phi/\partial n = 0$.

2.2.2 Verification of the Model

The numerical method for the new model with the DNS finite difference method (FDM) solver has been initially verified in comparison with the NEK5000 spectral element method (SEM) solver [46]. Solvers are implemented in the cylindrical coordinates. Additionally, the new model has been compared with the DNS FDM solver implemented in the Cartesian coordinates [26]. As demonstrated later in this chapter, the effect of different coordinate systems becomes very small in the systems with large aspect ratios. The verification of the model is performed for the regimes at $Ha = 0$. Comparison with experimental and numerical data with the effect of magnetic field is discussed in section 2.3.2.

Both solvers (NEK5000 SEM and DNS FDM in the Cartesian coordinates) have been thoroughly verified and applied to non-magnetic and high$-Ha$ flows with and without convection effects in recent studies such as [14, 17, 26, 47, 48]. Agreement in terms of time-averaged integral characteristics of the flow, such as temperature, kinetic energy and the Nusselt number. The latter is determined as follows

$$Nu = \sqrt{RaPr}\langle u_z T\rangle_{A,t} - \langle\frac{dT}{dz}\rangle_{A,t}, \tag{2.6}$$

where $\langle\cdot\rangle_{A,t}$ stands for averaging over time and horizontal cross-section, has been achieved.

The following control parameters are used for comparison with the results obtained by the SEM: $Ra = 10^6$ and 10^7, $Pr = 0.7$, $Ha = 0$ and $\Gamma = 1/2$. The turbulent flow pattern can be seen on instantaneous temperature iso-surfaces for two regimes (see figure 2.4). The simulations at two Rayleigh numbers show that the results obtained with the FDM in the cylindrical coordinates converge to those obtained by the SEM as the resolution increases. This is true for vertical mean profiles of the Nusselt number $\langle Nu(z)\rangle_{A,t}$ (see figure 2.5*a*), temperature $\langle T(z)\rangle_{A,t}$ (see figure 2.5*b*), the convective flux $\langle u_z T(z)\rangle_{A,t}$ (see figure 2.5*c*) and the diffusive heat flux $\langle\frac{dT}{dz}(z)\rangle_{A,t}$ (see figure 2.5*d*).

As a further verification, comparison is made with the DNS in the Cartesian coordinates

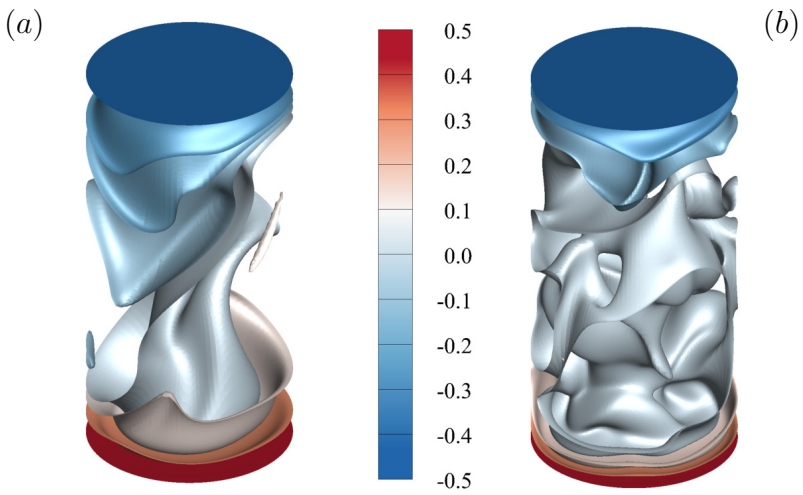

Figure 2.4: Results obtained with DNS FDM solver in the cylindrical coordinates. Instantaneous temperature iso-surfaces for turbulent flows at $Ha = 0$, $Ra = 10^6$ (a) and $Ra = 10^7$ (b). The aspect ratio is $\Gamma = 1/2$.

performed for a square domain with $\Gamma = 4$ [26]. The control parameters $Ra = 10^7$, $Pr = 0.7$ and $Ha = 0$ are chosen. The effect of different geometries expected to become insignificant at larger aspect ratios. The results of verification for a vertical cylinder and a rectangular cell prove that point. Quite good similarity between the profiles of the Nusselt number (see figure 2.6*a*) , temperature (see figure 2.6*b*) , the convective flux (see figure 2.6*c*) and kinetic energy $\frac{1}{2}\langle u_i^2(z)\rangle_{A,t}$ (see figure 2.6*d*) are presented.

2.2.3 Numerical Simulations

The equations (2.1)−(2.5) were solved for an unsteady evolving flow. Each simulation starts with the linear temperature distribution (bottom of a vertical cylinder is heated), to which random small-amplitude ($\sim 10^{-3}$) random perturbations of temperature are added. The non-magnetic flows are taken as initial conditions for magneto-convection flows.

The flow evolution consists of the convection instability, nonlinear saturation and then, evolution of fully developed flow. It must be stressed that fully developed convection ensues at large enough Ra when the pattern of convection loses its global order (i.e., spatial periodicity). The typical flow evolution is presented by the curves of average kinetic en-

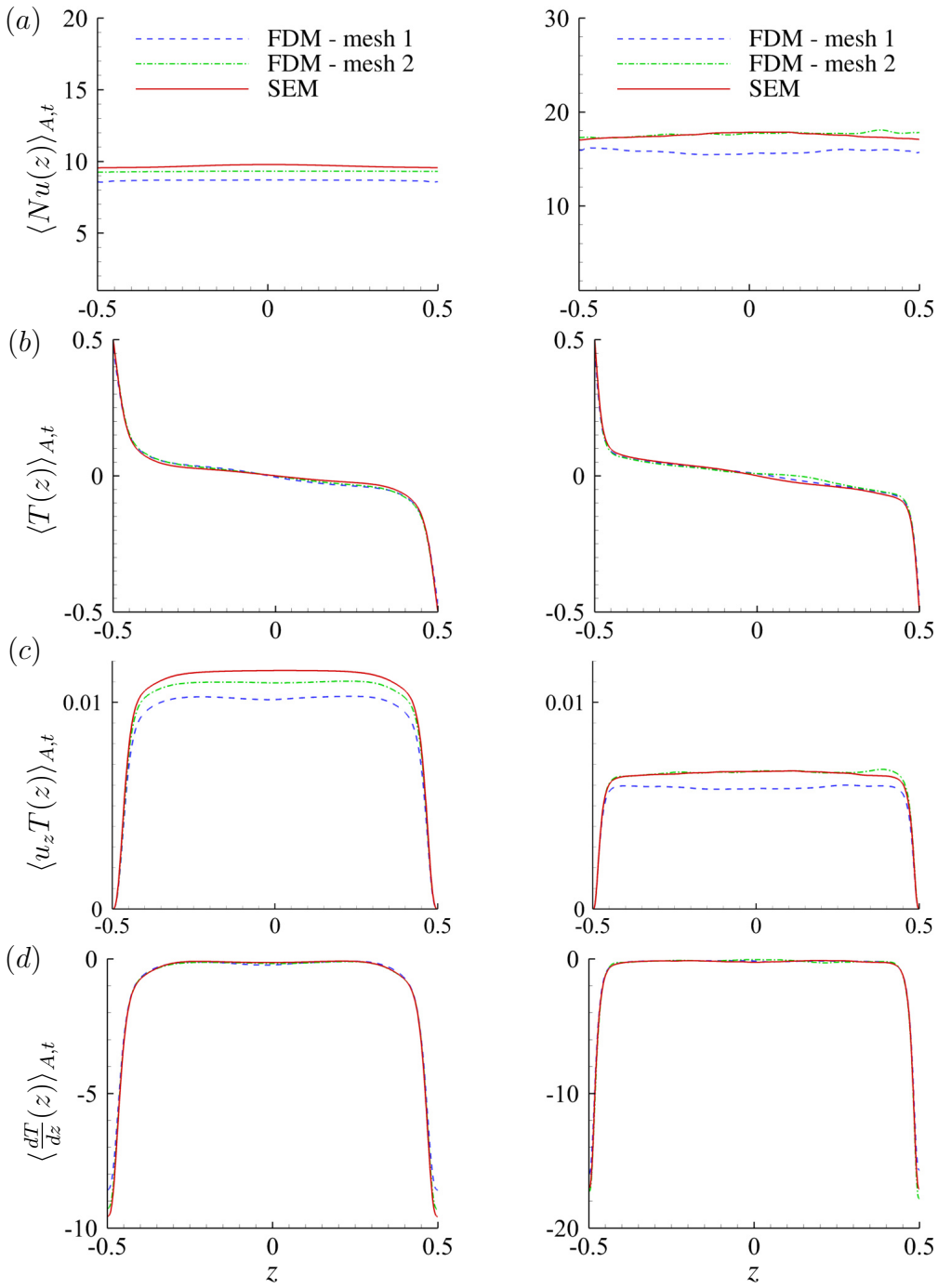

Figure 2.5: Comparison with the results obtained using the SEM code [46]. Results of simulations for the vertical mean profiles of the Nusselt number (a), temperature (b), the convective flux (c) and the diffusive heat flux (d) for turbulent flows at $Pr = 0.7$, $Ha = 0$, $Ra = 10^6$ (left column) and $Ra = 10^7$ (right column). SEM [46] on a grid of $N_e = 61440$ elements with a polynomial order of 5 (left column) and 7 (right column). FDM: mesh 1 - $N_r \times N_z \times N_\theta = 64 \times 128 \times 48$, mesh 2 - $N_r \times N_z \times N_\theta = 192 \times 384 \times 128$ (left column); mesh 1 - $N_r \times N_z \times N_\theta = 64 \times 128 \times 48$, mesh 2 - $N_r \times N_z \times N_\theta = 256 \times 512 \times 192$ (right column). The aspect ratio is $\Gamma = 1/2$.

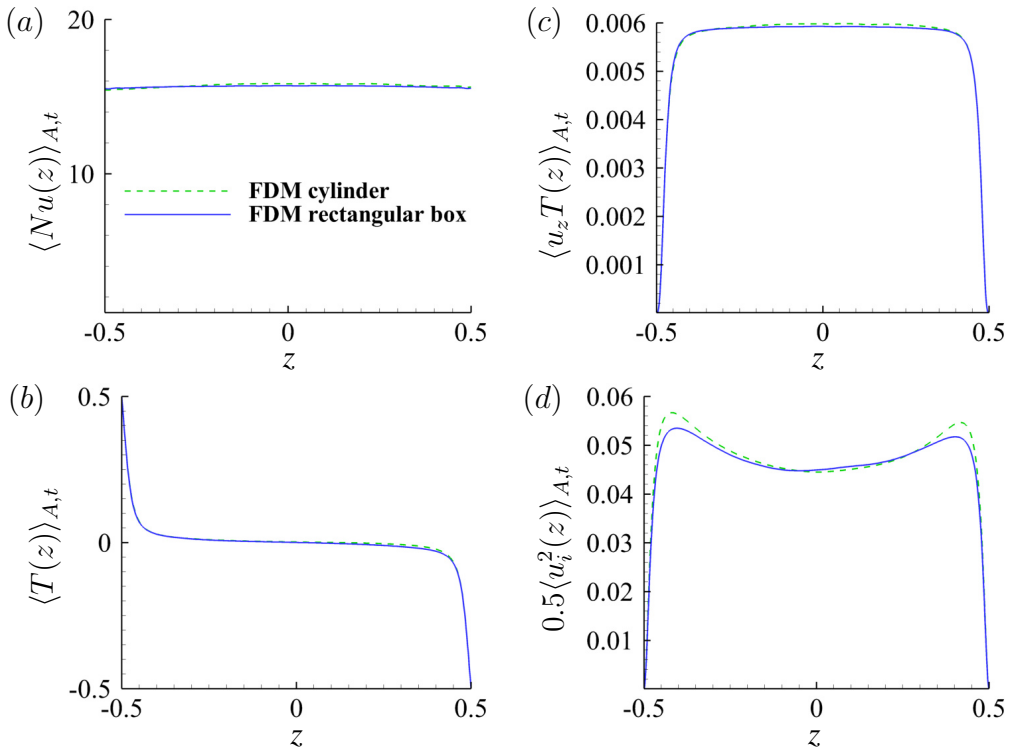

Figure 2.6: Comparison with the results obtained using the FDM code in the Cartesian coordinates [26]. Results of simulations for the vertical profiles of the mean Nusselt number (a), temperature (b), the convective flux (c) and kinetic energy (d) at $Ha = 0$, $Pr = 0.7$, $Ra = 10^7$: mesh for a cylindrical cavity - $N_r \times N_z \times N_\theta = 384 \times 192 \times 384$ and for a square cell - $N_r \times N_z \times N_\theta = 768 \times 192 \times 768$. The aspect ratio is $\Gamma = 4$.

ergies shown in figure 2.7. At this stage, the integral parameters fluctuate around steady means. The volume-averaged kinetic energies of radial, vertical and azimuthal velocities are computed as follows

$$E_r = V^{-1}\int_V u_r^2 dV, \quad E_z = V^{-1}\int_V u_z^2 dV, \quad E_\theta = V^{-1}\int_V u_\theta^2 dV. \tag{2.7}$$

All the results presented further are for the stage of a fully developed flow. The evolution of the fully developed flow is computed for at least 300 time units for the regimes at $Ha = 0$ and at least 100 time units for the regimes with the effect of magnetic field. Global transport properties of momentum and heat transfer are quantified by the Reynolds number

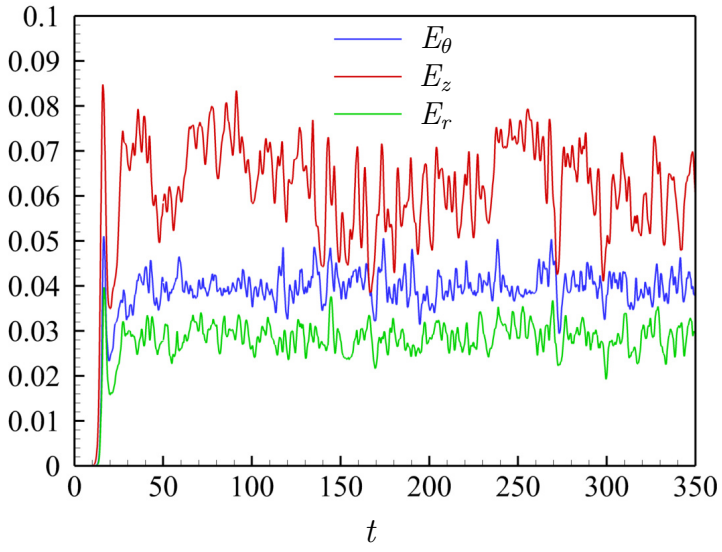

Figure 2.7: Time signals of the kinetic energies of the radial E_r (green line), vertical E_z (red line) and azimuthal E_θ (blue line) velocity components obtained in the DNS of flow at $Ra = 10^7$, $Ha = 0$.

and the Nusselt number

$$Re = u_{rms}\sqrt{\frac{Ra}{Pr}}, \tag{2.8}$$

$$Nu = 1 + \sqrt{\frac{Ra}{Pr}}\langle u_z T\rangle_{V,t}, \tag{2.9}$$

where $u_{rms} = \langle u_r^2 + u_z^2 + u_\theta^2\rangle_{V,t}$ is the root-mean-square velocity and $\langle\cdot\rangle_{V,t}$ stands for volume and time averaging, respectively.

2.2.4 Grid Sensitivity Study

The grid requirements and the grids used in the simulations are discussed in this section. The conclusions are based on the grid sensitivity study are summarized in table 2.1. In addition to internal structure of the flow, four boundary layers need to be accurately resolved [1, 49]: (i) the thermal boundary layer of thickness $\delta_T \approx 1/(2Nu)$ at the top and bottom walls, (ii) the viscous boundary layer with $\delta_v \approx 1/(4\sqrt{Re})$ at the top and bottom walls, (iii) the Shercliff layer with $\delta_{Sh} = 1/\sqrt{Ha}$ at the lateral wall, and (iv) the Hartmann layer with $\delta_{Ha} = 1/Ha$ at the top and bottom walls. The number of grid points inside

the smallest thickness, which is δ_v for the cases with $Ha = 0$ and δ_{Ha} for the cases with $Ha > 0$ is shown as N_{BL}.

Run	Ra	Ha	$N_r \times N_z \times N_\theta$	A_z	N_{BL}	Nu	Re
1	10^7	0	$128 \times 128 \times 128$	3.0	8	10.52	7179
2	10^7	0	$192 \times 192 \times 192$	3.0	12	10.31	7075
3	10^8	0	$192 \times 192 \times 192$	3.0	8	19.68	20428
4	10^8	0	$256 \times 256 \times 256$	3.0	11	19.51	20408
5	10^9	0	$192 \times 192 \times 192$	3.0	5	40.47	59689
6	10^9	0	$256 \times 256 \times 256$	3.0	7	40.57	63434
7	10^9	0	$384 \times 384 \times 384$	3.0	11	40.85	58239
8	10^7	450	$192 \times 64 \times 192$	4.0	8	5.16	2513
9	10^7	450	$192 \times 96 \times 192$	3.5	8	5.43	2281
10	10^7	450	$192 \times 192 \times 192$	3.0	7	5.35	2202
11	10^7	650	$192 \times 64 \times 192$	4.0	6	3.86	1616
12	10^7	650	$192 \times 96 \times 192$	3.5	6	3.84	1690
13	10^7	650	$192 \times 192 \times 192$	3.0	7	3.63	1638
14	10^8	650	$192 \times 96 \times 192$	3.5	6	13.19	8366
15	10^8	650	$192 \times 192 \times 192$	3.0	7	12.76	8369
16	10^8	650	$256 \times 256 \times 256$	3.0	10	13.32	8311
17	10^8	850	$192 \times 64 \times 192$	4.0	6	10.76	7326
18	10^8	850	$192 \times 192 \times 192$	3.0	6	10.62	7476
19	10^8	850	$256 \times 256 \times 256$	3.0	7	10.65	6842
20	10^9	850	$192 \times 96 \times 192$	4.0	9	33.67	28204
21	10^9	850	$192 \times 192 \times 192$	3.0	6	32.60	24971
22	10^9	850	$256 \times 256 \times 256$	3.0	7	31.92	25239
23	10^9	1400	$192 \times 96 \times 192$	4.0	6	26.37	23348
24	10^9	1400	$192 \times 192 \times 192$	3.0	4	25.78	21034
25	10^9	1400	$256 \times 256 \times 256$	3.0	5	25.85	22547

Table 2.1: Grid sensitivity study.

We find that grids with $N = N_r \times N_z \times N_\theta = 192^3, 256^3$, and 384^3 and the clustering parameter $A_z = 3.0$, $C_r = 0.9$ are sufficient for non-magnetic flows at $10^7 \leq Ra < 10^8$, $10^8 \leq Ra < 10^9$, and $Ra = 10^9$, respectively. Further refinement of the grid does not lead to significant changes. At the same time, the grid sensitivity study and the comparison between the maximum grid step in the bulk with the estimates of the Kolmogorov length scale indicate that the non-magnetic flow at $Ra = 10^9$ is somewhat under-resolved. This is

viewed as acceptable because the focus of the work is on flows at high Hartmann numbers and the data convincingly shows that such regimes are well-resolved.

Our study shows that N_r and N_θ not higher than 192 and 256 grid points are needed to accurately resolve flow structures at $Ha \geq 450$ with $10^7 \leq Ra < 10^8$ and $10^8 \leq Ra \leq 10^9$, respectively. Considering the resolution along the axial coordinate, we need to take into account the Q2D character of the flow with weak axial gradients of velocity in the core (we must note that the gradients do not approach zero at high Ra even at the strongest magnetic fields) and thin Hartmann boundary layers at the top and bottom walls. This allows us to rely on grids with the smaller number of points, but stronger near-wall clustering. The grid sensitivity study shows that, depending on the value of Ha, N_z between 64 and 256 and A_z between 3 and 4 securing not less than 6 points within the Hartmann layer are sufficient. The clustering in the radial direction is kept the same $C_r = 0.9$. It secures the sufficient number of points to resolve the Shercliff layer depending on the value of Ha.

As presented in detail in table 2.1, our simulations show good grid convergence for Nu. The results for Re are less satisfactory, especially in flows with strong magnetic field effect. The structure and character of the time evolution of the flow allow us to attribute this, at least partially, to the effect of strong and slow (on the time scale of many tens of convective units; see, e.g. figure 2.8e) fluctuations of velocity. Unfeasibly large averaging times are needed to eliminate this factor.

2.3 Results

Production runs are performed at the values of Ha and Ra shown in tables 2.2 and 2.3.

2.3.1 Spatial Structure of the Flow

The flow structure for several typical cases is illustrated in figure 2.8. Flows without a magnetic field (see figures 2.8a,b) are turbulent. The spatial structure in the horizontal cross-section (middle column) and the correlation between the velocity signals measured

along a vertical line indicate the presence of a LSC with upward or downward flow zones.

The magnetic field drastically changes the flow. The suppression of small-scale velocity gradients and the formation of large-scale anisotropic structures dominating the flow is observed (see plots in the left and middle columns of figures 2.8c-f). This is associated with a reduction of amplitude and frequency of velocity fluctuations (see the plots in the right column of figures 2.8c-f) and, as it will be discussed in section 2.3.2, an increase of Nu and Re. Similar flow transformations were detected in the recent measurements of [35] and in the simulations of [26, 27] for lower Rayleigh numbers. Such transformations can also be illustrated on instantaneous temperature iso-surfaces at lower values of Ra (see figure 2.9).

The strength of the magnetic field effect determining the degree of the flow transformation correlates with the ratio between Ra and Ra_c. At $Ra \gg Ra_c$ (see figures 2.8d,f), the large-scale velocity structures are anisotropic (elongated in the direction of the magnetic field) but susceptible to three-dimensional (3D) instabilities and evolve on the background of 3D small-scale velocity fluctuations. At Ra larger, but not much larger than Ra_c (see figures 2.8c,e), the anisotropy is much stronger and 3D fluctuations are much weaker.

In the latter case, nearly Q2D upward and downward streams occupy the flow domain. Interestingly, these flows, in particular the flow at $Ra/Ra_c \approx 5$ shown in figure 2.8(e), are principally different from the other recently identified Q2D magneto-convection regimes: the wall modes of [26] and the cellular and columnar regimes found in an infinite horizontal layer by [27]. The former is not surprising, since the simulations of [26] find the wall mode regimes at $Ra/Ra_c \sim 1$ or < 1, but not at higher Ra/Ra_c. For example, the wall modes were not found at $Ra/Ra_c = 4.05$.

The discrepancy with the results of [27] obtained for an infinite horizontal layer appears more significant. Unlike the 'cells' reminiscent of the linear instability modes or the 'columns' found in their simulations, the dominant feature of the flow in figure 2.8(e) can be described as a system of ascending and descending planar jets often originating at the

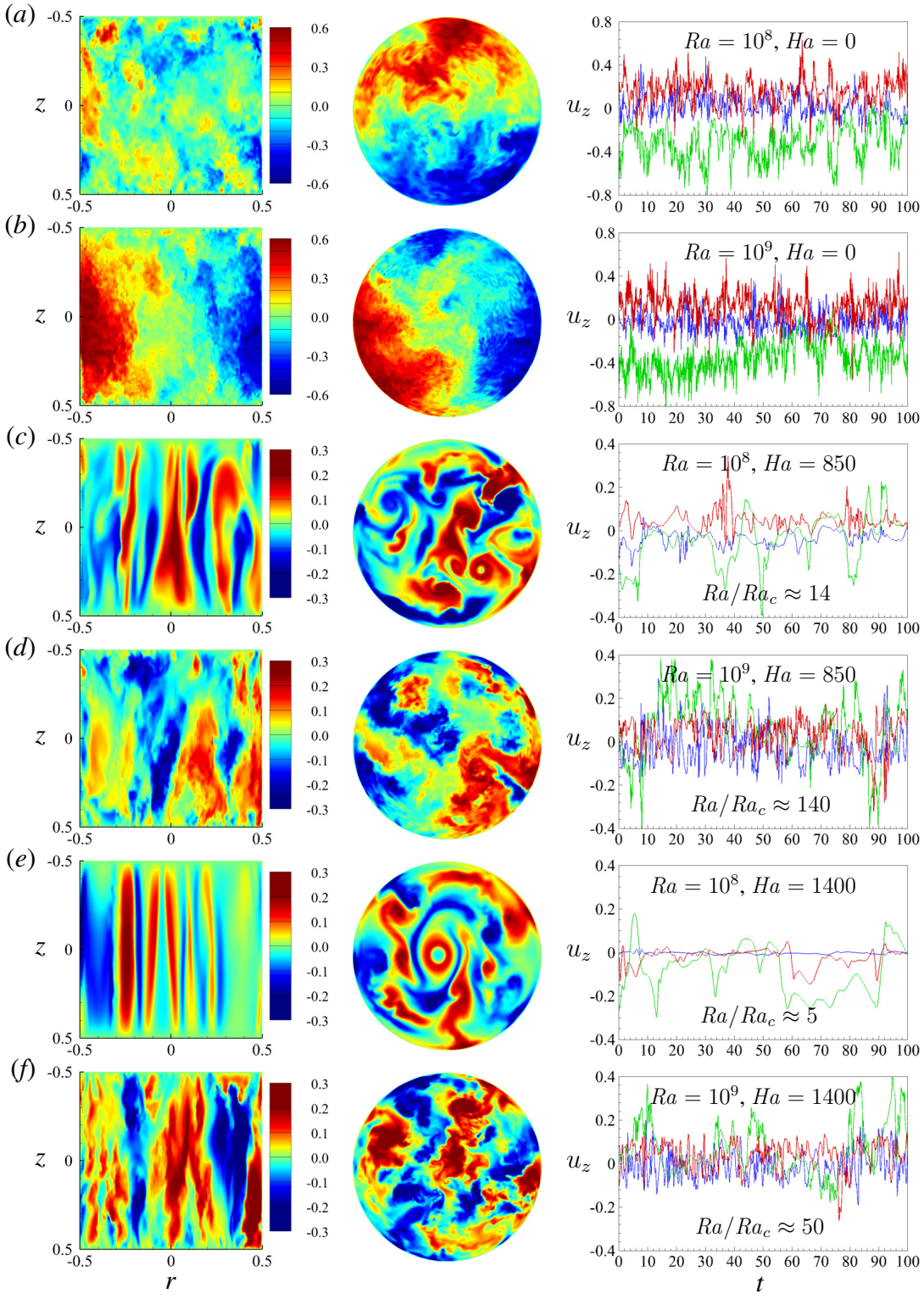

Figure 2.8: Snapshots of the vertical velocity in the vertical (left column) and horizontal mid-plane (center column) cross-sections, and time signals of u_z (right column) at $\theta = 0$, $z = 0.25$ (red line), 0 (green line), -0.25 (blue line), and $r = 0.42$ (*e*), 0.44 (*a, c, d, f*), 0.46 (*b*) are shown. The parameters Ra, Ha and the ratio between Ra and the stability limit $Ra_c \approx \pi^2 Ha^2$ [36] are indicated in the right column.

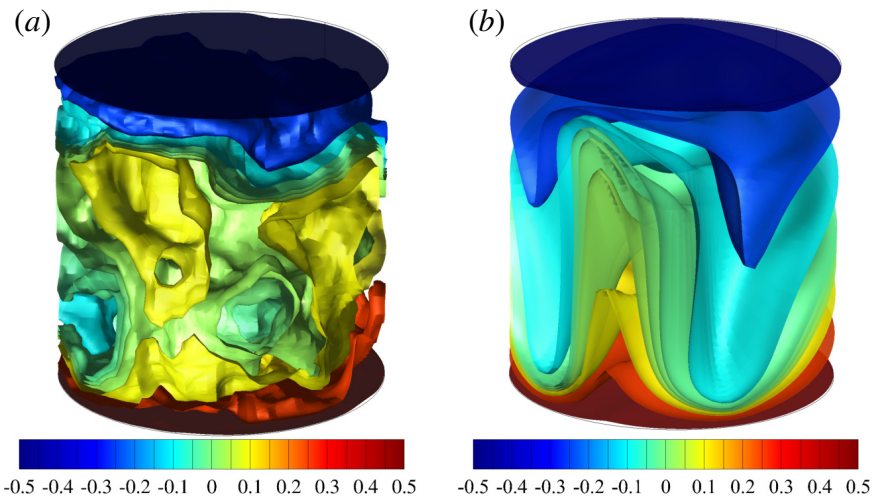

Figure 2.9: Instantaneous temperature iso-surfaces for turbulent flows at $Ra = 10^7$ for $Ha = 0$ (a) and $Ha = 850$ (b). The magnetic field is in the vertical direction.

sidewall and extending into the bulk of the flow. It should mentioned that the horizontal velocity is strong in this flow ($\langle u_r^2 + u_\theta^2 \rangle_{V,t} / \langle u_z^2 \rangle_{V,t} \approx 0.44$ in comparison to ≈ 0.27 for the case in figure 2.8f). The regime is reminiscent of Q2D extended vortex sheets often found in MHD turbulent flows with strong magnetic field effect (see, e.g., [24]). The fact that this regime rather than the cellular or columnar regimes of [27] is realized in our flow can be attributed to smaller Pr ($Pr = 1$ was used by [27]) or, much more likely, the presence of sidewalls.

The wall mode regime is found in our simulations at $Ra/Ra_c \to 1$. As an illustration, figures 2.10 and 2.11 show the instantaneous distributions of convective flux $u_z T$ and Instantaneous convective flux $u_z T$ iso-surfaces, respectively, in flows with $Ra = 10^7$ (also used by [26]) and several values of Ha.

The structure of the wall modes is qualitatively similar to the structure observed by [26] (see figure 2.10c). Significant flow and heat transfer are limited to tongue-like zones attached to the sidewall. There are noticeable differences, though. The entire wall-mode structure rotates clockwise or anticlockwise in our system. The effect of rotation is illustrated by the almost axisymmetric distribution of the time-averaged heat flux shown in figure 2.12. The travelling waves in the azimuthal direction were not observed in the linear

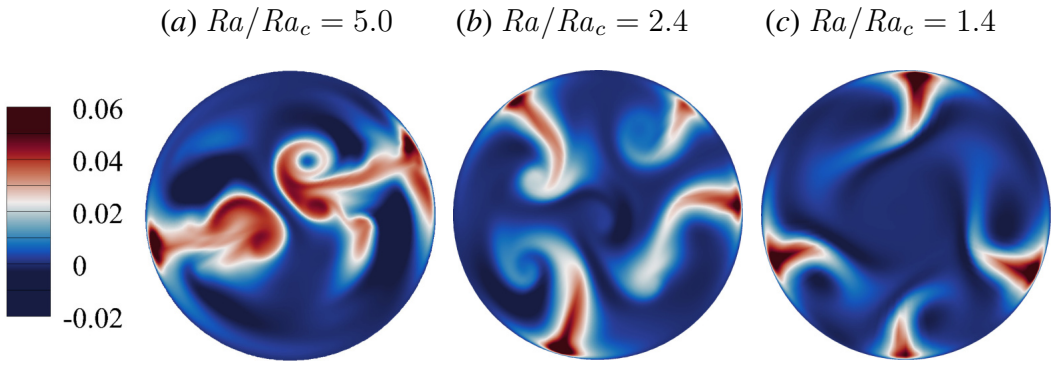

Figure 2.10: Snapshots of the convective flux $u_z T$ in the horizontal mid-plane of the cylinder at $Ra = 10^7$: $Ra/Ra_c = 5.0$, $Ha = 450$ (*a*), $Ra/Ra_c = 2.4$, $Ha = 650$ (*b*), $Ra/Ra_c = 1.4$, $Ha = 850$ (*c*).

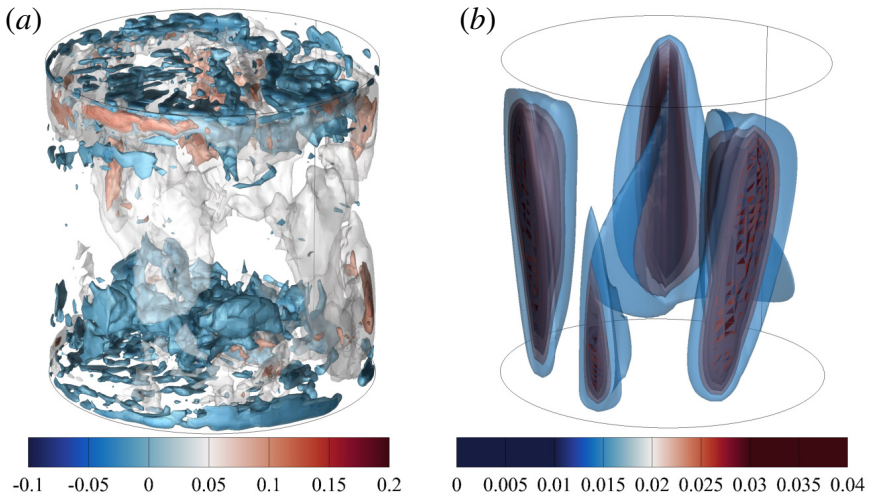

Figure 2.11: Instantaneous convective flux $u_z T$ iso-surfaces at $Ra = 10^7$ for $Ha = 0$ (a) and $Ha = 850$, $Ra/Ra_c = 1.4$ with the magnetic field in the vertical direction (b).

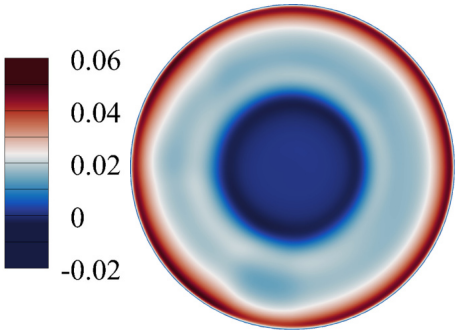

Figure 2.12: Time averaged convective flux at $Ra = 10^7$, $Ha = 850$, $Ra/Ra_c = 1.4$.

stability analysis [37] and in DNS [26]. Another difference is the transformation of wall modes at increasing Ra/Ra_c. As in the simulations of [26], the wall modes extend further from the wall. The new feature that can be plausibly attributed to rotation is that the wall-mode zones curve (see figure 2.10b) and form Q2D vortices (see figure 2.10a). We leave a detailed analysis of the properties and physical mechanisms of wall modes to future studies and only mention here that observed behaviour is qualitatively similar to that in RBC with rotation [42–44].

2.3.2 Global Transport Properties

All computed values of Nu and Re are listed in table 2.2 at $Ha = 0$ and in table 2.3 in the presence of the magnetic fields. They are also summarized and compared with the available experimental and numerical data in figures 2.13 and 2.14. The qualitative agreement between the numerical and experimental data is good. In particular, the increase of the slope of $Nu(Ra)$ and $Re(Ra)$ curves in flows with the magnetic field, which we discuss in detail below, is consistent between the simulations and the experiments. At the same time, the quantitative agreement is less convincing, with the computed values being consistently higher than in the experiments, especially in the experiment [31]. This situation is typical for thermal convection in low$-Pr$ fluids and can be attributed to several known difficulties of the experimental procedure (see [9]): (1) the ideal boundary conditions of constant temperature at the top and bottom plates cannot be accurately maintained; (2) the temperatures at the top and bottom boundaries are not measured directly, which usually leads to a slight overestimation of the Rayleigh number; (3) complete avoidance of heat losses through the sidewall is impossible; and (4) physical properties within a system are not constant, which results in inaccurate estimates of the Prandtl, Hartmann and Rayleigh numbers.

Estimates of the scaling behaviour of Nu and Re based on the data of our simulations are presented in table 2.4. Some of the respective lines are also shown in figure 2.13. The common regression method is applied to the computed time-averaged values to determine

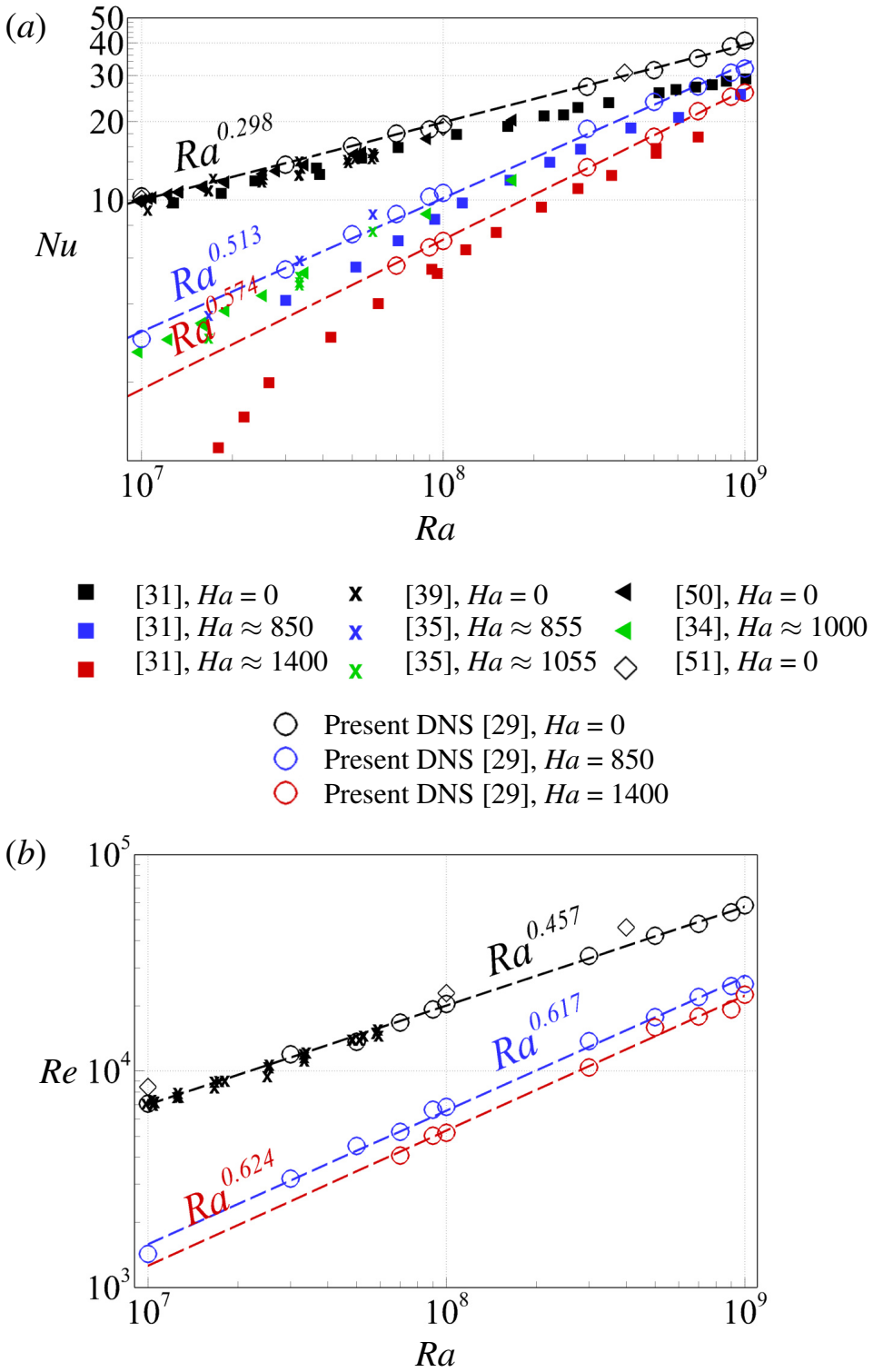

Figure 2.13: Nusselt number Nu vs Ra (a) and Reynolds number Re vs Ra (b) with and without magnetic field. Experimental [31, 34, 35, 39, 50] and numerical [29, 51] data for $\Gamma = 1$ are shown for comparison. Slope lines $\backsim Ra^{\beta}$ are plotted for guidance.

Ra	Nu	Re	$\delta_T \times 10^2$	$\delta_T^{DNS} \times 10^2$
10^7	10.31	7075	4.848	4.848
3×10^7	13.68	11929	3.655	3.650
5×10^7	16.09	13637	3.107	3.118
7×10^7	17.97	16768	2.783	2.785
9×10^7	18.67	19239	2.677	2.684
10^8	19.51	20408	2.562	2.547
3×10^8	27.16	34055	1.841	1.845
5×10^8	31.48	42203	1.588	1.588
7×10^8	34.94	47814	1.431	1.439
9×10^8	38.80	54015	1.289	1.295
10^9	40.85	58239	1.224	1.235

Table 2.2: Global transport properties at $Ha = 0$, $10^7 \leq Ra \leq 10^9$.

the exponents β_{Nu} and β_{Re} and their standard errors, and the constants α_{Nu} and α_{Re} in the following approximations

$$Nu \approx \alpha_{Nu} Ra^{\beta_{Nu}}, \tag{2.10}$$

$$Re \approx \alpha_{Re} Ra^{\beta_{Re}}. \tag{2.11}$$

For flows with $Ha = 0$, some disagreement with the data of experiments [31] is found (see figure 2.13a). At the same time, the computed value of β_{Nu} is in a good agreement with the value 0.29 ± 0.01 for $Pr = 0.025$ found in the experiments [52] performed at $\Gamma = 0.5, 1, 2$ with the largest range $2 \times 10^5 \leq Ra \leq 8 \times 10^{10}$. The exponent β_{Re} is consistent with 0.46 ± 0.02 for $Pr = 0.025$ and 0.42 ± 0.03 for $Pr = 0.029$ found in measurements [53] and [39], respectively, and with 0.45 ± 0.04 for $Pr = 0.021$ in numerical simulations [51].

An imposed magnetic field reduces the rate of heat transfer and kinetic energy in the entire studied range of *Ra*. At the same time, growth of Nu and Re with Ra becomes faster at higher Ha. In particular, the slope β_{Nu} increases from 0.298 at $Ha = 0$ to approximately 0.574 at $Ha = 1400$. A similar increase is observed for β_{Re} (see table 2.4 and figure 2.13).

Ha	Ra	Nu	Re	$\delta_T \times 10^2$	$\delta_T^{DNS} \times 10^2$
450	10^7	5.24	2234	9.548	9.610
450	3×10^7	8.64	4583	5.785	5.801
450	5×10^7	11.04	6480	4.528	4.531
450	7×10^7	12.95	8100	3.862	3.898
450	9×10^7	14.94	8911	3.346	3.363
450	10^8	14.98	9711	3.337	3.326
450	3×10^8	23.88	18686	2.094	2.108
450	5×10^8	28.98	24096	1.725	1.745
450	7×10^8	32.88	29430	1.520	1.546
450	9×10^8	35.59	33187	1.405	1.439
450	10^9	36.98	33753	1.352	1.379
650	10^7	3.84	1632	13.026	13.126
650	3×10^7	6.77	3805	7.389	7.439
650	5×10^7	9.06	5233	5.521	5.526
650	7×10^7	10.47	5946	4.776	4.812
650	9×10^7	11.84	7790	4.222	4.237
650	10^8	12.59	8549	3.971	4.001
650	3×10^8	21.31	14844	2.346	2.357
650	5×10^8	26.29	18958	1.902	1.925
650	7×10^8	30.48	23278	1.640	1.661
650	9×10^8	33.76	25829	1.481	1.498
650	10^9	35.15	27810	1.423	1.444
850	10^7	2.93	1429	17.090	17.119
850	3×10^7	5.41	3188	9.242	9.272
850	5×10^7	7.39	4507	6.770	6.773
850	7×10^7	8.84	5240	5.654	5.645
850	9×10^7	10.30	6634	4.855	4.830
850	10^8	10.65	6842	4.695	4.724
850	3×10^8	18.78	13734	2.662	2.676
850	5×10^8	23.77	17749	2.103	2.118
850	7×10^8	27.26	21971	1.834	1.843
850	9×10^8	30.79	24724	1.624	1.632
850	10^9	31.92	25239	1.566	1.563
1400	7×10^7	5.60	4066	8.921	8.950
1400	9×10^7	6.58	5022	7.593	7.743
1400	10^8	6.97	5190	7.172	7.182
1400	3×10^8	13.36	10402	3.742	3.749
1400	5×10^8	17.49	15886	2.858	2.883
1400	7×10^8	21.89	17892	2.284	2.301
1400	9×10^8	24.86	19256	2.011	2.008
1400	10^9	25.85	22547	1.934	1.949

Table 2.3: Global transport properties at $450 \leq Ha \leq 1400$, $10^7 \leq Ra \leq 10^9$.

Ra	Ha	α_{Nu}	β_{Nu}	α_{Re}	β_{Re}
$10^7 - 10^9$	0	0.0819	0.298 ± 0.005	4.427	0.457 ± 0.006
$10^7 - 10^9$	450	0.0064	0.420 ± 0.008	0.192	0.586 ± 0.010
$10^7 - 10^9$	650	0.0019	0.476 ± 0.007	0.139	0.591 ± 0.018
$10^7 - 10^9$	850	0.0008	0.513 ± 0.009	0.076	0.617 ± 0.012
$10^8 - 10^9$	1400	0.0002	0.574 ± 0.009	0.054	0.624 ± 0.033

Table 2.4: Scaling coefficients in the approximations $Nu \approx \alpha_{Nu} Ra^{\beta_{Nu}}$ and $Re \approx \alpha_{Re} Ra^{\beta_{Re}}$ based on the data of the present simulations (see figure 2.13).

The results are consistent with the data of [31], the only experiment in our range of interest of Ra and Ha.

The Nusselt number $\widetilde{Nu}$ and the Reynolds number $\widetilde{Re}$ numbers normalized by their reference values at $Ha = 0$ according to the formulas below are shown in figure 2.14.

$$\widetilde{Nu} = \frac{Nu - 1}{Nu_{Ha=0} - 1}, \tag{2.12}$$

$$\widetilde{Re} = \frac{Re}{Re_{Ha=0}}. \tag{2.13}$$

The universal scaling behaviour of $\widetilde{Nu} = 1/(1 + \alpha_{\widetilde{Nu}}(Ha/Ha_c)^{\beta_{\widetilde{Nu}}})$ and $\widetilde{Re} = 1/(1 + \alpha_{\widetilde{Re}}(Ha/\sqrt{Ha_c})^{\beta_{\widetilde{Re}}})$ where $Ha_c \equiv \sqrt{Ra}/\pi$ was proposed in [35]. To verify this hypothesis, we plot $1/\widetilde{Nu} - 1$ and $1/\widetilde{Re} - 1$ vs $Ha/Ra^{1/2}$ in logarithmic scales. The various parameters of the form $(Ra/Ha)^{\gamma}$ have been tried in [31]. The parameter Ra/Ha can be interpreted as the Rayleigh number constructed with the magnetic diffusivity η. It is relevant for the regimes where magnetic effects dominate viscous effect. The computed data provide $\beta_{\widetilde{Nu}} = 1.305 \pm 0.049$ and $\beta_{\widetilde{Re}} = 0.549 \pm 0.034$.

A good qualitative agreement between our simulations and the experiments, especially the experiments [31], is observed in figure 2.14a. Some deviations are observed The results indicate that a universal power is approached for flows at high Rayleigh numbers. At the same time, the standard error is higher and the coefficient of determination (R^2) is

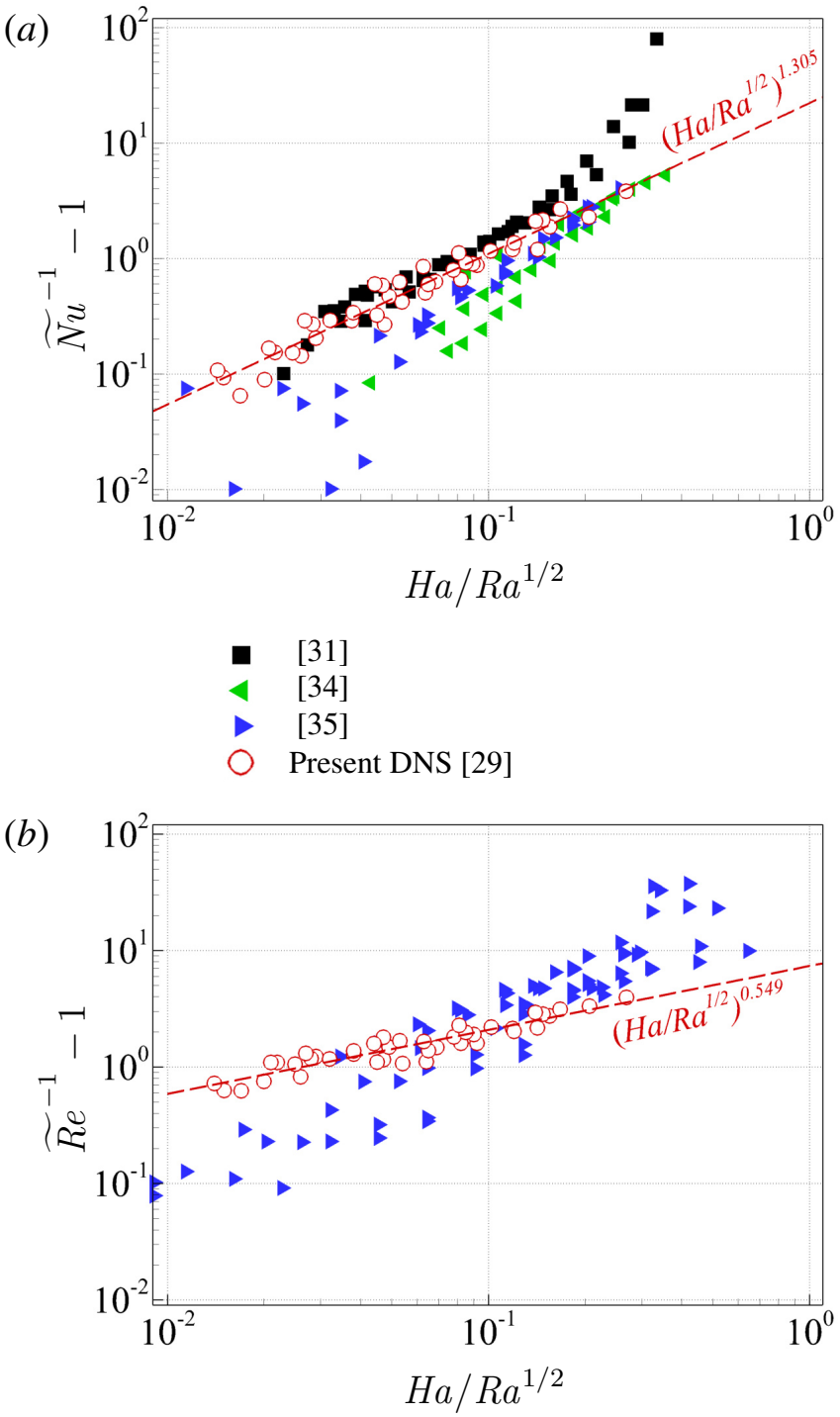

Figure 2.14: Normalized Nusselt number $\widetilde{Nu}$ vs $Ha/Ra^{1/2}$ (a) and Reynolds number $\widetilde{Re}$ vs $Ha/Ra^{1/2}$ (b). Experimental data [31, 34, 35] $\Gamma = 1$ are shown for comparison. Slope lines $\backsim (Ha/Ra^{1/2})^{\beta}$ are plotted for guidance.

lower than for the scaling $Nu \sim Ra^{\beta_{Nu}}$ presented above ($R^2 = 0.943$ in comparison to $R^2 = 0.998$ for $Nu \sim Ra^{\beta_{Nu}}$ at $Ha = 1400$). A similar situation is seen for the normalized Reynolds numbers in figure 2.14b.

It must be stressed that deviations of the normalized values of Nusselt and Reynolds numbers from the proposed power laws is insignificant in comparison with the experiments [31, 34, 35]. It can be attributed to difficulties of the experimental procedure mentioned at the beginning of this section.

Increase of the exponents $\beta_{\widetilde{Nu}}$ and $\beta_{\widetilde{Re}}$ in the wall mode regime at $Ra \sim Ra_c$ ($Ha/Ra^{1/2} \sim 0.25$) is expected. However the measurements of [35] for $1/\widetilde{Re}-1$ show a line with a higher slope $\sim (Ha/Ha_c)^{1.73\pm0.05}$ for a wide range of Ra and Ha. The discrepancy with this result and the presence of even stronger deviations in experimental data for moderate Ra can be attributed to the limitations of the ultrasound Doppler velocimetry (UDV) used to probe the flow field discussed in [35].

The estimates of the thickness of the thermal boundary layer are presented in tables 2.2 and 2.3. The common slope method used in the experiments [53] and simulations [26] is applied, i.e. the intersection point of the tangent of the time-averaged mean temperature profile near the sidewall and the horizontal line drawn through the mean value is taken. It should be mentioned here that the results of the present simulations deviate by no more than 2% from the theoretical value $\delta_T \approx 1/(2Nu)$ in [49], even in the presence of a magnetic field.

2.4 Concluding Remarks

The new computational model for MHD convection flows in cylindrical geometries based on the highly conservative finite-difference scheme [13, 20] was developed. The model underwent successful verification based on comparison with earlier simulations by the spectral element and finite difference methods.

The model was used to perform DNS of Rayleigh-Bénard convection in a cylinder with

an imposed vertical magnetic field. The range of high Ra and Ha never previously explored in numerical simulations was considered. The computations were performed on large grids with adequate numerical resolution of internal features and boundary layers.

A new flow regime with nearly Q2D upward and downward planar jets originating at the sidewalls and extending into the flow domain is identified at Ra larger, but not much larger, than the theoretic limit of convection instability in an infinite horizontal layer $Ra_c \approx \pi^2 Ha^2$ [36]. The structures are reminiscent of Q2D extended vortex sheets found in MHD turbulence (see, e.g., [24]). The results also show the existence of rotating tongue-like wall modes at $Ra \to Ra_c$, in an apparent qualitative similarity with rotating RBC [43, 44].

The results of the DNS are consistent with available experimental and numerical data. In particular, we find faster growth of Nu and Re with Ra in flows with strong magnetic fields. This effect can only be plausibly attributed to the formation of coherent large-scale Q2D structures in the flow field (see section 3.3.1) and can explain the counterintuitive phenomenon of having comparable heat transfer rates in the flow with and without magnetic field found in experiments [31].

The scaling laws for normalized Nusselt and Reynolds numbers reveal the same tendency as the experimental data, namely that the global transport properties approach a universal power law at $Ra \gg Ra_c$, and that the exponent increases with Ha in flows with a strong magnetic field.

CHAPTER 3

Poiseuille-Rayleigh-Bénard Flow

The computational results presented later in this chapter are published in [54].

3.1 Motivation and Review

The mixed convection flow in a horizontal duct with bottom heating and strong transverse magnetic field is considered (see figure 3.1). The flow is controlled by four dimensionless parameters: the Reynolds, Prandtl, Grashof and Hartmann numbers (see section 1.4). Rectangular duct geometry adds the aspect ratio $\Gamma = 2d/h$ as a parameter, where h is the height of the duct.

Many aspects of the transformation of flows of electrically conducting fluid under the influence of a strong magnetic field, such as suppression of turbulent fluctuations, anisotropic or quasi-two-dimensional (Q2D) states with zero or weak velocity gradients along the field lines, formation of MHD boundary layers and delay of laminar-turbulent transition, are relatively well understood [**?**, see, e.g.,]]Branover78, Davidson16, Sommeria82, Zikanov14. The work presented in this chapter addresses a recently discovered and still poorly understood phenomenon – the high amplitude fluctuations in flows in ducts and pipes [**?**, see, e.g.,]]Genin11Pamir,Vetcha13,Zikanov13,Belyaev21. The term magneto-convective fluctuations (MCFs) proposed for the phenomenon [55] will be used in this chapter. As discussed in detail in the review [9] and references therein, the fluctu-

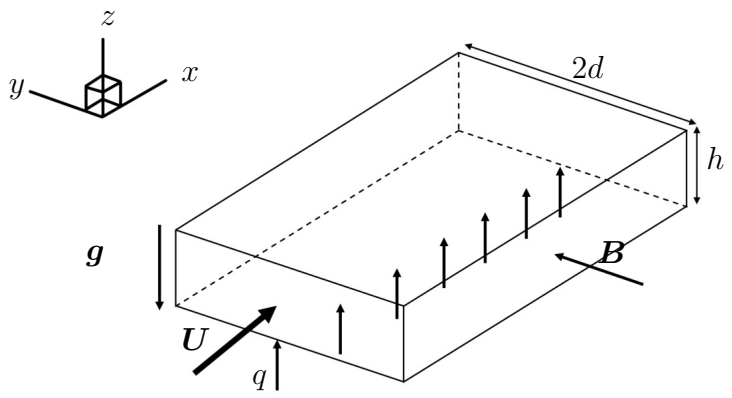

Figure 3.1: Flow geometry and coordinate system. The arrows marked by letters $\boldsymbol{g}$, $\boldsymbol{B}$ and q denote, respectively, the orientations of the gravity acceleration, magnetic field and wall heating.

ations have been detected in experimental and computational studies of a large variety of systems: pipes and ducts of various orientations with respect to gravity, various heating arrangements, and various configurations of the magnetic field.

The fluctuations were called anomalous in some earlier works, e.g., in [16] and [17]. This term now appears imprecise and somewhat misleading since it has been understood that the fluctuations are rather common. They occur in a wide variety of magnetoconvection flows. It must also be mentioned that, in a broader context, the magnetoconvective fluctuations are a part of the general phenomenon of large-amplitude fluctuations commonly found in flows, where turbulence is suppressed by a strong magnetic field and flow fields are strongly anisotropic or Q2D [**?**, see, e.g.,]for discussion and references]Smolentsev21, Zikanov21.

The magnetoconvective fluctuations appear in the conditions of a very strong magnetic field effect, i.e. in the range of Hartmann numbers, where turbulence is fully suppressed by magnetic damping. In experiments, the MCFs are manifested by oscillations of temperature with very high amplitude (up to $50K$ in some cases) and typical frequencies much lower than the frequencies of turbulence-induced fluctuations. Specific properties of the MCFs vary with the flow's configuration and values of the control parameters [9]. The effect has

potentially serious consequences for design and operation of liquid metal blankets of future fusion reactors. Should the fluctuations appear in an actual blanket, they may lead to strong and unsteady thermal stresses in the walls (see, e.g., [56]) possibly under the condition of significantly reduced strength of the wall material attributed to temperature increase [57]. Due to their possibly very large amplitude, the stresses will threaten the structural integrity of a fusion reactor system. Significant effects on heat transfer, transport of tritium, and wall corrosion are also anticipated. As it is discussed later in this section, it is yet impossible to say how realistic these expectations are, since no experiments or computations at very high Ha and Gr typical for reactor conditions have been conducted so far.

The configuration illustrated in figure 2.8 is not found in currently developed specific designs of liquid metal blankets of fusion reactors, although it may occur in future designs of an upper divertor and top blanket modules [58]. It is also important as an archetypal system, in which the MCFs were first identified (in [59] and [16], where they were named anomalous fluctuations) and explained.

Similar systems for either ducts or round pipes have been studied experimentally [59–61] and numerically [16, 17, 62, 63].

Interesting results were obtained in the linear stability analysis of the Poiseulle-Rayleigh-Bérnard duct flow with a transverse magnetic field performed by [62]. Two-dimensional approximation valid in the limit of strong magnetic field presented later in this chapter was used. One important result of [62] is relevant to our work even though different boundary conditions were used. It was demonstrated that the convection instability occurs at moderate and high Grashof number (approximately above 10^6) at the Hartmann numbers ($\sim 10^4$) typical for reactor blanket conditions.

The presence of MCFs in a horizontal round pipe with a lower half of the wall heated was detected in experiments [59,60] and explained in the linear stability analysis and direct numerical simulations (DNS) [16]. The nature of the magnetoconvective fluctuations is thoroughly described in [16]. Flows of mercury with $Pr \approx 0.022$, Re up to 10^5, Gr up to

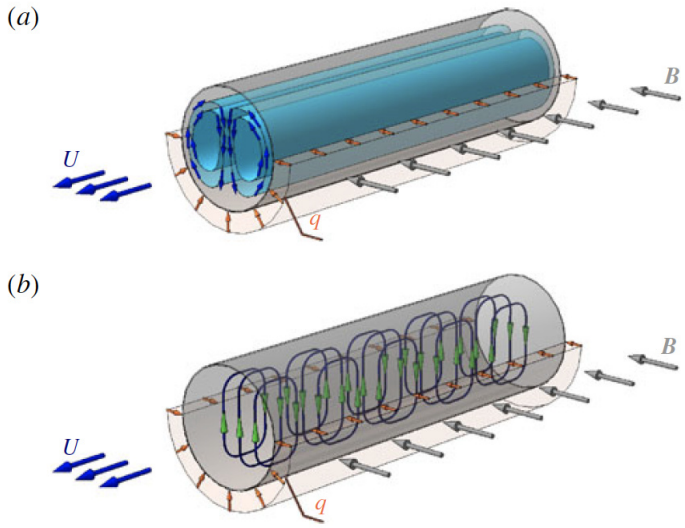

Figure 3.2: The structure of convection rolls at moderate (a) and strong (b) magnetic field [16]. Liquid metal flows in a horizontal pipe with constant uniform magnetic field $\boldsymbol{B}$ imposed in the transverse horizontal direction. The upper half of the pipe wall is thermally insulated, while the lower half is heated at a constant heat transfer rate q.

10^8, and Ha up to 500 were investigated. It was shown that at a strong magnetic field the suppression of flow structures having large gradients along the field lines resulted in the most unstable modes in the form of convection rolls with axes aligned with the field (see figure 3.2). The instability led to development of convection structures in the form of Q2D rolls. Transport of the rolls by the mean flow generated the MCFs.

Numerical simulations demonstrated that the mechanism is also realized in a square duct geometry [17]. Flows in a horizontal duct of aspect ratio $\Gamma = 1$ with bottom heating and transverse magnetic field at $Pr = 0.0321$, $Re = 5000$, $50 \leq Ha \leq 800$ and $10^5 \leq Gr \leq 10^9$ were investigated. The instability leading to the formation of Q2D rolls similar to those found in the pipe flow was detected at sufficiently high Gr and Ha.

Investigations of [17] conducted in the broader range of parameters than for the pipe flow demonstrated existence of two distinct secondary flow regimes. The realization of the regimes depended on the relative strength of the convection and MHD effects. The low$-Gr$ type characterized by Q2D distributions of velocity and temperature dominated by spanwise rolls appeared at Gr below a certain $Gr^*(Ha)$. At higher Gr, stronger con-

vection resulted in three-dimensional (3D) flow states combining the spanwise rolls with streamwise ones (the geometrically preferred convection structure in pipes and ducts with bottom heating).

Flows of liquid metals in fusion reactor blankets and divertors are subject to very strong effects of convection ($Gr \sim 10^{10} - 10^{12}$) and magnetic fields ($Ha \sim 10^4$) (see, e.g., [64, 65]). Such extreme parameters present serious obstacles to analysis, because neither laboratory experiments nor 3D simulations of unsteady flow regimes in realistic blanket or divertor geometries can, at this moment, achieve such values.

In an attempt to reach the typical blanket flow conditions, the data on two types of the secondary flow regime in a horizontal duct were extrapolated to high Gr and Ha in [17]. The extrapolation predicted the existence of MCFs at the typical blanket parameters. It also predicted that the flow would likely be of the low Gr type at $Gr \leq 10^{10}$ and of the high Gr type at higher Gr. The experiments in the pipe flow (see the review of recent results in [9]), on the contrary, indicate that MCFs may disappear at high Ha, so the extrapolation can be wrong. The nature of the convection flow at the parameters corresponding to ducts in blankets and divertors of an operating fusion reactor remains unknown, setting up the motivation for the present study.

The focus of the investigation is on the magnetoconvection in the range of very high Gr and Ha including the values typical for a reactor blanket and divertor. To the best of my knowledge, this study is the first to analyze the MCF effect in this range. Linear stability analysis and DNS of flows in a horizontal duct with $Pr = 0.025$, $Re = 5000$, $10^8 \leq Gr \leq 10^{10}$ and $10^3 \leq Ha \leq 10^4$ are performed. The study follows the work of [17], but differs by much larger values of Gr and Ha and the aspect ratio $\Gamma = 3.5$ selected to match the new experimental facility (see, e.g., [66]), on which the same configuration is to be explored at $Ha \lesssim 10^3$ and $Gr \lesssim 10^8$ in the near future. Another essential difference between the current work and the work presented in [17] is that an in-depth analysis of the accuracy of the two-dimensional approximation applied to Q2D flows at such high Ha is

carried out.

3.2 Presentation of the Problem

The flow of an incompressible, Newtonian, viscous, electrically conducting fluid (a liquid metal) with constant physical properties is considered. The fluid moves through a horizontal duct of aspect ratio $\Gamma = 3.5$ (see figure 3.1). A spatially uniform and time-independent magnetic field $\boldsymbol{B} = B\boldsymbol{e}_y$ is imposed in the horizontal transverse direction. All walls are perfectly electrically insulated. The top and side walls are perfectly thermally insulated. The bottom wall is subject to uniform heating with the heat flux of constant rate q. The no-slip boundary conditions for velocity are applied at the walls.

3.2.1 Physical Model

The governing equations are rendered non-dimensional using the duct half-width in the magnetic field direction d as the length scale, mean streamwise velocity U as the velocity scale, wall heating-based group qd/κ as the temperature scale, B as the scale of the magnetic field strength and dUB as the scale of electric potential. The equations can be written as:

$$\frac{\partial \boldsymbol{u}}{\partial t} + (\boldsymbol{u}\cdot\nabla)\boldsymbol{u} = -\nabla p - \nabla\hat{p} - \nabla\tilde{p} + \frac{1}{Re}\nabla^2\boldsymbol{u} + \boldsymbol{F}_b + \boldsymbol{F}_L, \tag{3.1}$$

$$\nabla\cdot\boldsymbol{u} = 0, \tag{3.2}$$

$$\frac{\partial\theta}{\partial t} + \boldsymbol{u}\cdot\nabla\theta = \frac{1}{RePr}\nabla^2\theta - u_x\frac{\mathrm{d}T_m}{\mathrm{d}x}, \tag{3.3}$$

where $\boldsymbol{u}$ is the velocity field. The decompositions of the temperature and pressure fields commonly used in studies of mixed convection in ducts and pipes (see, e.g., [9, 16, 17, 67, 68]) are applied. The decompositions are convenient, since they allow one to recast the problem in terms of the fluctuation fields, which are statistically uniform in the streamwise direction and, thus, study the flow in a relatively short segment of the channel with periodic

inlet-exit conditions. The temperature field is written as a sum

$$T(\boldsymbol{x},t) = T_m(x) + \theta(\boldsymbol{x},t) \tag{3.4}$$

of fluctuations θ and the mean-mixed temperature

$$T_m(x) = \frac{\int_A u_x T \mathrm{d}A}{\int_A u_x \mathrm{d}A} = A^{-1} \int\limits_A u_x T \mathrm{d}A, \tag{3.5}$$

where $A = 2h/d$ is the cross-section area of the duct. One can also use the decomposition into fluctuations and simple mean temperature $\bar{T}(x) = A^{-1}\int_A T \mathrm{d}A$. Applying the energy balance between the wall heating and the streamwise convection heat transfer, one can find that $T_m(x)$ and $\bar{T}(x)$ are linear functions with the same derivative:

$$\frac{\mathrm{d}T_m}{\mathrm{d}x} = \frac{\mathrm{d}\bar{T}}{\mathrm{d}x} = \frac{\Pi}{ARePr} = \frac{\Gamma}{2RePr}, \tag{3.6}$$

where $\Pi = 2$ is the perimeter of the heated portion of the wall.

The total pressure P is presented in (3.1) as

$$P = \hat{p}(x) + \tilde{p}(x,z) + p(\boldsymbol{x},t), \tag{3.7}$$

where $p(\boldsymbol{x},t)$ is the field of pressure fluctuations statistically homogeneous in the streamwise direction, and $\hat{p}$ is a linear function of x corresponding to the spatially uniform streamwise gradient $\mathrm{d}\hat{p}/\mathrm{d}x$ applied as a flow-driving mechanism. In the simulations discussed in this chapter, the gradient is adjusted at every time step to maintain constant mean velocity.

The second term of the decomposition becomes necessary in numerical models of mixed convection in non-vertical channels with periodic inlet–exit conditions. The component

$$\tilde{p}(x,z) = \frac{\mathrm{d}T_m}{\mathrm{d}x}\frac{Gr}{Re^2}xz = \frac{\Pi}{ARePr}\frac{Gr}{Re^2}xz, \tag{3.8}$$

arises due to the buoyancy force caused by the mean–mixed temperature T_m:

$$\boldsymbol{F}_{b,m} = GrRe^{-2}\boldsymbol{e}_z T_m, \tag{3.9}$$

where $\boldsymbol{e}_z$ is the unit vector opposite to the direction of gravity (see figure 3.1). The force has a non-zero curl and, therefore, modifies the velocity field. Its action on the flow can be described by introducing the pressure field $\tilde{p}$, such that its vertical gradient balances $\boldsymbol{F}_{b,m}$. The pressure field is a two-dimensional function increasing with the streamwise coordinate x and vertical coordinate z. Its z-dependent x-gradient, which appears in the respective momentum equation, generates a flow in the positive x-direction in the lower part of the channel and in the negative x-direction in the upper part. The result is a top$-$bottom asymmetry of the streamwise velocity profile and of the associated convection heat flux, which can dramatically change the structure of the flow at high Gr and Ha (see, e.g., [9, 16, 17, 69]).

The buoyancy force in (3.1) is

$$\boldsymbol{F}_b = GrRe^{-2}\boldsymbol{e}_z T. \tag{3.10}$$

The Lorentz force is computed as

$$\boldsymbol{F}_L = Ha^2 Re^{-1}\boldsymbol{j} \times \boldsymbol{e}_y, \tag{3.11}$$

where $\boldsymbol{e}_y$ is the unit vector along the imposed magnetic field (see figure 2.8). The electric current $\boldsymbol{j}$ is determined by the Ohm's law

$$\boldsymbol{j} = -\nabla\phi + (\boldsymbol{u} \times \boldsymbol{e}_y), \tag{3.12}$$

where the electric potential ϕ is a solution of the Poisson equation expressing the instanta-

neous electric neutrality of the fluid:

$$\nabla^2\phi = \nabla \cdot (\boldsymbol{u} \times \boldsymbol{e}_y). \tag{3.13}$$

The inlet–exit conditions are those of periodicity of the velocity $\boldsymbol{u}$, temperature fluctuations θ, pressure fluctuations p and potential ϕ.

3.2.2 Two-dimensional Approximation

Flows with a very strong imposed magnetic field are considered, so the Hartmann number and the Stuart number satisfy

$$Ha \gg 1,\ N \equiv \frac{Ha^2}{Re} \gg 1. \tag{3.14}$$

The flows are anticipated to have Q2D form with nearly zero gradients along the magnetic field lines except in the thin Hartmann layers at the walls perpendicular to the field. The 2D approximation proposed in [21] can be applied in this asymptotic limit. The problem can be expressed in terms of the variables integrated wall-to-wall along the direction of the magnetic field, leading to 2D dynamics for y-averaged quantities. The approximation has been verified and examined in [70, 71], and utilized in numerical studies of liquid metal flows in rectangular ducts (see, e.g., [18, 62, 72–74]).

The often applied abbreviation SM82 by the first letters of the surnames of the authors in [21] will be used for the model in the following. The y-independent solutions obtained in the framework of the model will be referred to as 2D solutions, while the full solutions obtained numerically without resorting to the model will be designated as 3D.

The SM82 model is derived for flows with $Ha \gg 1$ and $N \gg 1$, in domains with electrically insulating walls and constant wall-to-wall distance in the field direction. It utilizes the fact that the Lorentz force becomes nearly zero in the bulk region of Q2D flows in such geometries, and that the effect of the magnetic field on the flow is largely reduced

to thin Hartmann layers and can be accurately modelled by the linear friction term in the momentum equation.

It must be noted that the original SM82 model was developed for isothermal flows. Its extension to flows with heat transfer and temperature variations was, to our best knowledge, first proposed by [64]. As demonstrated in this and in the following studies (see, e.g., [18, 74, 75]), the model can be extended to a 2D approximation of temperature if the imposed heat flux is perpendicular to the magnetic field.

The SM82 version of (3.1)−(3.3) is

$$\frac{\partial \boldsymbol{u}}{\partial t} + (\boldsymbol{u}\cdot\nabla)\boldsymbol{u} = -\nabla p - \nabla\hat{p} - \nabla\tilde{p} + \frac{1}{Re}\nabla^2\boldsymbol{u} - \frac{Ha}{Re}\boldsymbol{u} + \frac{Gr}{Re^2}T\hat{\boldsymbol{e}}_z, \tag{3.15}$$

$$\nabla\cdot\boldsymbol{u} = 0, \tag{3.16}$$

$$\frac{\partial\theta}{\partial t} + \boldsymbol{u}\cdot\nabla\theta = \frac{1}{RePr}\nabla^2\theta - u_x\frac{\mathrm{d}T_m}{\mathrm{d}x}, \tag{3.17}$$

where all the flow variables are now 2D fields obtained by wall-to-wall averaging. The term $(Ha/Re)\boldsymbol{u}$ represents the effect of viscous friction in the thin Hartmann layers. It appears as a result of assuming the Hartmann boundary layer solution $\boldsymbol{u} \sim \exp(z/Ha)$. The same notation as in (3.1)−(3.3) is used. The boundary conditions on velocity and temperature on the remaining two wall are the same as in the 3D model.

3.2.3 Approach to Linear Stability Analysis

The base flow needs to be selected before conducting the linear stability analysis. It needs to be noted that an archetypal structure of a laminar flow with convection in a horizontal channel heated from below is a superposition of the streamwise flow $u_x(y,z)$ and one or several streamwise-uniform convection rolls $(u_y(y,z), u_z(y,z))$. At high Ha, the structure can be modified by the magnetic field and replaced by a 3D structure with the rolls aligned with the magnetic field and, thus, x-dependent velocity and temperature. Following [16] and [17], the problem is treated as that of the instability of the laminar steady-state

streamwise-uniform base flow $\boldsymbol{U}(y,z)$, $\Theta(y,z)$, $P(y,z)$ to x-dependent perturbations.

The base flow is calculated by artificially imposing uniformity in the streamwise direction, i.e. by applying x-averaging after every time step. In order to assure that a fully developed state of the base flow is reached, each solution is computed for a sufficiently long time. Long evolution, in some regimes up to 1000 time units, is typically required in order to arrive at this state. No unsteady base flow solutions have been detected in the studied range of parameters. The steady-state solutions are discussed in section 3.3.1.

The linear stability analysis is conducted using a modified version of the numerical model described in section 1.5. We follow evolution of perturbations $-$ solutions of the equations linearized around the base flow $\boldsymbol{U}(y,z)$, $\Theta(y,z)$, $P(y,z)$. Individual Fourier modes determined by their streamwise wavelength λ are computed. This is practically achieved by setting the length of the computational domain to λ and filtering out all the Fourier modes except the zero mode corresponding to the base flow and the first mode corresponding to the perturbations of wavelength λ. All simulations start with random noise distributions of velocity and temperature.

The linear instability is identified by the exponential growth of the perturbations with the growth rate determined as

$$\gamma = \frac{1}{2E'}\frac{dE'}{dt}, \tag{3.18}$$

where $E' = \langle f^2 \rangle$, $\langle \ldots \rangle$ stands for volume averaging, and f stands for perturbations of a velocity component or temperature. The growth rate coefficient is recorded after its values computed for all three velocity components and temperature coincide with each other and remain constant within the third digit after the decimal point for at least 100 time units. The results of the linear stability analysis are presented in sections 3.3.2 and 3.3.3.

3.2.4 Grid Sensitivity Study

The grid sensitivity study has been conducted for the base flow. A detailed description of the various flow regimes is provided in section 3.3.1. For the present discussion, it is sufficient to say that accurate resolution of the internal flow structure, along with two boundary layers: the Hartmann layers of thickness $\delta_{Ha} = 1/Ha$ at the vertical walls and the Shercliff layers of thickness $\delta_{Sh} = 1/\sqrt{Ha}$ at the top and bottom walls, is critically important for accurate representation of the flow behavior.

As an example, the results obtained at $Ha = 1200$, $Gr = 10^8$ are presented in table 3.1. In a fully developed steady-state flow, the integrated Lorentz and buoyancy forces are zero. The wall friction must be balanced by the driving pressure gradient according to

$$\frac{d\hat{p}}{dx} = A^{-1}\left(\tau_{Ha} + \tau_{Sh}\right), \tag{3.19}$$

where τ_{Ha} and τ_{Sh} are the computed values of the integrated friction forces at the Hartmann and Shercliff walls of the duct, respectively, expressed as

$$\tau_{Ha} = \tau_y = \frac{1}{Re}\sum_{y=\pm 1}\int_{-1/\Gamma}^{1/\Gamma}\frac{\partial U_x}{\partial y}dz, \quad \tau_{Sh} = \tau_z = \frac{1}{Re}\sum_{z=\pm 1/\Gamma}\int_{-1}^{1}\frac{\partial U_x}{\partial z}dy. \tag{3.20}$$

Values of τ_{Ha}, τ_{Sh} and the error ϵ, with which the computed solution satisfies (3.19), found on various grids are compared in table 3.1. On the basis of these data, it is concluded that the grid with $N_y \times N_z = 192 \times 96$, $A_y = 4.0$ and $A_z = 2.0$ is sufficient. The maximum and minimum grid steps of such a grid are $\Delta y_{min} \approx 0.0001$, $\Delta y_{max} \approx 0.042$, $\Delta z_{min} \approx 0.0009$, $\Delta z_{max} \approx 0.012$. The Hartmann and Shercliff layers are resolved by, respectively, 9 and 32 grid points.

The parameters of the grids in the entire studied parameter range of Ha and Gr have been determined in the same way. It has been found that the value of Gr does not affect the selection at fixed Ha. This effect can be explained by the presence of very strong magnetic

N_y	N_z	A_y	A_z	$-\tau_{Ha}$	$-\tau_{Sh}$	ϵ	N_{Ha}	N_{Sh}
128	32	4.0	2.0	0.23425	0.02914	0.00074	6	10
128	64	4.0	2.0	0.23460	0.26417	0.00070	6	21
128	64	4.3	2.0	0.23477	0.26387	0.00025	8	21
128	96	4.0	2.0	0.23468	0.26407	0.00069	6	32
128	96	4.3	2.0	0.23484	0.26377	0.00024	8	32
192	96	4.0	2.0	0.23459	0.26356	0.00030	9	32
192	128	4.0	2.0	0.23462	0.26347	0.00029	9	43

Table 3.1: Grid sensitivity study conducted for $Ha = 1200$ and $Gr = 10^8$: τ_{Ha} and τ_{Sh} are the wall friction forces, ϵ is the absolute error of the balance (3.19). The number of grid points inside the Hartmann and Shercliff boundary layers are N_{Ha} and N_{Sh}, respectively.

fields which fully suppress transverse circulation (see section 3.3.1 for a discussion). The summary of the grids used in the simulations is presented in table 3.2.

A grid sensitivity study has also been conducted to determine the minimum number of grid points N_x required in the linear stability analysis. It has been found that the growth of linear unstable modes is accurately reproduced at $N_x = 32$ for modes with $\lambda \lesssim 2$, which needs to be increased to $N_x = 64$ for greater λ.

Computational domains of length $L_x = 4\pi$ or $L_x = 2\pi$ are used in DNS of nonlinear flow regimes. As it will be seen below, these lengths are substantially larger than the streamwise wavelength of the fastest growing instability modes. The flow structures have been accurately resolved with, respectively, 384 or 192 grid points in the $x-$direction.

The time steps adjusted to secure numerical instability and, thus, varying with Ha and Gr, but never exceeding 2.5×10^{-3}, are used in linear stability and DNS simulations.

3.3 Results

3.3.1 Base Flow

The structure of the base flow, as it is defined in section 3.2.3, for several typical cases is illustrated in figures 3.3 and 3.4. The results for all the completed simulations are sum-

Ha	N_y	N_z	A_y	A_z	N_{Ha}	N_{Sh}
1000	192	96	4.0	2.0	9	32
2000	256	96	4.0	2.0	8	28
3000	384	96	4.0	2.0	9	24
4000	384	96	4.0	2.0	7	22
5000	512	96	4.0	2.0	8	20
6000	512	96	4.0	2.0	7	19
7000	512	96	4.3	2.0	9	18
8000	512	96	4.3	2.0	8	17
9000	512	96	4.3	2.0	7	16
10000	512	96	4.3	2.0	6	15

Table 3.2: Parameters of the computational grids used in the simulations for $Gr = 10^8 - 10^{10}$. The number of grid points inside the Hartmann and Shercliff boundary layers are N_{Ha} and N_{Sh}, respectively.

marized in table 3.3.

The table shows the type of flow for a particular regime (Q2D or 3D flows to be discussed shortly), the maximum and minimum values of U_x, integral quantities, such as the wall friction force $d\hat{p}/dx$, the volume-averaged kinetic energies of streamwise and transverse velocities

$$E_x = A^{-1} \int_{-1/\Gamma}^{1/\Gamma} \int_{-1}^{1} U_x^2 dydz, \quad E_t = A^{-1} \int_{-1/\Gamma}^{1/\Gamma} \int_{-1}^{1} \left(U_y^2 + U_z^2\right) dydz, \tag{3.21}$$

and the mean square of temperature perturbations

$$E_\theta = A^{-1} \int_{-1/\Gamma}^{1/\Gamma} \int_{-1}^{1} \Theta^2 dydz. \tag{3.22}$$

Similar data for flows with lower values of Gr and Ha in a duct with $\Gamma = 1$ can be found in [17].

The flow structure is predominantly determined by the effect of magnetoconvection. Similarly to the findings of [17], two regimes of the base flow depending on whether Gr is

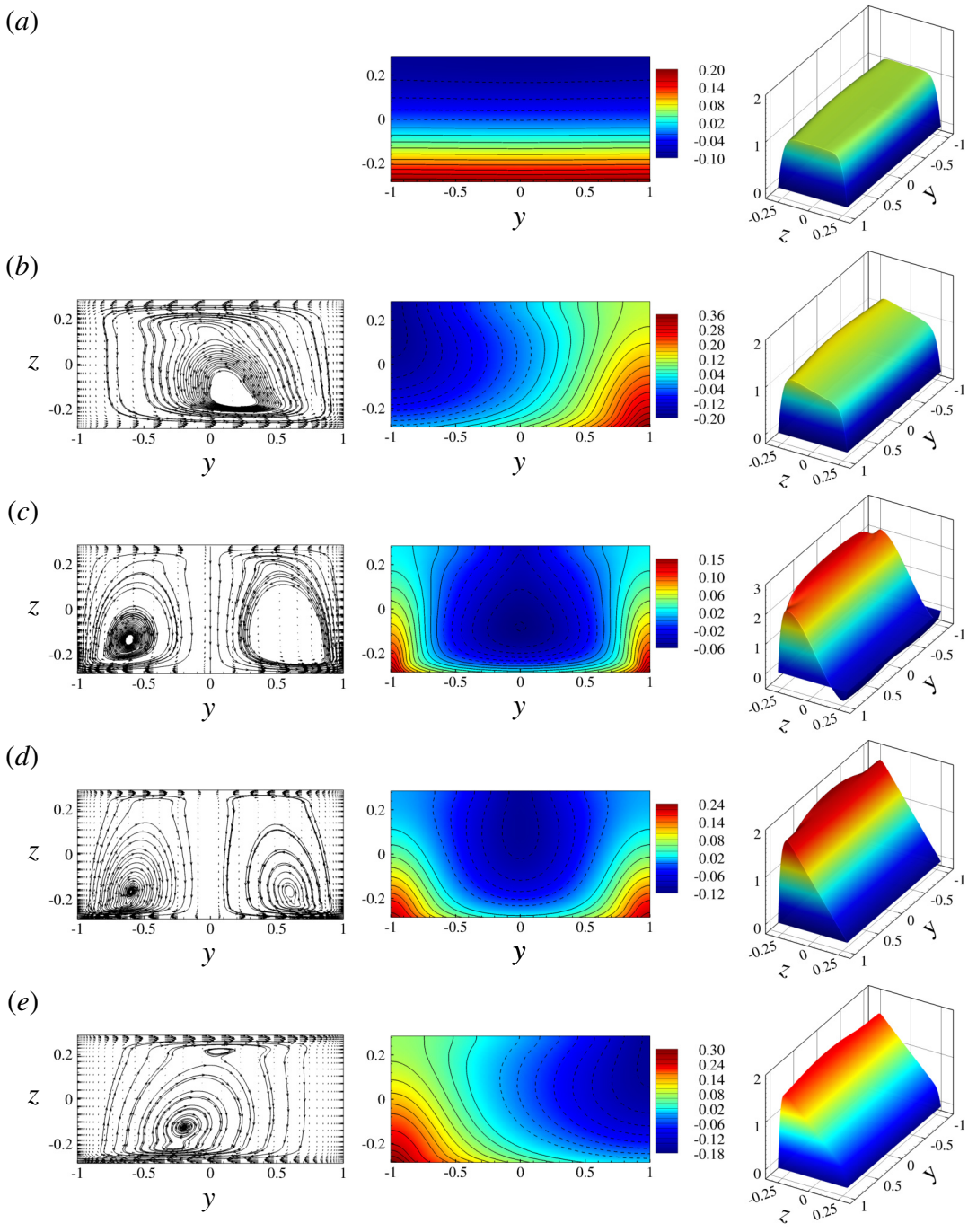

Figure 3.3: Base flow at $Ha = 1000$, $Gr = 10^8$ (a), $Ha = 1000$, $Gr = 10^9$ (b), $Ha = 1000$, $Gr = 10^{10}$ (c), $Ha = 2000$, $Gr = 10^{10}$ (d) and $Ha = 3000$, $Gr = 10^{10}$ (e). Vector fields and streamlines of transverse circulation (u_y, u_z) are shown in the left column (not in (a), since the velocity's amplitude is virtually zero in this case). The middle and right columns show distributions of temperature Θ and streamwise velocity U_x, respectively. Solid and dashed isolines in the middle column indicate positive and negative values, respectively. The wall heating is at the wall at $z = -0.2857$, and the magnetic field is in the y-direction.

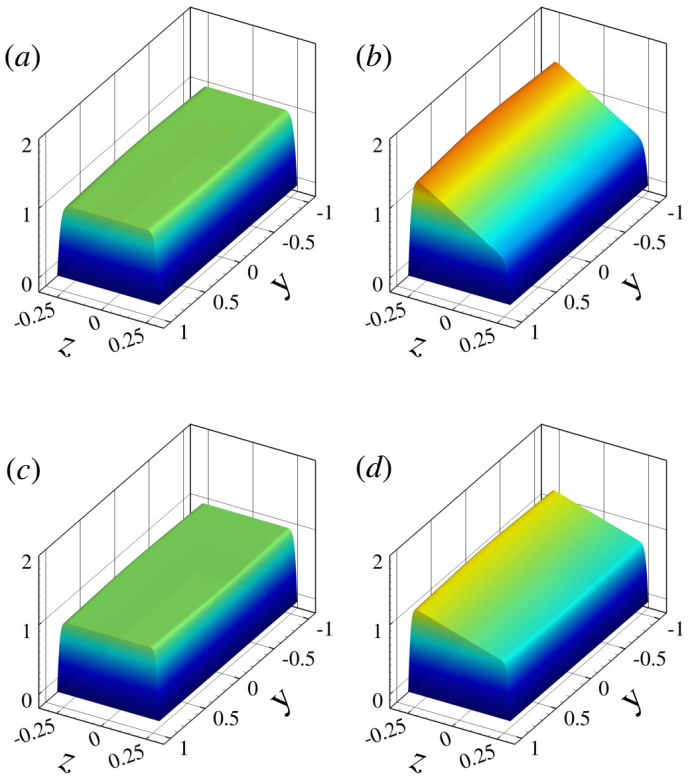

Figure 3.4: Q2D base flow at $Ha = 5000$, $Gr = 10^9$ (a), $Ha = 5000$, $Gr = 10^{10}$ (b), $Ha = 10000$, $Gr = 10^9$ (c) and $Ha = 10000$, $Gr = 10^{10}$ (d). Distribution of streamwise velocity u_x is shown. The wall heating is at the wall at $z = -0.2857$, and the magnetic field is in the y-direction.

smaller or larger than a certain threshold $Gr^*(Ha)$ are observed. The Q2D regime observed at $Gr < Gr^*$ is characterized by the transverse convection-induced circulation entirely suppressed by the strong magnetic field. The distributions of the temperature and streamwise velocity are nearly one-dimensional outside of the Hartmann boundary layers ($\Theta \approx \Theta(z)$ and $U_x \approx U_x(z)$). In the absence of transverse circulation, the distributions of temperature are determined by the balance between the heat conduction and the heat convection by U_x. Examples of this regime are shown in figure 3.3a and figure 3.4.

The 3D regime observed at $Gr > Gr^*(Ha)$, when the strength of the magnetic field is insufficient to suppress convection circulation, is characterized by significant transverse flow and fully 2D variations of temperature. (see figure 3.3$b - e$).

To avoid confusion, it is pertinent to repeat the terminology here. The terms 3D and

Ha	Gr	Gr/Ha^2	$-d\hat{p}/dx$	E_x	E_t	E_θ	$u_{x,max}$	$Regime$
1000	10^8	1.00×10^2	0.222	1.050	1.62×10^{-8}	3.59×10^{-3}	1.139	$Q2D$
1000	10^9	1.00×10^3	0.224	1.056	6.32×10^{-3}	9.31×10^{-3}	1.249	$3D$
1000	10^{10}	1.00×10^4	0.254	1.892	3.11×10^{-2}	7.11×10^{-4}	2.601	$3D$
2000	10^8	2.50×10^1	0.430	1.035	5.42×10^{-9}	3.61×10^{-3}	1.079	$Q2D$
2000	10^9	2.50×10^2	0.431	1.037	4.96×10^{-7}	3.34×10^{-3}	1.153	$Q2D$
2000	10^{10}	2.50×10^3	0.447	1.313	8.30×10^{-3}	2.19×10^{-3}	1.968	$3D$
3000	10^8	1.11×10^1	0.636	1.029	1.76×10^{-9}	3.62×10^{-3}	1.063	$Q2D$
3000	10^9	1.11×10^2	0.637	1.030	1.66×10^{-7}	3.45×10^{-3}	1.114	$Q2D$
3000	10^{10}	1.11×10^3	0.643	1.172	1.58×10^{-2}	4.48×10^{-3}	1.683	$3D$
4000	10^8	6.25×10^0	0.842	1.025	3.85×10^{-10}	3.63×10^{-3}	1.054	$Q2D$
4000	10^9	6.25×10^1	0.842	1.026	3.70×10^{-8}	3.53×10^{-3}	1.093	$Q2D$
4000	10^{10}	6.25×10^2	0.847	1.109	2.75×10^{-6}	2.96×10^{-3}	1.522	$Q2D$
5000	10^8	4.00×10^0	1.046	1.022	1.13×10^{-10}	3.63×10^{-3}	1.048	$Q2D$
5000	10^9	4.00×10^1	1.046	1.023	1.10×10^{-8}	3.57×10^{-3}	1.080	$Q2D$
5000	10^{10}	4.00×10^2	1.049	1.078	8.55×10^{-7}	3.16×10^{-3}	1.425	$Q2D$
6000	10^8	2.78×10^0	1.251	1.020	1.00×10^{-10}	3.63×10^{-3}	1.043	$Q2D$
6000	10^9	2.78×10^1	1.251	1.021	9.79×10^{-9}	3.57×10^{-3}	1.071	$Q2D$
6000	10^{10}	2.78×10^2	1.254	1.060	7.75×10^{-7}	3.18×10^{-3}	1.362	$Q2D$
7000	10^8	2.04×10^0	1.454	1.019	9.00×10^{-11}	3.63×10^{-3}	1.040	$Q2D$
7000	10^9	2.04×10^1	1.454	1.019	8.80×10^{-9}	3.58×10^{-3}	1.064	$Q2D$
7000	10^{10}	2.04×10^2	1.457	1.048	7.12×10^{-7}	3.20×10^{-3}	1.315	$Q2D$
8000	10^8	1.56×10^0	1.658	1.018	8.12×10^{-11}	3.63×10^{-3}	1.037	$Q2D$
8000	10^9	1.56×10^1	1.658	1.018	7.96×10^{-9}	3.58×10^{-3}	1.058	$Q2D$
8000	10^{10}	1.56×10^2	1.661	1.040	6.56×10^{-7}	3.22×10^{-3}	1.280	$Q2D$
9000	10^8	1.23×10^0	1.862	1.017	2.50×10^{-11}	3.63×10^{-3}	1.035	$Q2D$
9000	10^9	1.23×10^1	1.862	1.017	2.46×10^{-9}	3.60×10^{-3}	1.054	$Q2D$
9000	10^{10}	1.23×10^2	1.864	1.035	2.11×10^{-7}	3.34×10^{-3}	1.252	$Q2D$
10000	10^8	1.00×10^0	2.067	1.016	2.31×10^{-11}	3.63×10^{-3}	1.033	$Q2D$
10000	10^9	1.00×10^1	2.067	1.016	2.28×10^{-9}	3.60×10^{-3}	1.050	$Q2D$
10000	10^{10}	1.00×10^2	2.068	1.031	1.97×10^{-7}	3.36×10^{-3}	1.229	$Q2D$

Table 3.3: Integral characteristics and type of the computed base flow states.

Q2D are used in this chapter to describe the general flow transformation caused by the magnetic field, i.e. suppression of velocity and temperature gradients along the magnetic field lines in the core of the duct and formation of thin Hartmann boundary layers. The base flow, in which streamwise uniformity is also imposed, becomes, respectively, 2D and Q1D.

The Q2D regime is found in the larger part of the explored range of Ha and Gr including the most interesting cases of large Ha (see the rightmost column in table 3.3). The total friction force increases at stronger magnetic fields. The visible effect of convection is the asymmetry of the velocity profile, with U_x larger in the bottom than in the top half (see, e.g., figure 3.4b, d). The cause of the asymmetry has been explained in section 3.2.1.

The 3D regimes are only found in a limited range of moderate values of Ha at $Gr = 10^9$ and 10^{10} (see table 3.3). The transverse circulation consist of a single roll (see figure 3.3b, e) or two symmetric rolls (see figure 3.3c, d). The single roll has no preferred circulation direction and may appear in the solution either as shown in the figure 3.3b or as a symmetric reflection with respect to the vertical midplane (see figure 3.3e for an example). The circulation causes a visibly 2D distributions of Θ and U_x, and, at the same values of Gr, a decrease of E_θ as a result of mixing (see table 3.3). Stronger top–bottom asymmetries or even formation of reverse flow in the top portion of the duct as the strength of convection increases at fixed Ha is observed (see figure 3.3$a - c$ for an example). As an illustration of the asymmetry the minimum (all the regimes with zero values of the streamwise velocity except one at $Ha = 10000$, $Gr = 10^{10}$ where $u_{x,min} = -0.402$) and maximum values of u_x are shown in table 3.3.

The classification of the flow regimes into Q2D and 3D can also be described in terms of the values of the average kinetic energy of transverse circulation E_t. DNS data shown in table 3.3 and figure 3.5 are in a good qualitative agreement with the results of [17]. The observed differences can be attributed to the substantially different studied ranges of Ha and Gr and different aspect ratio.

One can see in figure 3.5 that, at a fixed Reynolds number considered in this work, the intensity of the transverse circulation is well approximated by a function of the single control parameter - the combination Gr/Ha^2. Analyzing the flow structures at various values of E_t a clear demarcation is found between 3D and Q2D regimes. E_t is greater than, approximately, 10^{-4} in 3D regimes. Q2D flows all have values of E_t less than 10^{-6}.

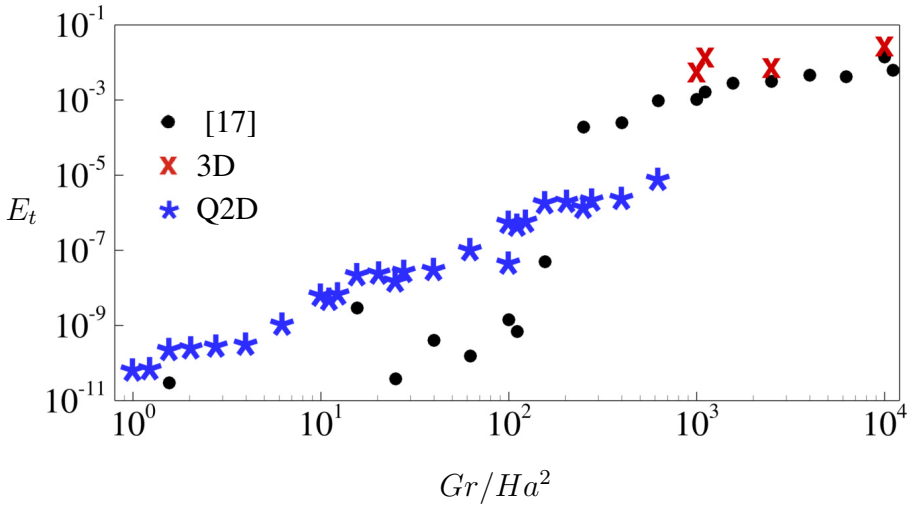

Figure 3.5: The average kinetic energy of transverse circulation in the base flow E_t as a function of Gr/Ha^2. Circles indicate the numerical results of [17] at $\Gamma = 1.0$. Stars and crosses indicate, respectively, Q2D and 3D regimes found in this work for the flow at $\Gamma = 3.5$. Values of E_t and Gr/Ha^2 for each computed flow can be found in table 3.3.

The interest in this study is primarily in the Q2D regimes. The 3D regimes are not considered in the rest of the chapter.

3.3.2 Applicability of the SM82 Model

In this section, the applicability of the SM82 model to analysis of magnetoconvection instability is investigated.

3.3.2.1 Base flow

For a streamwise-uniform, unidirectional, steady-state base flow, the SM82 model equations (3.15)−(3.17) are reduced to a system of linear ordinary differential equations. The solution satisfying the boundary conditions is:

$$U_x(z) = \frac{Re}{Ha}\left(Cc_1 + \frac{A}{\Gamma}s_1 - Az - C\right), \tag{3.23}$$

$$\Theta(z) = \frac{Re}{2Ha^2}\left(C\Gamma c_1 + As_1\right) - \frac{Re}{Ha}\frac{\Gamma}{4}\left(\frac{A}{3}z^3 + Cz^2\right) + a_1 z, \tag{3.24}$$

where

$$a_1 = -\frac{Re}{Ha^{3/2}}\frac{\Gamma}{2}\left(Ct_1 + At_1^{-1}\right) + \frac{Re}{2Ha}\left(\frac{A}{2\Gamma} + C\right), \tag{3.25}$$

$$c_1 = \frac{cosh(\sqrt{Ha}z)}{cosh(\sqrt{Ha}/\Gamma)}, \quad s_1 = \frac{sinh(\sqrt{Ha}z)}{sinh(\sqrt{Ha}/\Gamma)}, \quad t_1 = tanh(\sqrt{Ha}/\Gamma), \tag{3.26}$$

$$A = \frac{\Gamma}{2RePr}\frac{Gr}{Re^2}, \quad C = \frac{Ha}{Re\Gamma}\frac{1}{t_1/\sqrt{Ha} - 1/\Gamma}. \tag{3.27}$$

The profiles (3.23) and (3.24) are shown for $Gr = 10^8, 10^9, 10^{10}$ and several values of Ha in figure 3.6. For comparison, solutions of the 3D equations U_x and Θ obtained for the computed base flow solutions described in section 3.3.1 are shown for the midplane $y = 0$.

Good agreement between the computed solutions and the solutions of the SM82 model is evident at $Gr = 10^8$ and 10^9. There are some deviations between the computed and model profiles of U_x, but they are small and decrease with increasing Ha. The agreement is significantly worse in the case of the flows at $Gr = 10^{10}$. Here, large deviations between the computed and model curves at $Ha = 5000$ and smaller, yet still significant deviations at $Ha = 10000$ are observed.

The main reason for the discrepancy between the results of 2D model and 3D calculations at such a high Ha is the geometry of the flow. The duct has a large aspect ratio Γ and the magnetic field oriented along the long side. Deviations from two-dimensionality become more pronounced in such geometries. To verify this explanation, additional simulations for various values of Ha and Gr are performed, which revealed that velocity and temperature profiles in 2D and 3D solutions are almost indistinguishable from each other at $\Gamma \leq 1$.

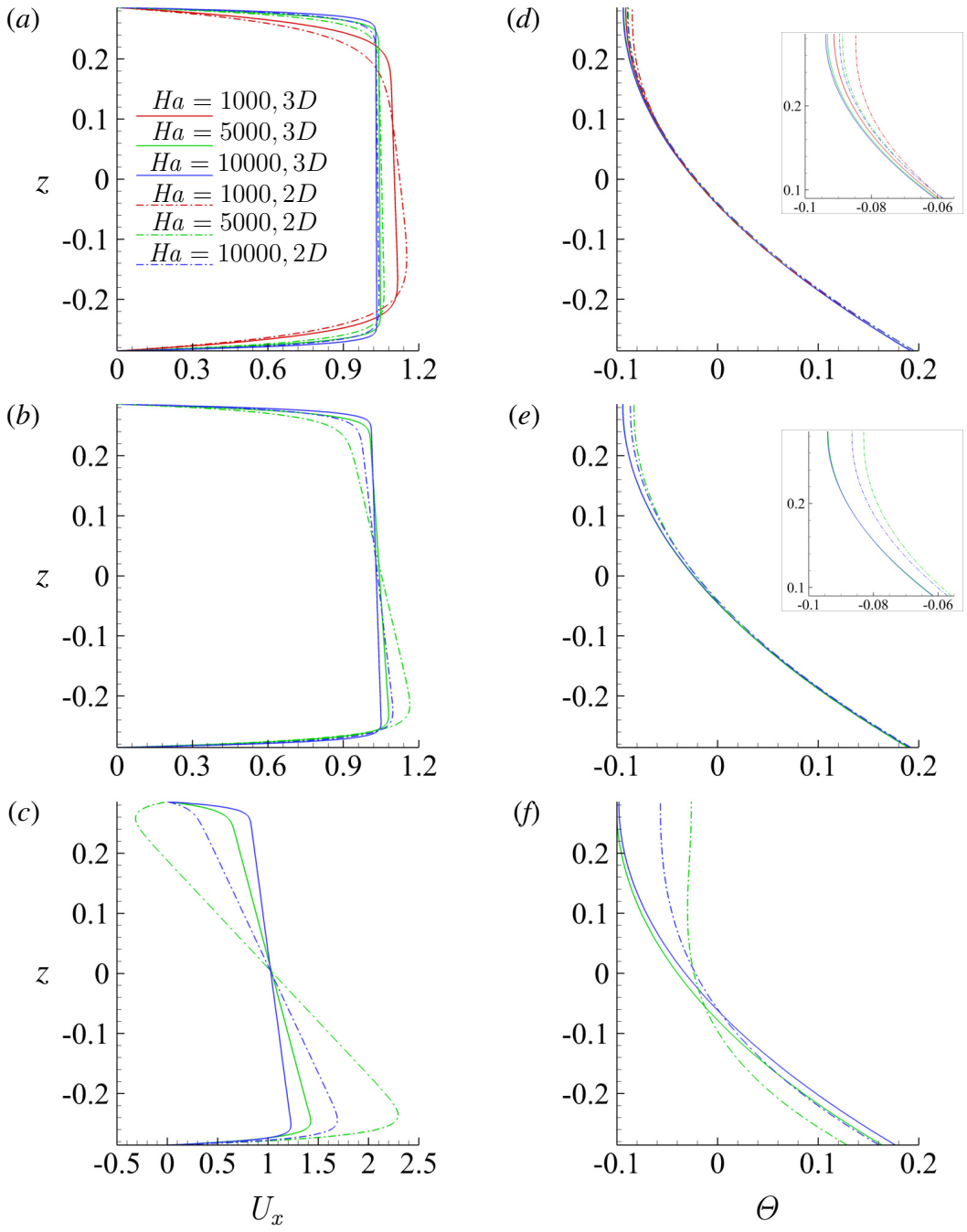

Figure 3.6: Base flow profiles at $Gr = 10^8$ (a, d), $Gr = 10^9$ (b, e), and $Gr = 10^{10}$ (c, f). The SM82 model solutions (3.23), (3.24) and the distributions along the midplane $y = 0$ obtained in the full numerical solutions of section 3.3.1 are denoted, respectively, as 2D and 3D. The curves for $Ha = 10^3$ are only shown at $Gr = 10^8$ (a, d), since at higher Gr the base flow is not Q2D (see section 3.3.1). The top and bottom rows show the profiles of streamwise velocity and temperature, respectively. The insets in (d) and (e) show zoomed-in illustrations of the temperature profiles near the top wall.

3.3.2.2 Linear stability analysis

In order to verify applicability of the SM82 model to linear stability analysis of Q2D flows, instability of several high$-Ha$ flows was evaluated twice: once using full 3D model of the base flow and perturbations and once entirely in the framework of the 2D SM82 model. The results are presented in figure 3.7 and table 3.4. Good agreement between predictions of 2D and 3D models at $Gr = 10^8$ and 10^9 can be seen. The accuracy improves with growing Ha. As an example, the average relative difference between the values of the growth rate γ for the two models is 33% at $Ha = 2000$, $Gr = 10^9$, 11% at $Ha = 3000$, $Gr = 10^9$ and 3% at $Ha = 10000$, $Gr = 10^9$. The situation is less clear for flows at $Gr = 10^{10}$ (see figure 3.7c and the last six lines of table 3.4). Here only a qualitative agreement is achieved. The shape of the $\gamma(\lambda)$ curves, the wavelength of the most unstable mode, and the effect of Ha on stability are similar in the 3D and 2D solution. The quantitative agreement is, however, poor, with the difference between the values of γ found for the two models being about 60% at $Ha = 4000$. Discrepancy between the 3D and 2D solutions becomes smaller at higher values of Ha. For example, it is about 20% at $Ha = 10000$.

The quantitative disagreement between the base flow profiles and, as an evident consequence, stability properties found in the 3D and 2D models is difficult to interpret. The velocity and temperature distributions computed in the framework of the 3D model clearly show that the base flow is Q2D and nearly perfectly unidirectional at Ha higher than approximately 4000 (see figure 3.4b, d and values of E_t in table 3.3). As illustrated in section 3.3.3, fields of growing perturbations also remain Q2D at such high Ha. Additional calculations performed with larger grids and longer times of flow evolution did not lead to significant changes. The deviations from quasi-two-dimensionality and inaccuracy of the numerical model are, therefore, excluded as possible reasons.

A further useful, albeit not fully explaining illustration is provided in figure 3.8. Computed base flow distributions of U_x and the streamwise component of the Lorentz force F_{Lx} are shown for $Ha = 10000$ and $Gr = 10^8, 10^9$ and 10^{10} within and near the Hartmann

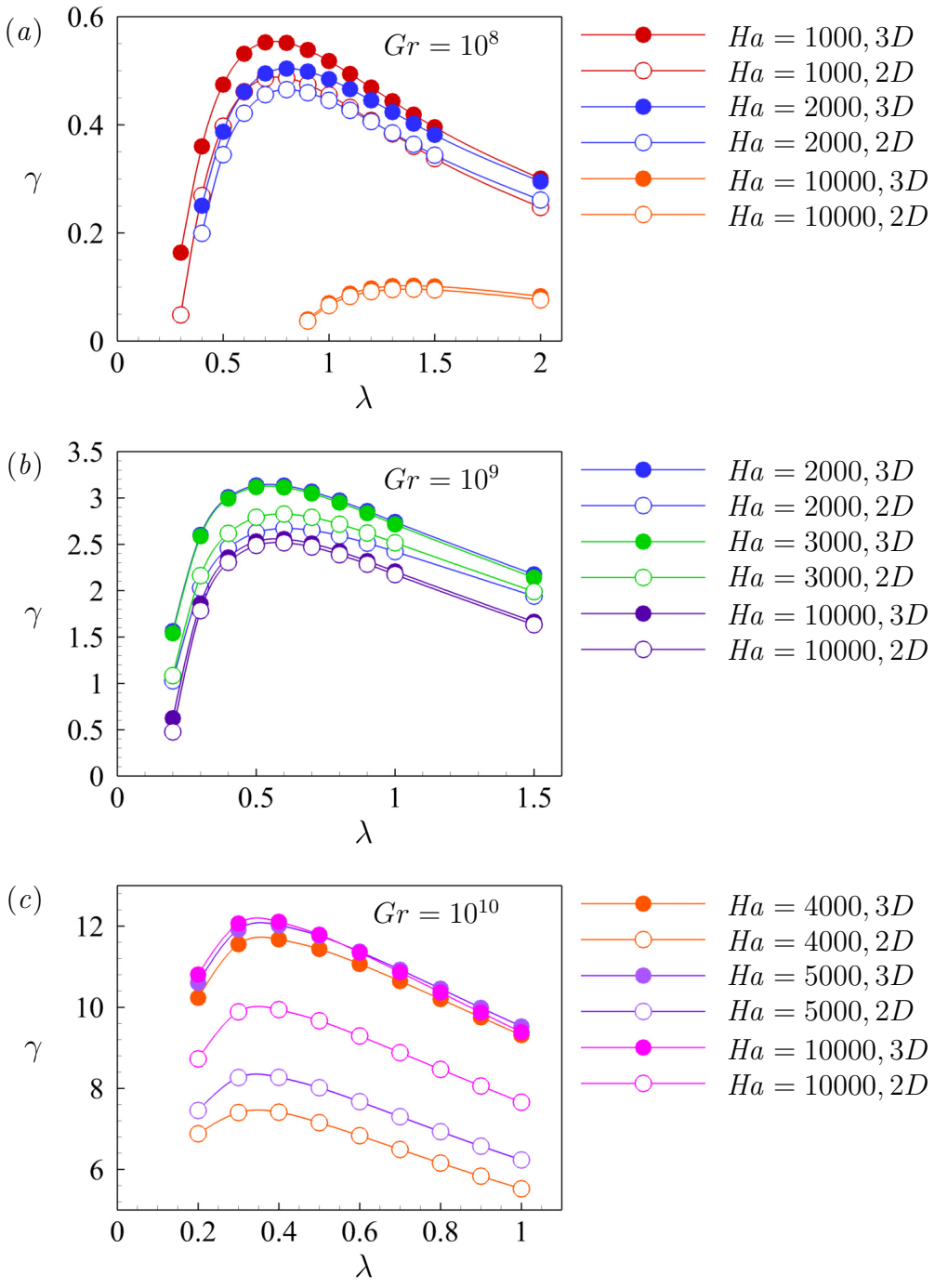

Figure 3.7: Rates of exponential growth γ shown as functions of the axial wavelength λ at $Ha = 1000, 2000, 10000$, $Gr = 10^8$ (a), $Ha = 2000$, 3000, 10000, $Gr = 10^9$ (b), and $Ha = 4000, 5000, 10000$, $Gr = 10^{10}$ (c). The results of 3D and 2D (SM82) models are denoted as filled and empty circles, respectively.

boundary layer. It can be seen that the strong vertical variation of U_x existing at $Gr = 10^{10}$ extends toward the Hartmann wall and causes a respective variation of the Lorentz force. It

Ha	Gr	λ										
		0.2	0.3	0.4	0.5	0.6	0.7	0.8	0.9	1.0	1.5	2.0
1000	10^8	–	0.164	0.360	0.474	0.532	0.553	0.552	0.538	0.518	0.396	0.301
1000	10^8	–	0.049	0.269	0.398	0.461	0.486	0.487	0.475	0.455	0.338	0.247
2000	10^8	–	–	0.251	0.387	0.461	0.495	0.504	0.499	0.485	0.381	0.295
2000	10^8	–	–	0.200	0.345	0.486	0.422	0.456	0.459	0.445	0.344	0.261
2000	10^9	1.563	2.602	3.010	3.136	3.134	3.069	2.972	2.859	2.741	2.175	–
2000	10^9	1.028	2.029	2.459	2.626	2.671	2.651	2.593	2.513	2.421	1.941	–
3000	10^9	1.540	2.587	2.993	3.117	3.114	3.048	2.950	2.836	2.715	2.141	–
3000	10^9	1.085	2.162	2.619	2.791	2.827	2.792	2.717	2.622	2.516	1.990	–
4000	10^{10}	10.234	11.553	11.674	11.435	11.067	10.645	10.202	9.754	9.312	–	–
4000	10^{10}	6.881	7.404	7.415	7.156	6.833	6.494	6.158	5.834	5.525	–	–
5000	10^{10}	10.605	11.918	12.023	11.764	11.371	10.925	10.458	9.988	9.527	–	–
5000	10^{10}	7.454	8.269	8.273	8.018	7.673	7.303	6.934	6.577	6.237	–	–
10000	10^{10}	10.807	12.064	12.106	11.791	11.351	10.865	10.366	9.871	9.389	–	–
10000	10^{10}	8.729	9.890	9.942	9.668	9.291	8.882	8.468	8.059	7.661	–	–

Table 3.4: Results of the linear stability analysis of 3D and 2D flow solutions. Rates of exponential growth γ are shown as functions of the axial wavelength λ. The results of the SM82 model are underlined. The growth rates are determined as in (3.18).

must be noted that this picture does not contradict to the identification of the flow as Q2D. The profiles $U_x(y, z = const)$, if taken outside the sidewall layers at the horizontal walls and scaled by the respective maximum values of U_x, collapse into one curve with a flat core and Hartmann boundary layers.

3.3.2.3 Nonlinear flows

The results presented so far in this section indicate that the SM82 2D model may also inaccurately describe the nonlinear flow regimes developing as a result of the instability at $Gr = 10^{10}$. As a test of this possibility, comparison between the results of 2D and 3D models at $Gr = 10^{10}$, $Ha = 10000$ is illustrated in figures 3.9, 3.10 and 3.11 and discussed below. The procedure of computing nonlinear flows is described in section 3.3.4. It needs to be mentioned that the same numerical resolution is used in 2D and 3D models. The shorter wavelength domain length $L_x = 2\pi$ is used in the 3D model. This rather small length has no significant effect on the flow evolution as it has been confirmed in the additional 2D

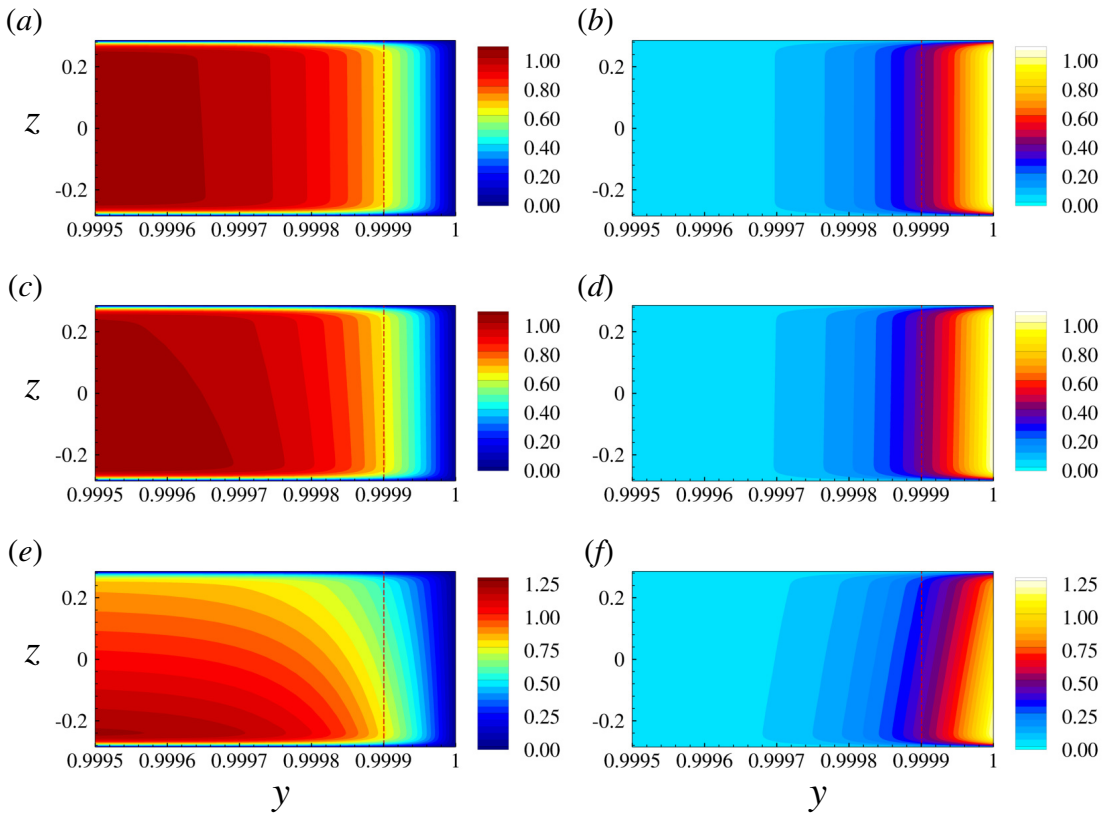

Figure 3.8: Base flow at $Gr = 10^8$ (a, b), $Gr = 10^9$ (c, d), and $Gr = 10^{10}$ (e, f) for $Ha = 10000$. The left and right columns show, respectively, distributions of streamwise velocity U_x and the streamwise component of the Lorentz force F_{Lx} near the Hartmann wall. The red dashed line shows the boundary of the Hartmann layer of thickness $\delta_{Ha} = Ha^{-1}$.

simulations conducted with $L_x = 4\pi$ (shown in figure 3.9) and $L_x = 2\pi$.

The simulations show that the 3D flow remains Q2D at these values of Ha and Gr. At the same time, its reproduction by the 2D SM82 model is inaccurate in some aspects. The instantaneous distributions of velocity components and temperature shown in figure 3.9 clearly illustrate the difference. 2D approximations (see figure 3.9a-c) are similar to 3D flows (see figure 3.9d-f) in terms of the largest typical streamwise wavelength (about 1.5) but demonstrate noticeably less regular pattern and higher energy in shorter wavelengths. The difference is reflected by the point signals of velocity and temperature shown in figure 3.11. It is also observed in the power spectrum density graphs of velocity and temperature (not shown). Comparing figures 3.11b and 3.11d, it can be seen that the 2D approximation

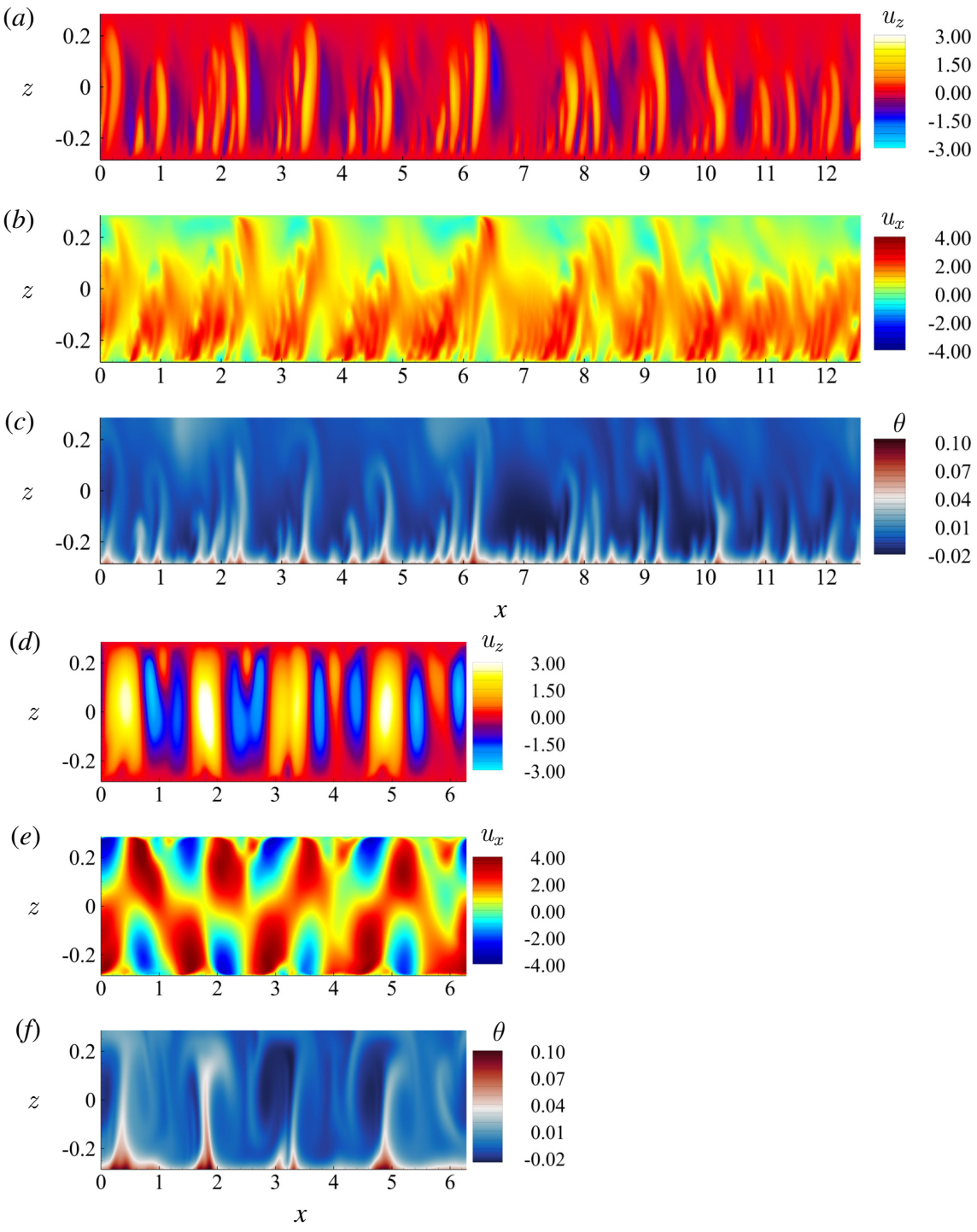

Figure 3.9: Flow structure in nonlinear regime at $Gr = 10^{10}$, $Ha = 10000$. The instantaneous distributions of u_z (a, d), u_x (b, e), and θ (c, f) obtained in 2D and 3D (plotted in the midplane $y = 0$) models are shown in (a)-(c) and (d)-(f), respectively.

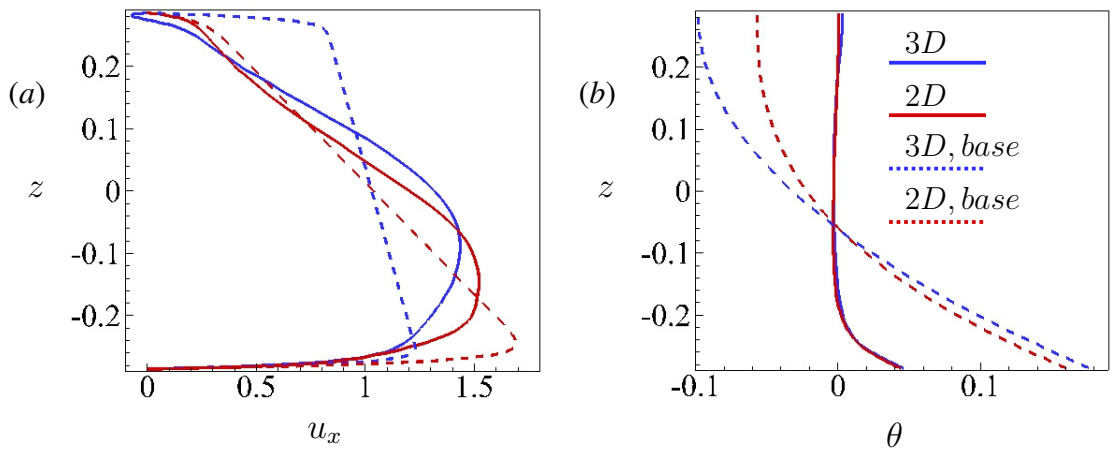

Figure 3.10: The profiles of u_x and θ in nonlinear regime at $Gr = 10^{10}$, $Ha = 10000$ obtained by averaging over x and time (with the base flow profiles from figure 3.6c, f) are shown, respectively, in (a) and (b).

substantially underestimates the typical amplitude of velocity fluctuations. As an example, the standard deviation for the signal of u_x in the middle of the duct ($z = 0$) is 0.33 for the 2D model and 0.71 for the 3D model. Computed values of volume-average kinetic energy of the fluctuations (not shown) confirm this conclusion. The values of energy found in the 2D approximation are about an order of magnitude lower than in the actual flow computed in the framework of the 3D model.

Interestingly, the misrepresentation of the structure of velocity and temperature fluctuations by the 2D model does not lead to a similarly strong inaccuracy in the prediction of the effect of mixing by fluctuations. Profiles of average streamwise velocity and temperature in figures 3.9(g, h) show strong change in comparison with the base flow, but only moderate differences between the 2D and 3D results.

3.3.2.4 Applicability of the SM82 model: summary

It must be stressed that the proposed 2D model works perfectly well for the classical Hartmann duct flow [11]. Based on the results of our study, it is concluded that the SM82 approximation accurately represents Q2D flows at moderately large Gr (10^8 and 10^9 in our system). The accuracy deteriorates at higher Gr even though the flow remains Q2D.

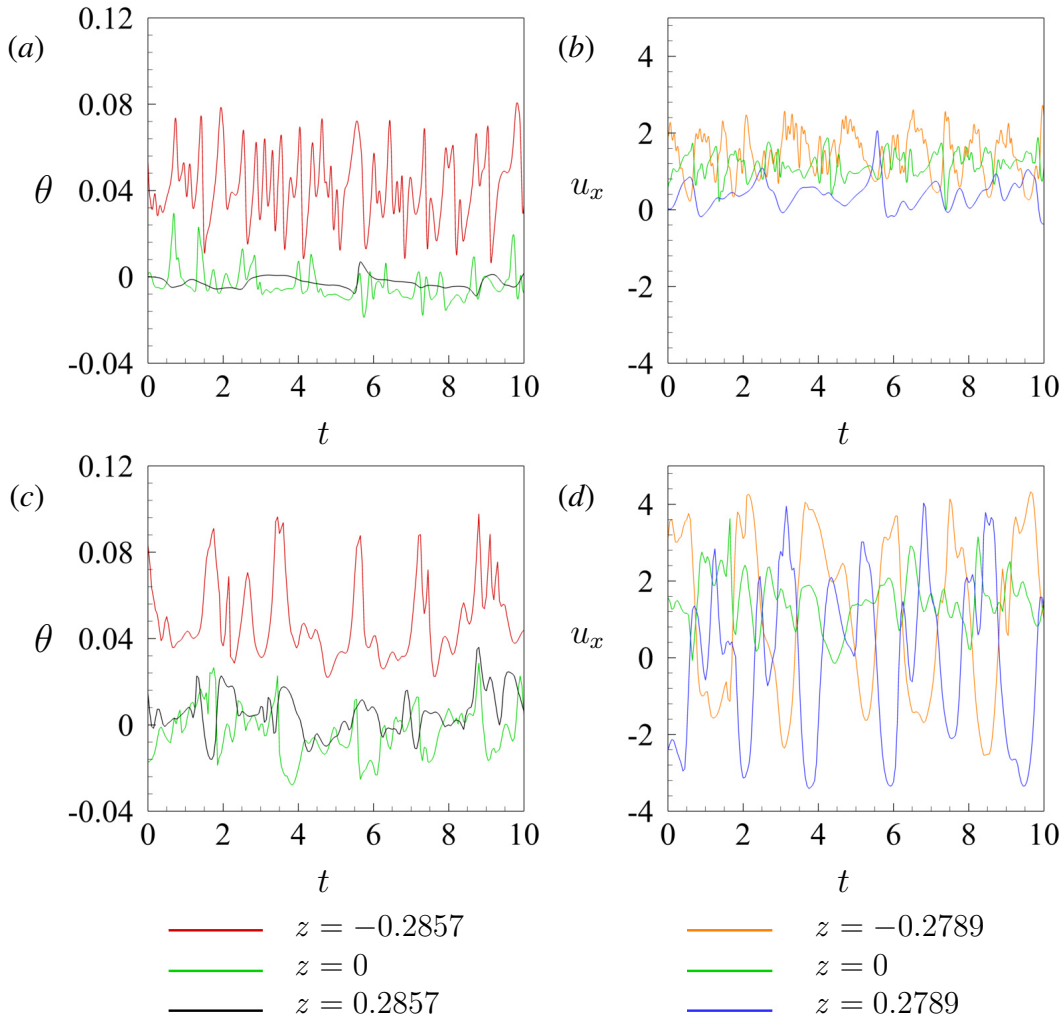

Figure 3.11: Time signals of temperature (a, c) and streamwise velocity (b, d) at $y = 0$ (in the 3D flow) in the nonlinear regime at $Ha = 10^4$, $Gr = 10^{10}$ are shown for 2D (a, b) and 3D (c, d) models.

An example of this is observed at $Ha \gtrsim 4000$ and $Gr = 10^{10}$. The base flow profiles are clearly different between the 2D and 3D models (see figures 3.6c, f). The 2D linear stability analysis is qualitatively correct in the sense that it correctly predicts the principal type of the unstable perturbations and the streamwise wavelength of the most unstable mode (see figure 3.7c). The values of the growth rate γ are, however, substantially underestimated by the 2D model (see figure 3.7c and table 3.4). The nonlinear flow states resulting from the instability are predicted incorrectly by the 2D model, which adds artificial irregularity and short-wave fluctuations and underestimates the amplitude of velocity fluctuations (see

figures 3.9 and 3.11). It should be noted that the discrepancy is not due to irregularities of the model or our computational procedure. Calculations carried out at lower Gr and high Ha reveal a perfectly good agreement in the bulk region between the 2D and 3D models.

It should be mentioned that the quality of the 2D approximation improves with increasing Ha. As an example, the values of the linear instability growth rate γ shown in table 3.4 are underpredicted by the 2D model by about 60% at $Ha = 4000$ and by about only 20% at $Ha = 10000$. A further explanation to this effect is left for future studies. One reason for discrepancy is the geometry of flow. The 2D model tends to be less accurate if applied to flows in ducts with larger aspect ratios and the magnetic field parallel to the long side. This conclusion is important as a warning against application of the model without a proper verification.

It must be mentioned that this is not the only example of the model's breakdown. The model is known to break down when any 3D structures are present in the flow for which the typical streamwise length scale is shorter than the size of the domain [76, 77].

Based on the findings in this section, the SM82 model can be safely applied to all the Q2D flow regimes at $Gr = 10^8$ and 10^9. At $Gr = 10^{10}$, it is recommended to use the full 3D solutions for the Hartmann numbers considered in the study. Therefore, in the remaining part of this chapter, the discussion of the instability and nonlinear states is based on the SM82 2D approximation for flows at $Gr = 10^8$ and 10^9 and on the full 3D solutions for flows at 10^{10}.

The numerical solution for the 2D approximation is obtained using a modified version of the code which solves (3.15)$-$(3.17). The code has been verified through comparison of its results with the analytical solution of (3.23)$-$(3.27) for the base flow.

3.3.3 Results of Linear Stability Analysis

The results of the linear stability analysis are summarized in figures 3.12$-$3.14 and table 3.5. It needs to be mentioned that the wavelength λ is varied with step 0.1 in the

Gr	Ha	λ_{max}	γ_{max}	Gr	Ha	λ_{max}	γ_{max}	Gr	Ha	λ_{max}	γ_{max}
10^8	1000	0.8	0.487	10^9	1000	–	–	10^{10}	1000	–	–
10^8	2000	0.8	0.465	10^9	2000	0.6	2.671	10^{10}	2000	–	–
10^8	3000	0.9	0.400	10^9	3000	0.6	2.827	10^{10}	3000	–	–
10^8	4000	0.9	0.336	10^9	4000	0.6	2.856	10^{10}	4000	0.4	11.674
10^8	5000	1.0	0.277	10^9	5000	0.6	2.833	10^{10}	5000	0.4	12.023
10^8	6000	1.1	0.226	10^9	6000	0.6	2.786	10^{10}	6000	0.4	12.094
10^8	7000	1.1	0.184	10^9	7000	0.6	2.726	10^{10}	7000	0.4	12.112
10^8	8000	1.2	0.149	10^9	8000	0.6	2.659	10^{10}	8000	0.4	12.106
10^8	9000	1.3	0.120	10^9	9000	0.6	2.589	10^{10}	9000	0.4	12.161
10^8	10000	1.4	0.096	10^9	10000	0.6	2.517	10^{10}	10000	0.4	12.106

Table 3.5: Results of linear stability analysis. Wavelengths λ_{max} and exponential growth rates γ_{max} of the fastest growing modes are shown as functions of Ha and Gr. Only the data for flow regimes identified as Q2D in the analysis of the base flow are shown.

simulations. The computed values of the exponential growth rate γ as a function of the wavelength λ for various combinations of Ha and Gr are shown in figure 3.12. Two trends of the linear stability behavior were proposed in [17]: (1) a higher growth rate and shorter wavelength appear at higher Gr; (2) an increase of Ha leads to a higher growth rate. The second, apparently counterintuitive effect was attributed to modification of the base flow, namely to suppression of the transverse circulation resulting in weaker mixing and stronger unstable temperature stratification [17].

In order to investigate these trends for our system and parameter range, the exponential growth rate γ_{max} of the fastest growing modes and the corresponding wavelengths λ_{max} are presented in figure 3.13 and table 3.5. The results are clearly consistent with the first trend, γ_{max} increases and λ_{max} decreases with growing Gr. However, a different behavior in regard of the second trend is found. The increase of Ha leads to noticeable or slight decrease of the exponential growth rates at $Gr = 10^8$ or $Gr = 10^9$, respectively (see figure 3.12c). For $Gr = 10^{10}$, γ is nearly insensitive to the values of Ha.

We conclude that the counterintuitive behavior of stronger instability at higher Ha is not observed in Q2D flows at high Ha considered in our study. It is, nevertheless, noteworthy that γ_{max} does not decrease with Ha at $Gr = 10^{10}$. It increases slightly at $Ha \lesssim 6000$ and

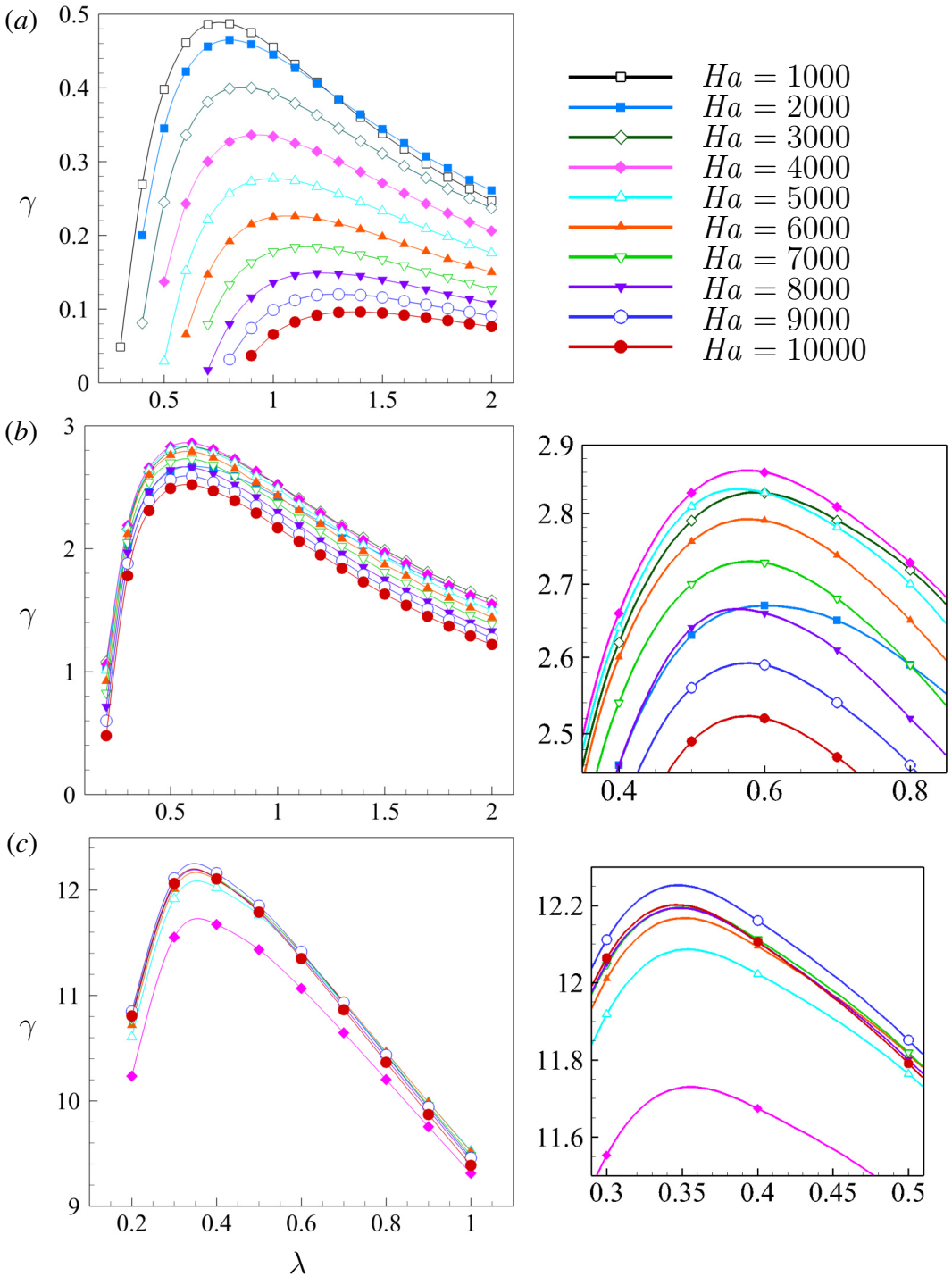

Figure 3.12: Rates of exponential growth γ shown as functions of axial wavelength λ at $Gr = 10^8$ (a), $Gr = 10^9$ (b), and $Gr = 10^{10}$ (c) for various values of Ha. Results of 2D SM82 approximation are shown for $Gr = 10^8$ and 10^9. Results of 3D computational analysis are shown for $Gr = 10^{10}$. Additional plots in (b) and (c) show zoomed-in areas around $(\lambda_{max}, \gamma_{max})$.

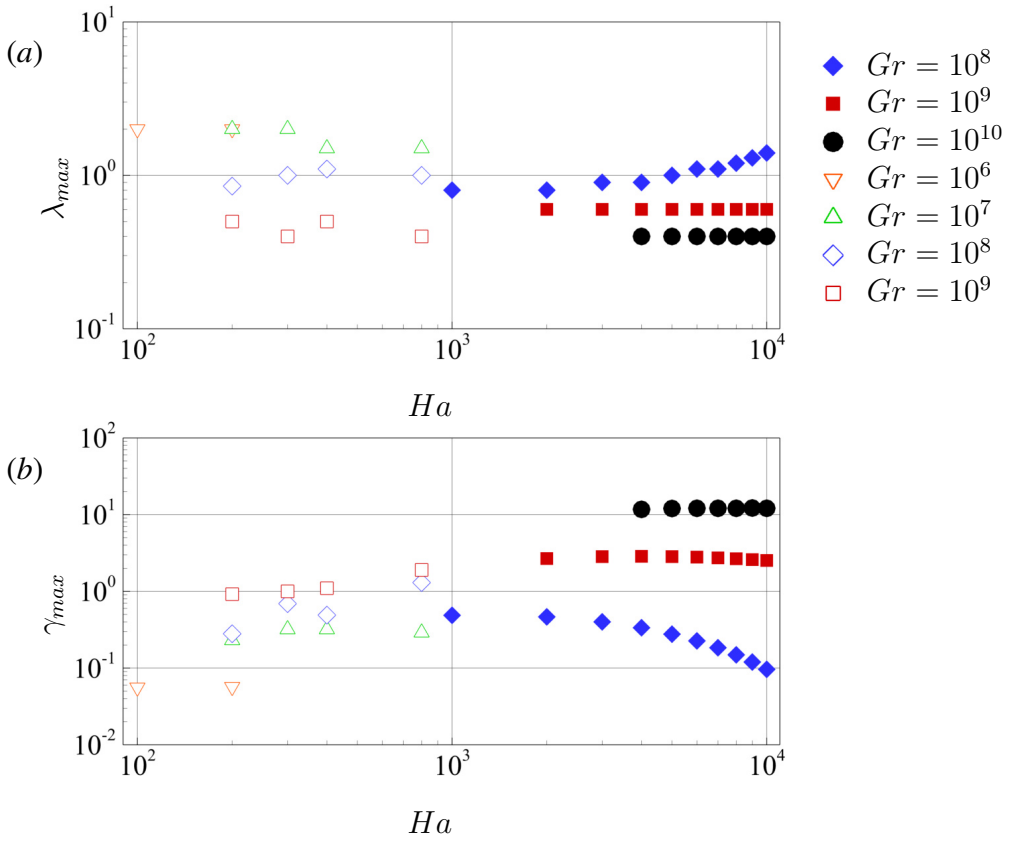

Figure 3.13: The wavelength λ_{max} (a) and the exponential growth rate γ_{max} (b) of the fastest growing perturbations as a function of Ha. The data are taken from table 3.5. The results of the current work and that of [17] are denoted as filled and unfilled elements, respectively. Results of 2D SM82 approximation are shown for $Gr = 10^8$ and 10^9. Results of 3D computational analysis are shown for $Gr = 10^{10}$.

remains practically constant at higher Ha. The enhanced friction in the Hartmann boundary layers is compensated by another effect, the only plausible candidate for which is the strong modification of the streamwise velocity profile visible in figure 3.6c. U_x strongly grows with Ha in the bottom half of the duct, i.e., its part with the strongest unstable temperature gradient.

The most unstable mode is oscillatory. This was also observed in the earlier works [16,17]. Point signals of temperature and velocity oscillate in time with constant frequency. This is caused by the transport of the rolls by mean flow. The phase velocity as the ratio of the axial wavelength to the period of oscillations of a signal at a given point to illustrate this effect have been computed. It is found that, similarly to findings of [16] and [17], it

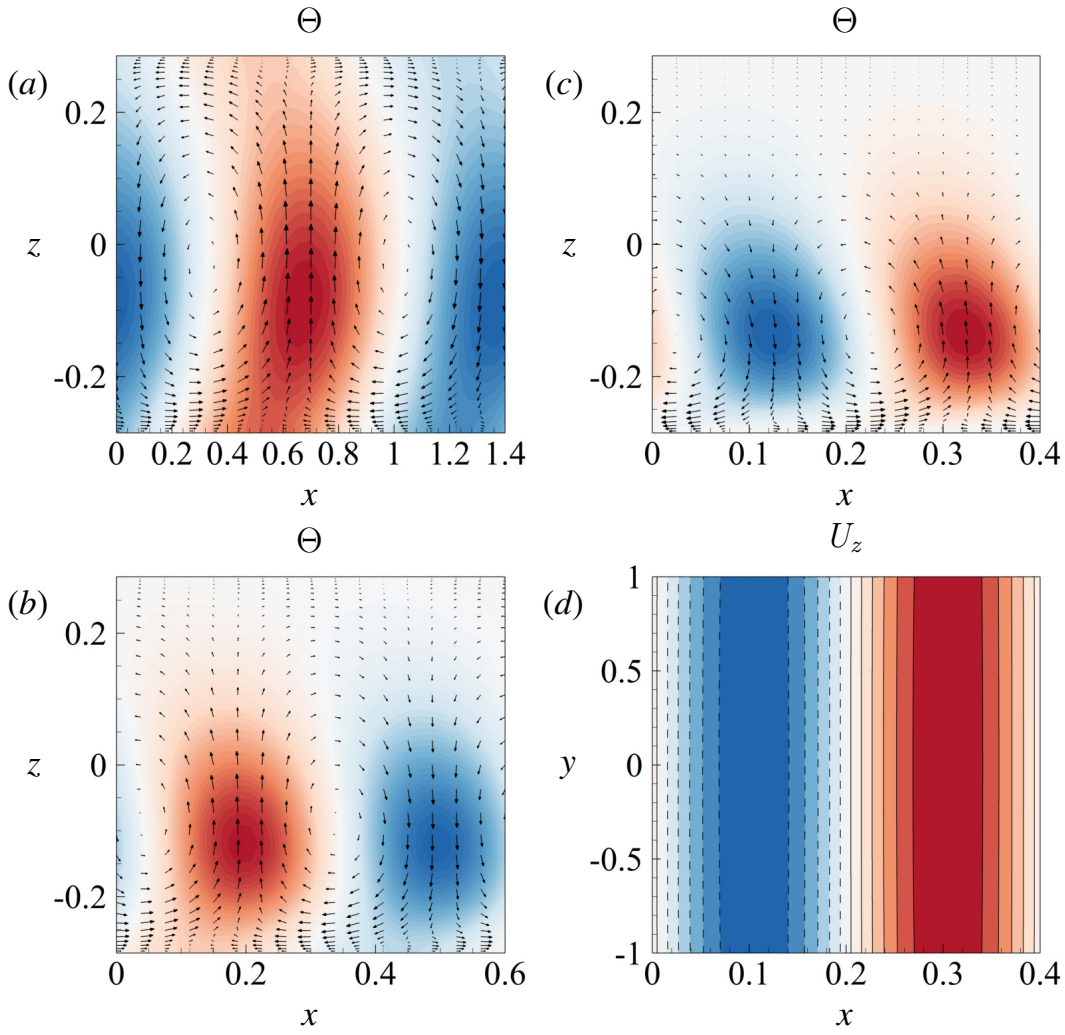

Figure 3.14: Spatial structure of the fastest growing instability modes during the stage of exponential growth at $Gr = 10^8$ (a), $Gr = 10^9$ (b), and $Gr = 10^{10}$ (c),(d) for $Ha = 10000$. Results of 2D SM82 approximation are shown for $Gr = 10^8$ and 10^9. Results of 3D computational analysis are shown for $Gr = 10^{10}$. Perturbations of temperature and vector fields of velocity perturbations (u', w') in the vertical midplane ($y = 0$) are shown in (a)-(c). Perturbations of vertical velocity in the horizontal midplane section $z = 0$ are shown in (d). Solid and dashed isolines indicate positive and negative values, respectively.

varies little with Ha and Gr for the most unstable modes, and has the value close to the mean velocity value 1.

The findings have critical implications for design and operation of the fusion reactor systems, since they indicate that strength of the convection instability is not diminished by strong magnetic fields at $Gr \geq 10^{10}$ typical for reactor blankets.

The spatial structure of the unstable modes is illustrated in figure 3.14 for $Gr = 10^8, 10^9, 10^{10}$ and $Ha = 10^4$. The structures are qualitatively similar to those found for Q2D instabilities in [17]. Consistent with the first trend mentioned above and with the base flow modification illustrated in figure 3.6 is the fact that the energy of growing perturbations becomes contained to the lower part of the duct at higher values of Gr.

3.3.4 Results of DNS of Nonlinear Flows

The results concerning the nonlinear flow regimes are illustrated in figures 3.9(d, e, f), 3.15, 3.16, and 3.18. DNS approach based on direct solution of the nonlinear governing equations is utilized. The 2D SM82 model (3.15)−(3.17) and the computational domain of length $L_x = 4\pi$ are used for flows at $Gr = 10^8$ and 10^9. Full 3D equations (3.1)−(3.3) are solved and the domain is reduced to $L_x = 2\pi$ at $Gr = 10^{10}$. Other parameters of computational model are described in section 3.2.4. Each simulation starts with the streamwise-independent base flow (see section 3.3.1) computed at the same Gr and Ha, to which random small-amplitude ($\sim 10^{-3}$) perturbations of velocity and temperature are added.

The typical flow evolution is illustrated by the curves of average kinetic energy shown in figure 3.15. The flow reaches a fully developed state after the instability and initial development. The evolution of the fully developed flow is computed for at least 500 time units for the 2D model at $Gr = 10^8, 10^9$ and at least 100 time units for the 3D model at $Gr = 10^{10}$. At this stage, the integral parameters fluctuate around steady means (at $Gr = 10^9$ and 10^{10}) or remain steady (at $Gr = 10^8$). The amplitudes of the fluctuations are small at $Gr = 10^9$ and large, but still moderate at $Gr = 10^{10}$.

Structure of fully developed flows is illustrated in figures 3.9 and 3.16. The velocity field shows finite-amplitude roll-like structures (hereafter referred to as rolls) resulting from the instability, which are superimposed on a streamwise-independent mean flow (see figures 3.9d and 3.16a, d). The rolls cause variations of temperature (see figures 3.9f, 3.16c and 3.16f). Transport of the rolls by the mean flow is a known reason of MCFs in

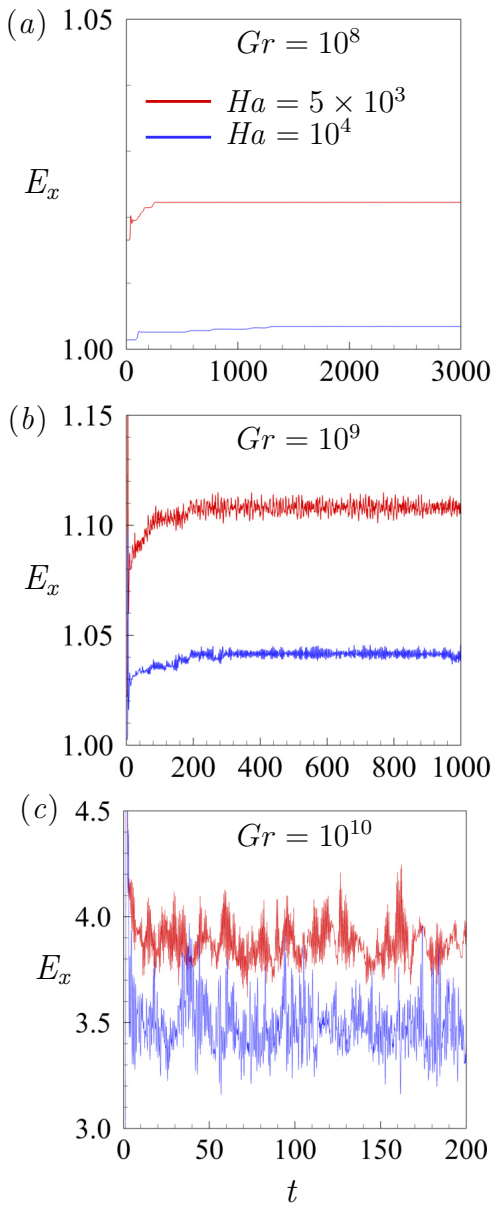

Figure 3.15: Time signals of the kinetic energy of the streamwise velocity obtained in the DNS of flows at $Gr = 10^8$ (a), $Gr = 10^9$ (b), and $Gr = 10^{10}$ (c) for $Ha = 5000$ and $Ha = 10000$. Results of 2D SM82 approximation are shown for $Gr = 10^8$ and 10^9. Results of 3D computational analysis are shown for $Gr = 10^{10}$.

horizontal channels [9, 16, 17].

Comparison of the flow structures in figures 3.9d-f and 3.16 reveal the effect of the value of Gr on convection rolls. As anticipated, increase of Gr leads to higher non-dimensional amplitude of the velocity fluctuations. This results in stronger vertical mixing

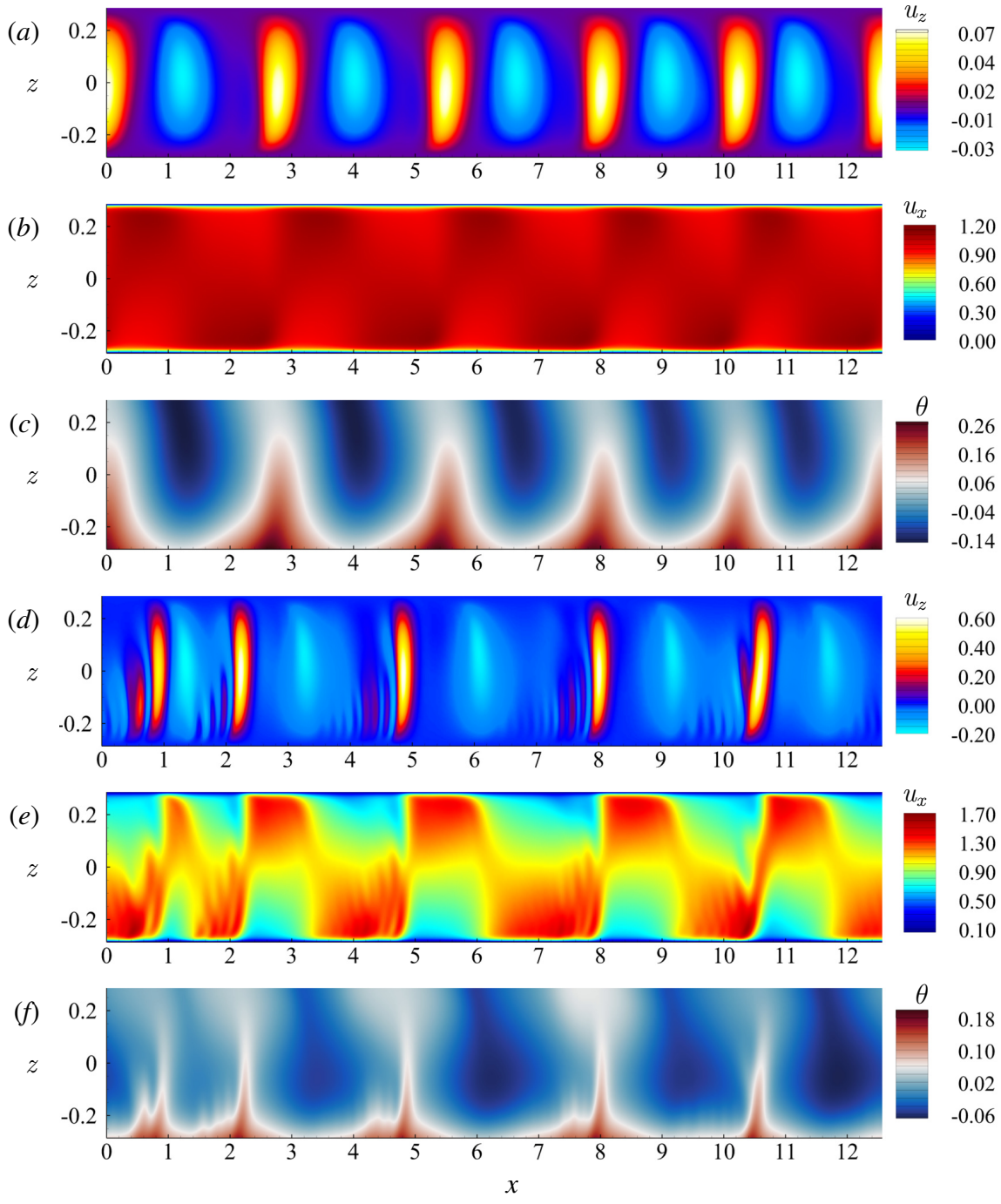

Figure 3.16: Flow structure in nonlinear regime at $Gr = 10^8$ (a-c) and $Gr = 10^9$ (d-f) for $Ha = 10000$. The instantaneous distributions of u_z (a, d), u_x (b, e), and θ (c, f) obtained in the 2D model are shown.

as illustrated by the streamwise- and time-averaged profiles in figure 3.17. In particular, a nearly uniform vertical distribution of average temperature with a thin (but still much

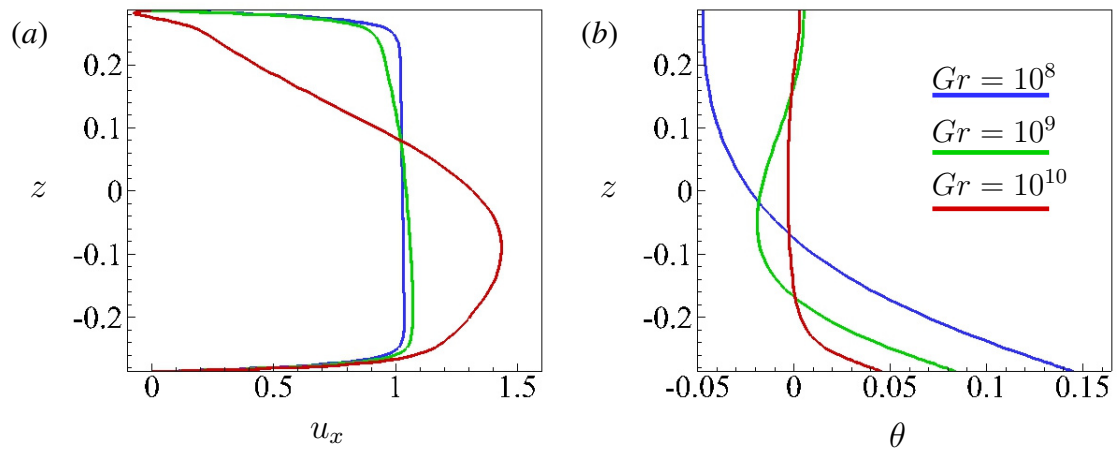

Figure 3.17: The profiles of u_x and θ in nonlinear regime for $Gr = 10^8, 10^9, 10^{10}$ at $Ha = 10000$ obtained by averaging over x and time are shown, respectively, in (a) and (b).

thicker than the Shercliff layer) boundary layer at the bottom is observed at $Gr = 10^{10}$.

As it was discussed earlier, MCFs caused by the instability have potentially critical implications for design and operation of liquid-metal components of nuclear fusion reactors. The DNS results allow us, for the first time, to evaluate the properties of the MCFs at the high values of Gr and Ha corresponding to the actual reactor conditions.

In addition to the instantaneous temperature distributions in figures $3.9f$, $3.16c$ and $3.16f$, the discussion will be based on the point-signals of temperature measured at the top and bottom walls and in the middle of the duct (see figure 3.18). As discussed, e.g., in [9], measuring such signals is the most reliable and commonly used tool for studying MCFs in experiments.

The evident conclusion from the DNS data is that MCFs are fully present in flows with $Gr = 10^8, 10^9, 10^{10}$ and the highest values $Ha = 5 \times 10^3$ and 10^4 considered in this study. The fluctuations are observed in the entire duct. The temperature signals are regular and dominated by one or several low frequencies (the typical period is 2-3 non-dimensional time units at $Gr = 10^8$ and 10^9). The signal is less regular and characterized by higher typical frequencies at $Gr = 10^{10}$.

Interestingly, the non-dimensional amplitude of the temperature fluctuations decreases

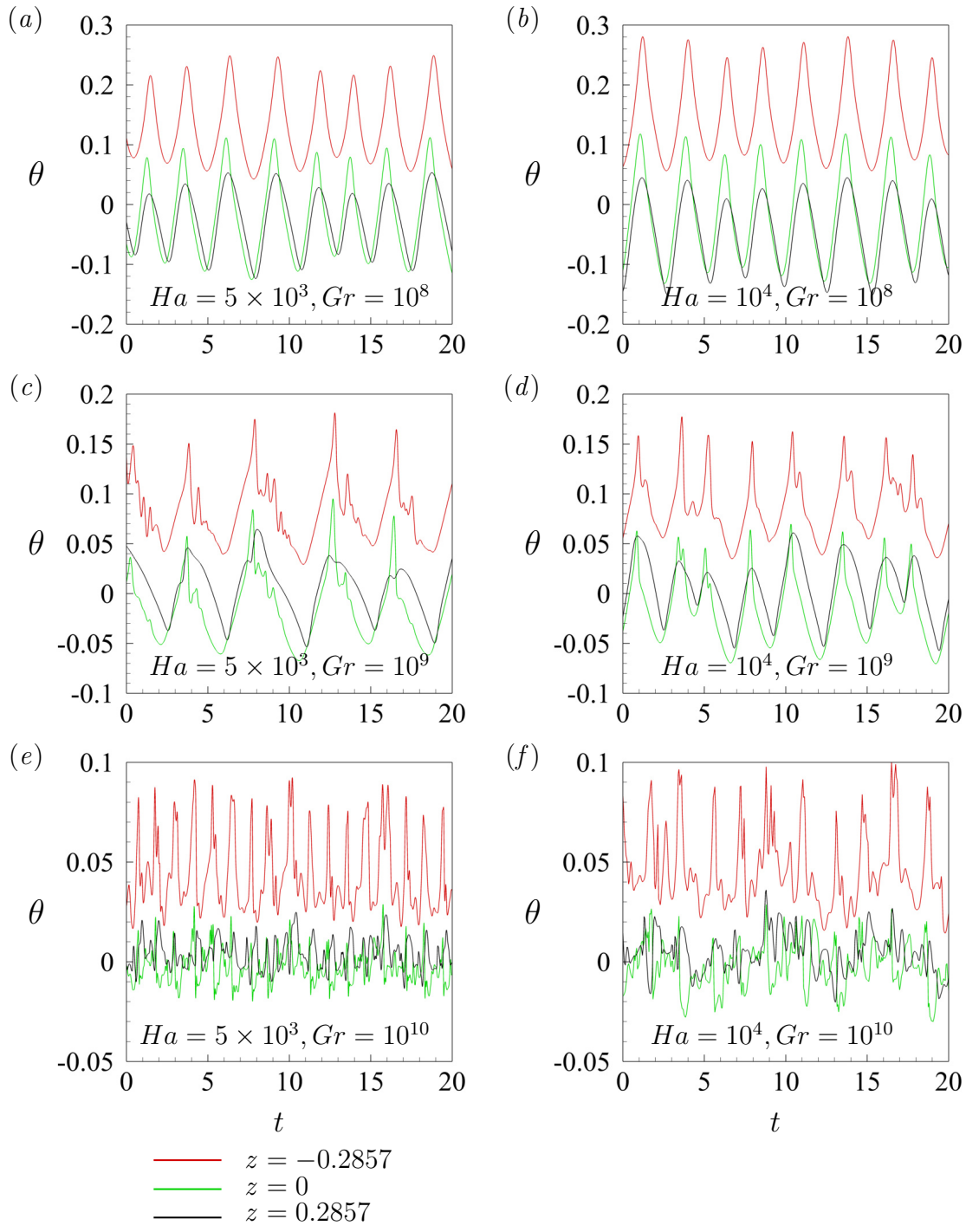

Figure 3.18: Time signals of temperature measured at top and bottom walls and in the middle of the duct in fully developed flows at $Gr = 10^8, 10^9, 10^{10}$ are shown for $Ha = 5 \times 10^3$ in (a, c, e) and for $Ha = 10^4$ in (b, d, f). Results of 2D SM82 approximation are shown for $Gr = 10^8$ and 10^9 $(a - d)$. Results of 3D computational analysis are shown for $Gr = 10^{10}$ $(e - f)$.

noticeably with growing Gr. Comparison of the signals in the two columns of figure 3.18 demonstrates that value of Ha has practically no effect on the MCFs. This can be attributed to the effect of nonlinearity, which distributes energy of the fluctuations to a range of streamwise modes.

Considering the practical implications, it is interesting to evaluate the parameters of the MCFs in dimensional units. We will do that for the temperature signals at the bottom of the duct ($z = -0.2857$) assuming the duct half-width $d = 5\ cm$ and using the physical properties of PbLi at $573\ K$ [9]. The wall heat rate is $q = 10.56\ kWm^{-2}$ at $Gr = 10^8$, $q = 105.6\ kWm^{-2}$ at $Gr = 10^9$ and $q = 1056\ kWm^{-2}$ at $Gr = 10^{10}$. We find, by applying the temperature scale qd/κ, that the largest amplitude of fluctuations of wall temperature is in the range $5 - 6\ K$ at $Gr = 10^8$, $44 - 62\ K$ at $Gr = 10^9$, and somewhat unrealistic $180-300\ K$ at $Gr = 10^{10}$. The typical time period of the fluctuations is 5.64 s at $Gr = 10^8$, $6.45\ s$ at $Gr = 10^9$, and $4.51\ s$ at $Gr = 10^{10}$ for $Ha = 10^4$.

Similar evaluations have been done for the future experiments on the recently built experimental facility (see, e.g., [66]), in which liquid mercury flows in the duct with the half-width of $d = 2.8\ cm$. The physical properties of Hg are taken at $303\ K$ [9]. The wall heat rate is $q = 9.59\ kWm^{-2}$ at $Gr = 10^8$ and $q = 95.9\ kWm^{-2}$ at $Gr = 10^9$. The results of nonlinear simulations allow us to predict the largest amplitude of fluctuations of temperature in the middle of the duct. The amplitudes are in the range of $2 - 3\ K$ at $Gr = 10^8$ and $12 - 18\ K$ at $Gr = 10^9$. The typical time period of the fluctuations is 1.1 s at $Gr = 10^8$ and 1.58 s at $Gr = 10^9$ for $Ha = 1000$.

3.3.5 Parametric Study

The results presented so far are for a single value of the Reynolds number $Re = 5000$. To explore the effect of Re on the MCFs, a parametric study is conducted at $Re = 4375, 8500, 17500$, $Gr = 10^8, 4.1 \times 10^8, 8.2 \times 10^8$ and $Ha = 175 - 1225$ with the aspect ratio $\Gamma = 3.5$. The parameter values are selected to match the values that are to

be investigated in the experimental facility (see, e.g., [66]) in the near future. The results of the study are presented in sections 3.3.5.1, 3.3.5.2 and 3.3.5.3. The interest in this study is primarily in the Q2D regimes, while the 3D regimes are only discussed in section 3.3.5.1.

3.3.5.1 Base flows

The results for all the completed simulations are summarized in tables 3.6, 3.7 and 3.8. The flow structure of the base flow in Q2D and 3D regimes has been shown and discussed in section 3.3.1. The structure for the newly explored regimes is similar (not shown, however, see for the reference figure 3.3).

The 3D regime is found in the larger part of the explored range of Re, Ha and Gr due to insufficient strength of the magnetic field to suppress convection circulation. For example, all the regimes at $Gr = 8.2 \times 10^8$ are 3D for any Re and Ha.

The classification of the flow regimes into Q2D and 3D in terms of the values of the average kinetic energy of transverse circulation E_t is extended to the new values of the non-dimensional parameters (see figure 3.19). The main conclusion is that the demarcation between 3D and Q2D regimes is valid for variable Re. It can also be more accurately determined. We can see that the flow regime is Q2D or 3D at, respectively, E_t smaller or greater than 10^{-5}.

3.3.5.2 Linear stability analysis

Linear stability was only done for Q2D regimes. The results of the linear stability analysis are summarized in table 3.9. The findings confirm two trends discussed in section 3.3.3 and extends them to the different values of Re.

The exponential growth rate γ_{max} of the fastest growing modes and the corresponding wavelengths λ_{max} decrease with growing Re at fixed Ha and Gr. For example, $\gamma_{max} = 0.569$ and $\lambda_{max} = 0.8$ at $Re = 4375$, while these values are 0.092 and 0.6, respectively, at $Re = 17500$ for $Ha = 1050$ and $Gr = 10^8$. The increase of Gr and/or Ha at fixed Re

Ha	Gr	Gr/Ha^2	$-d\hat{p}/dx$	E_x	E_t	E_θ	$u_{x,max}$	$Regime$
175	10^8	3.27×10^3	0.059	1.078	1.59×10^{-3}	2.52×10^{-3}	1.318	$3D$
175	4.1×10^8	1.34×10^4	0.065	1.069	8.68×10^{-3}	8.78×10^{-4}	1.344	$3D$
175	8.2×10^8	2.68×10^4	0.070	1.068	1.79×10^{-2}	5.71×10^{-4}	1.368	$3D$
350	10^8	8.16×10^2	0.096	1.072	3.70×10^{-4}	7.93×10^{-3}	1.207	$3D$
350	4.1×10^8	3.35×10^3	0.102	1.079	1.86×10^{-3}	2.34×10^{-3}	1.293	$3D$
350	8.2×10^8	6.69×10^3	0.107	1.101	4.39×10^{-3}	1.31×10^{-3}	1.464	$3D$
525	10^8	3.63×10^2	0.139	1.068	3.59×10^{-8}	3.57×10^{-3}	1.172	$Q2D$
525	4.1×10^8	1.49×10^3	0.142	1.071	4.54×10^{-4}	3.77×10^{-3}	1.208	$3D$
525	8.2×10^8	2.98×10^3	0.145	1.090	1.60×10^{-3}	2.47×10^{-3}	1.329	$3D$
700	10^8	2.04×10^2	0.181	1.059	2.41×10^{-8}	3.58×10^{-3}	1.147	$Q2D$
700	4.1×10^8	8.37×10^2	0.183	1.060	4.06×10^{-4}	7.45×10^{-3}	1.216	$3D$
700	8.2×10^8	1.67×10^3	0.185	1.074	5.81×10^{-4}	3.46×10^{-3}	1.323	$3D$
875	10^8	1.31×10^2	0.223	1.053	2.23×10^{-8}	3.58×10^{-3}	1.129	$Q2D$
875	4.1×10^8	5.36×10^2	0.225	1.054	3.74×10^{-7}	3.39×10^{-3}	1.192	$Q2D$
875	8.2×10^8	1.07×10^3	0.227	1.063	1.02×10^{-4}	3.53×10^{-3}	1.249	$3D$
1050	10^8	9.07×10^1	0.265	1.048	2.15×10^{-8}	3.58×10^{-3}	1.117	$Q2D$
1050	4.1×10^8	3.72×10^2	0.267	1.049	3.40×10^{-7}	3.40×10^{-3}	1.172	$Q2D$
1050	8.2×10^8	7.44×10^2	0.267	1.056	3.18×10^{-4}	7.30×10^{-3}	1.251	$3D$
1225	10^8	6.66×10^1	0.307	1.045	2.08×10^{-8}	3.59×10^{-3}	1.107	$Q2D$
1225	4.1×10^8	2.73×10^2	0.308	1.045	3.29×10^{-7}	3.41×10^{-3}	1.155	$Q2D$
1225	8.2×10^8	5.46×10^2	0.310	1.056	1.28×10^{-5}	3.22×10^{-3}	1.225	$3D$

Table 3.6: Integral characteristics and type of the computed base flow states at $Re = 4375$.

leads to increase of γ_{max}. For example, $\gamma_{max} = 0.569$ at $Gr = 10^8$, while it is 1.609 at $Gr = 4.1 \times 10^8$ for $Re = 4375$ and $Ha = 1050$.

The findings have critical implications for design and operation of the liquid metal blankets for fusion reactor systems. They indicate that strength of the convection instability is not diminished by strong magnetic fields, however, as new study shows, it decreases with growing Re, i.e., with growing flow rate in the ducts of a blanket module.

3.3.5.3 Nonlinear flows

DNS of the nonlinear flows was only conducted for Q2D regimes. The results of the nonlinear flow regimes are illustrated in figures 3.20, 3.21, 3.22 and 3.23.

Ha	Gr	Gr/Ha^2	$-d\hat{p}/dx$	E_x	E_t	E_θ	$u_{x,max}$	$Regime$
175	10^8	3.27×10^3	0.029	1.075	4.00×10^{-4}	2.53×10^{-3}	1.420	$3D$
175	4.1×10^8	1.34×10^4	0.032	1.062	2.20×10^{-3}	8.88×10^{-4}	1.407	$3D$
175	8.2×10^8	2.68×10^4	0.033	1.060	5.49×10^{-2}	6.06×10^{-4}	1.236	$3D$
350	10^8	8.16×10^2	0.049	1.071	9.39×10^{-4}	8.04×10^{-3}	1.345	$3D$
350	4.1×10^8	3.35×10^3	0.051	1.066	4.78×10^{-4}	2.40×10^{-3}	1.340	$3D$
350	8.2×10^8	6.69×10^3	0.052	1.060	1.14×10^{-3}	1.35×10^{-3}	1.335	$3D$
525	10^8	3.63×10^2	0.069	1.068	5.94×10^{-9}	3.62×10^{-3}	1.335	$Q2D$
525	4.1×10^8	1.49×10^3	0.071	1.064	1.20×10^{-4}	3.90×10^{-3}	1.288	$3D$
525	8.2×10^8	2.98×10^3	0.072	1.062	4.21×10^{-4}	2.57×10^{-3}	1.285	$3D$
700	10^8	2.04×10^2	0.090	1.059	3.02×10^{-9}	3.62×10^{-3}	1.251	$Q2D$
700	4.1×10^8	8.37×10^2	0.091	1.055	1.06×10^{-4}	7.74×10^{-3}	1.147	$3D$
700	8.2×10^8	1.67×10^3	0.092	1.056	1.58×10^{-4}	3.64×10^{-3}	1.245	$3D$
875	10^8	1.31×10^2	0.112	1.053	2.63×10^{-9}	3.61×10^{-3}	1.217	$Q2D$
875	4.1×10^8	5.36×10^2	0.112	1.051	5.03×10^{-5}	9.24×10^{-3}	1.131	$3D$
875	8.2×10^8	1.07×10^3	0.113	1.050	3.85×10^{-5}	3.87×10^{-3}	1.212	$3D$
1050	10^8	9.07×10^1	0.133	1.049	2.49×10^{-9}	3.61×10^{-3}	1.189	$Q2D$
1050	4.1×10^8	3.72×10^2	0.133	1.047	4.15×10^{-8}	3.51×10^{-3}	1.187	$Q2D$
1050	8.2×10^8	7.44×10^2	0.133	1.046	8.73×10^{-5}	7.87×10^{-3}	1.129	$3D$
1225	10^8	6.66×10^1	0.154	1.045	2.40×10^{-9}	3.61×10^{-3}	1.166	$Q2D$
1225	4.1×10^8	2.73×10^2	0.154	1.044	3.94×10^{-8}	3.51×10^{-3}	1.164	$Q2D$
1225	8.2×10^8	5.46×10^2	0.154	1.043	4.95×10^{-5}	8.58×10^{-3}	1.120	$3D$

Table 3.7: Integral characteristics and type of the computed base flow states at $Re = 8750$.

Structure of fully developed flows is illustrated in figures 3.20 and 3.21. The prominent effects of growing Re and Gr on the flow structures are observed. As discussed earlier in section 3.3.4, increase of Gr at fixed Re leads to higher non-dimensional amplitudes of roll-like structures of the vertical velocity and streamwise velocity fluctuations (see, e.g., figures 3.20a and 3.21a). This results in stronger vertical mixing as illustrated by the streamwise- and time-averaged profiles of u_x and θ in figure 3.22. On the contrary, at higher Re when Ha and Gr are fixed, weaker vertical mixing and decrease in the amplitudes of u_z and u_x are observed. The instantaneous distributions of temperature are found to be very similar to each other for all the presented regimes (see, figures 3.20c, f and 3.21c, f).

As it was explained earlier, the roll-like structures of u_z cause variations of temperature.

Ha	Gr	Gr/Ha^2	$-d\hat{p}/dx$	E_x	E_t	E_θ	$u_{x,max}$	*Regime*
175	10^8	3.27×10^3	0.015	1.074	1.00×10^{-4}	2.54×10^{-3}	1.451	$3D$
175	4.1×10^8	1.34×10^4	0.016	1.060	5.52×10^{-4}	8.92×10^{-4}	1.449	$3D$
175	8.2×10^8	2.68×10^4	0.017	1.056	1.14×10^{-3}	5.84×10^{-4}	1.447	$3D$
350	10^8	8.16×10^2	0.024	1.071	2.37×10^{-5}	8.09×10^{-3}	1.395	$3D$
350	4.1×10^8	3.35×10^3	0.025	1.064	1.21×10^{-4}	2.42×10^{-3}	1.394	$3D$
350	8.2×10^8	6.69×10^3	0.026	1.056	2.88×10^{-4}	1.37×10^{-3}	1.392	$3D$
525	10^8	3.63×10^2	0.035	1.069	1.09×10^{-9}	3.64×10^{-3}	1.359	$Q2D$
525	4.1×10^8	1.49×10^3	0.035	1.065	3.10×10^{-5}	3.96×10^{-3}	1.358	$3D$
525	8.2×10^8	2.98×10^3	0.036	1.061	1.08×10^{-4}	2.62×10^{-3}	1.356	$3D$
700	10^8	2.04×10^2	0.045	1.060	3.65×10^{-10}	3.63×10^{-3}	1.327	$Q2D$
700	4.1×10^8	8.37×10^2	0.046	1.055	2.73×10^{-5}	7.92×10^{-3}	1.326	$3D$
700	8.2×10^8	1.67×10^3	0.046	1.056	4.12×10^{-5}	3.73×10^{-3}	1.325	$3D$
875	10^8	1.31×10^2	0.056	1.053	2.77×10^{-10}	3.63×10^{-3}	1.300	$Q2D$
875	4.1×10^8	5.36×10^2	0.056	1.051	1.32×10^{-5}	9.59×10^{-3}	1.299	$3D$
875	8.2×10^8	1.07×10^3	0.056	1.049	3.93×10^{-5}	6.67×10^{-3}	1.298	$3D$
1050	10^8	9.07×10^1	0.066	1.049	2.52×10^{-10}	3.63×10^{-3}	1.276	$Q2D$
1050	4.1×10^8	3.72×10^2	0.066	1.048	4.43×10^{-9}	3.57×10^{-3}	1.275	$Q2D$
1050	8.2×10^8	7.44×10^2	0.067	1.046	2.31×10^{-5}	8.24×10^{-3}	1.274	$3D$
1225	10^8	6.66×10^1	0.077	1.045	2.40×10^{-10}	3.63×10^{-3}	1.254	$Q2D$
1225	4.1×10^8	2.73×10^2	0.077	1.044	4.04×10^{-9}	3.57×10^{-3}	1.253	$Q2D$
1225	8.2×10^8	5.46×10^2	0.077	1.043	1.35×10^{-5}	9.19×10^{-3}	1.252	$3D$

Table 3.8: Integral characteristics and type of the computed base flow states at $Re = 17500$.

Gr	Ha	Re	λ_{max}	γ_{max}	Re	λ_{max}	γ_{max}	Re	λ_{max}	γ_{max}
10^8	525	4375	0.8	0.479	8750	0.7	0.183	17500	0.6	0.031
10^8	700	4375	0.8	0.531	8750	0.7	0.220	17500	0.6	0.065
10^8	875	4375	0.8	0.557	8750	0.7	0.239	17500	0.6	0.082
10^8	1050	4375	0.8	0.569	8750	0.7	0.248	17500	0.6	0.092
10^8	1225	4375	0.8	0.573	8750	0.7	0.252	17500	0.6	0.097
4.1×10^8	1050	4375	0.6	1.609	8750	0.6	0.900	17500	0.6	0.424
4.1×10^8	1225	4375	0.6	1.678	8750	0.6	0.914	17500	0.6	0.433

Table 3.9: Results of linear stability analysis for flow regimes identified as Q2D in the analysis of the base flow (see tables 3.6, 3.7, 3.8). Wavelengths λ_{max} and exponential growth rates γ_{max} of the fastest growing modes are shown as functions of Re, Ha and Gr.

In addition to the distributions, the point-signals of temperature and streamwise velocity measured at the top and bottom walls and in the middle of the duct (see figure 3.23). The

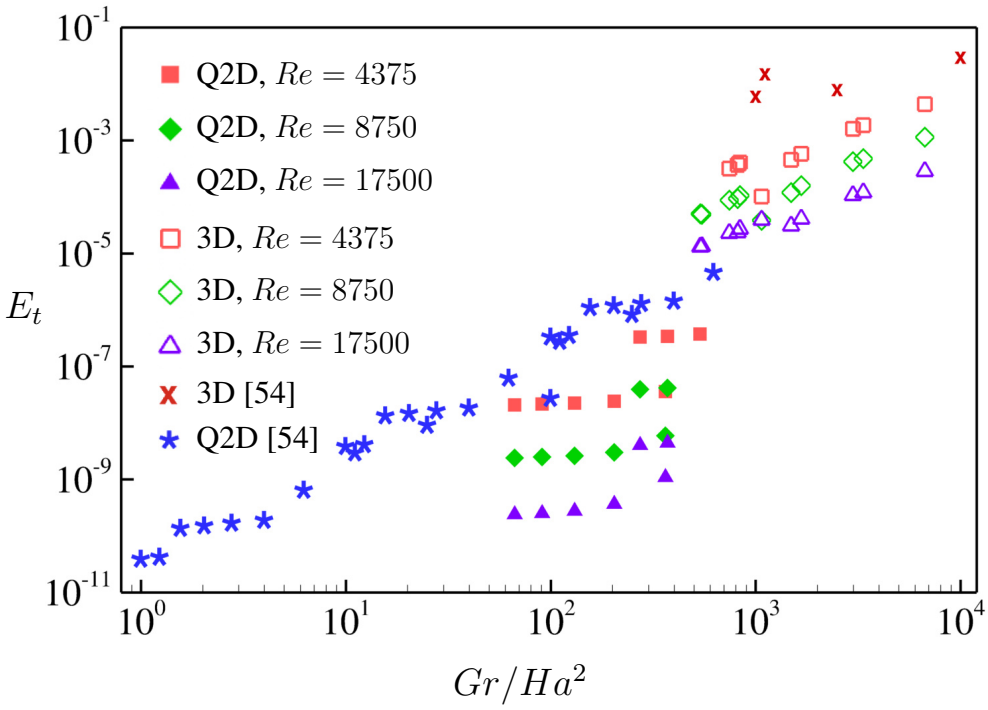

Figure 3.19: The average kinetic energy of transverse circulation in the base flow E_t as a function of Gr/Ha^2. Q2D and 3D indicate regimes found in this work for the flow at $\Gamma = 3.5$. Values of E_t and Gr/Ha^2 for each computed flow can be found in tables 3.3, 3.6, 3.7, 3.8.

evident conclusion from the parametric study data is that MCFs are fully present in the investigated flows. The fluctuations are observed in the entire duct. The signals are regular and dominated by one or several low frequencies at $Re = 8750$ and $Re = 17500$ for $Gr = 10^8$ and $Gr = 4.1 \times 10^8$. The amplitude of velocity signals decreases noticeably at all the measured points with growing Re at fixed Gr and Ha (see 3.23b, d or 3.23f, h). Comparison of the non-dimensional temperature signals demonstrates that the value of Re has practically no effect on the MCFs (see 3.23a, c or 3.23e, g).

Additionally, dimensional evaluation of the parameters of the MCFs is done (similar to the procedure discussed in section 3.3.4). Liquid mercury flows in the duct with the half-width of $d = 2.8\ cm$ are considered. The physical properties of Hg are taken at 303 K [9]. The wall heat rate is $q = 9.59\ kWm^{-2}$ at $Gr = 10^8$ and $q = 39.4\ kWm^{-2}$ at $Gr = 4.1 \times 10^8$. The results of nonlinear simulations allow us to predict the largest

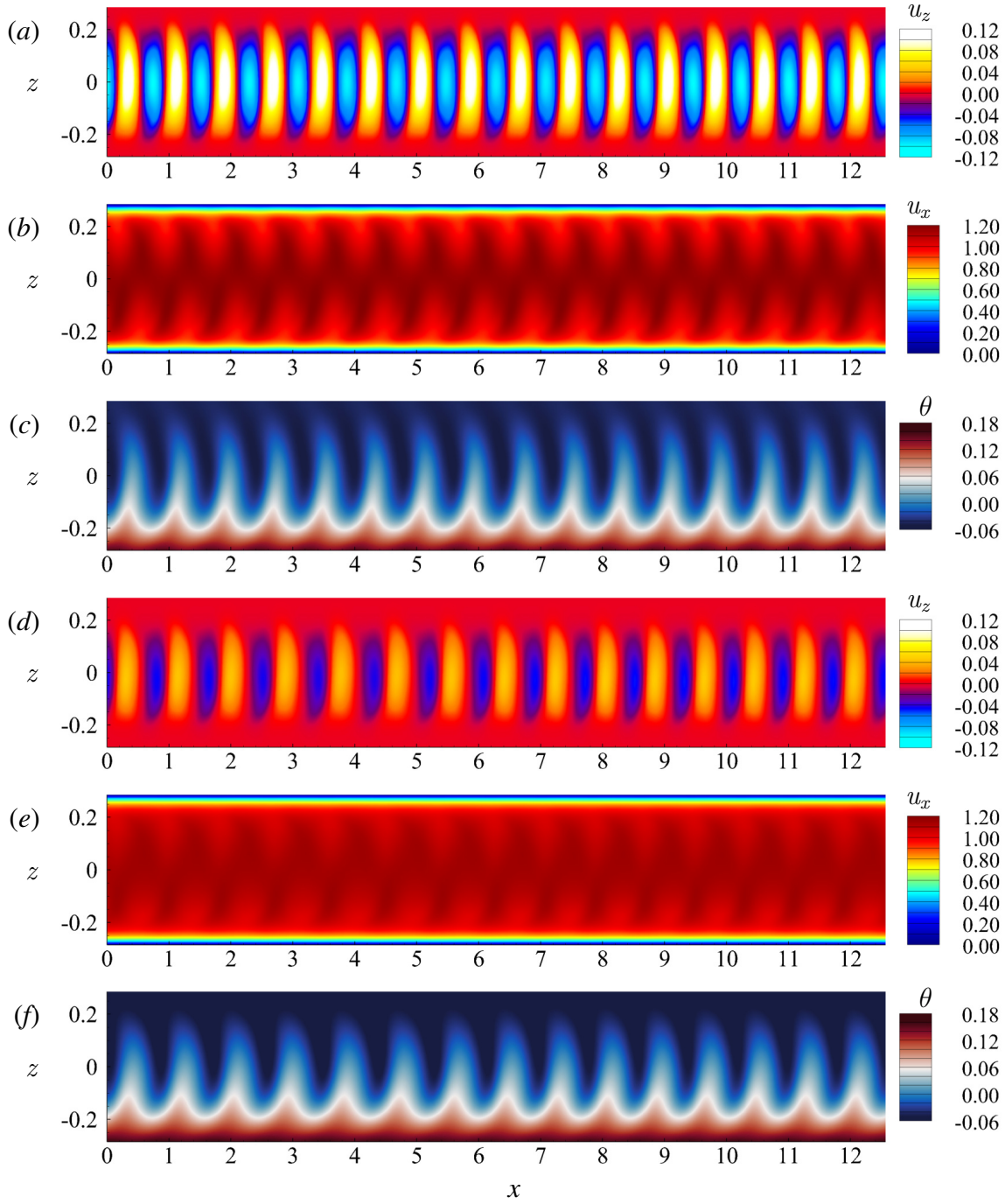

Figure 3.20: Flow structure in nonlinear regime at $Re = 8750$ (a-c) and $Re = 17500$ (d-f) for $Ha = 1225$, $Gr = 10^8$. The instantaneous distributions of u_z (a, d), u_x (b, e), and θ (c, f) obtained in the 2D model are shown.

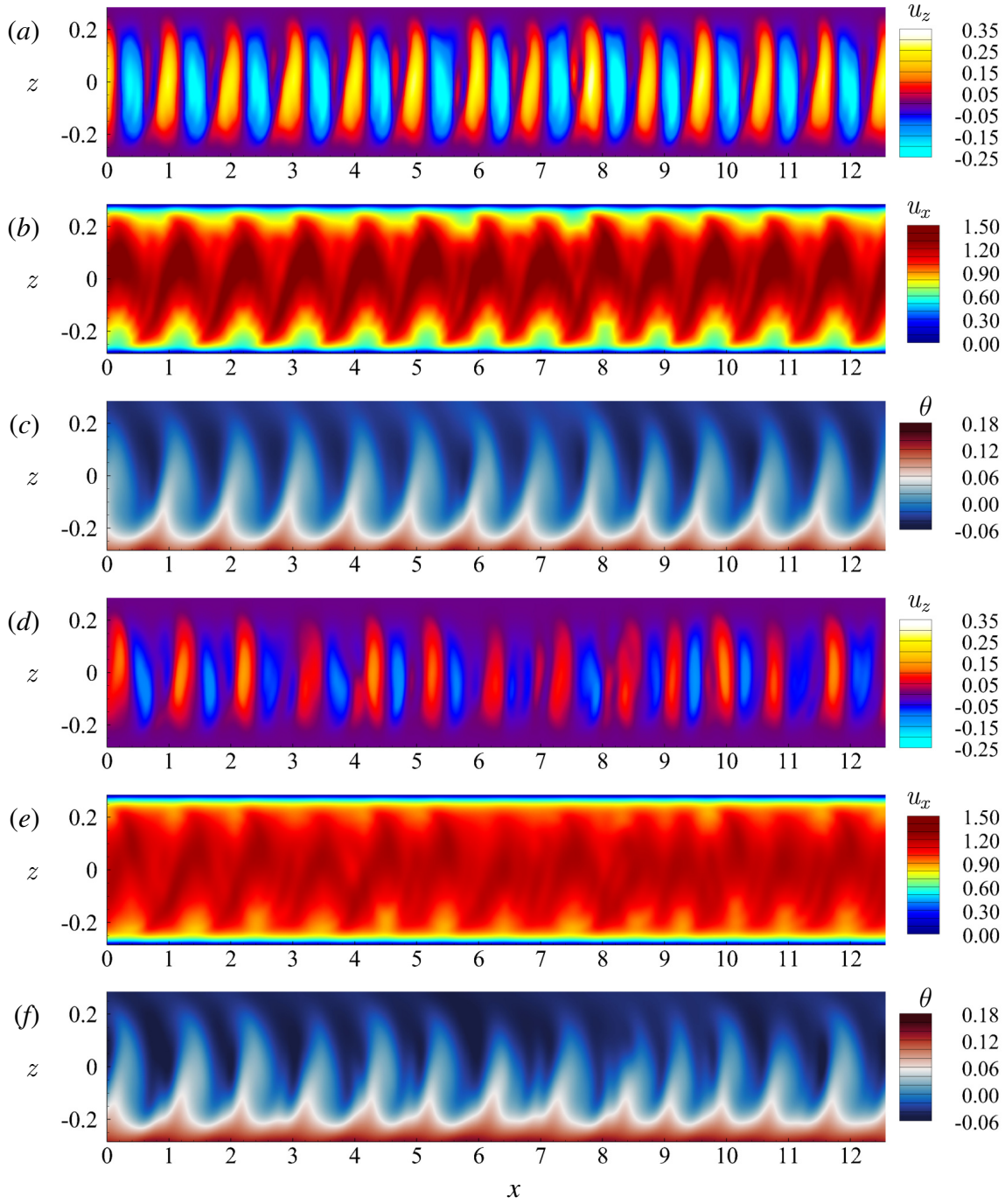

Figure 3.21: Flow structure in nonlinear regime at $Re = 8750$ (a-c) and $Re = 17500$ (d-f) for $Ha = 1225$, $Gr = 4.1 \times 10^8$. The instantaneous distributions of u_z (a, d), u_x (b, e), and θ (c, f) obtained in the 2D model are shown.

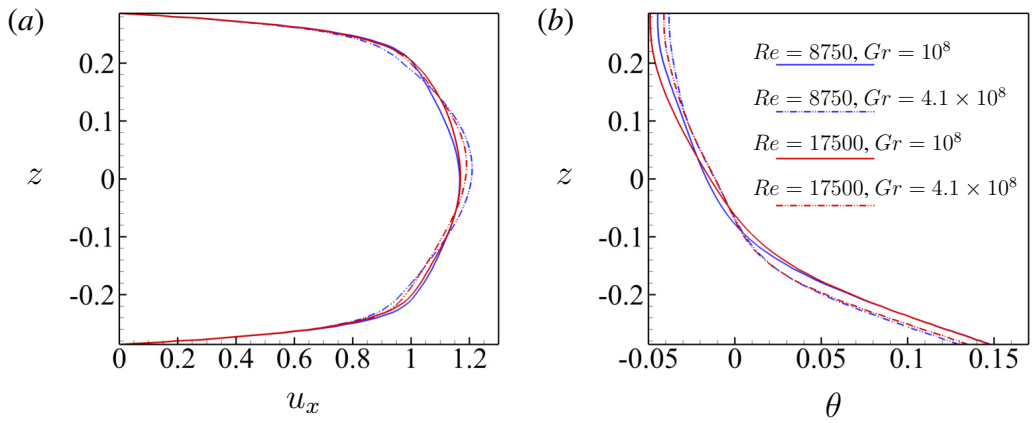

Figure 3.22: The profiles of u_x and θ in nonlinear regime for $Re = 8750$ and 17500 at $Ha = 1225$, $Gr = 10^8$ and 4×10^8 obtained by averaging over x and time are shown, respectively, in (a) and (b).

amplitude of fluctuations of temperature in the middle of the duct. The amplitudes are in the range of $2-3\ K$ at $Gr = 10^8$, $Ha = 1225$ and $6-12\ K$ at $Gr = 4.1\times10^8$, $Ha = 1225$ for $Re = 8750$ and $Re = 17500$. These ranges are consistent with earlier results shown in section 3.3.4.

3.4 Concluding Remarks

Mixed convection in a liquid metal flow in a duct with bottom heating and transverse magnetic field has been analyzed. The analysis is extended to much higher values of Ha and Gr than the previous analysis of similar effects in [17].

The main conclusion of the work is that magnetoconvective fluctuations appear at the parameters anticipated for operational regimes of blankets and divertors of future fusion rectors. The fluctuations are not suppressed or even significantly reduced in amplitude by the very strong magnetic field. The amplitude remains high, reaching tens or hundreds degrees K (depending on the value of Gr and Re) in a typical duct geometry. Moreover, the parametric study reveals that the amplitude of magnetoconvective fluctuations is nearly insensitive to increase of Re at fixed Ha and Gr in liquid metal flows. This has significant far-reaching implications for mixing, heat and mass transfer, and structural integrity of

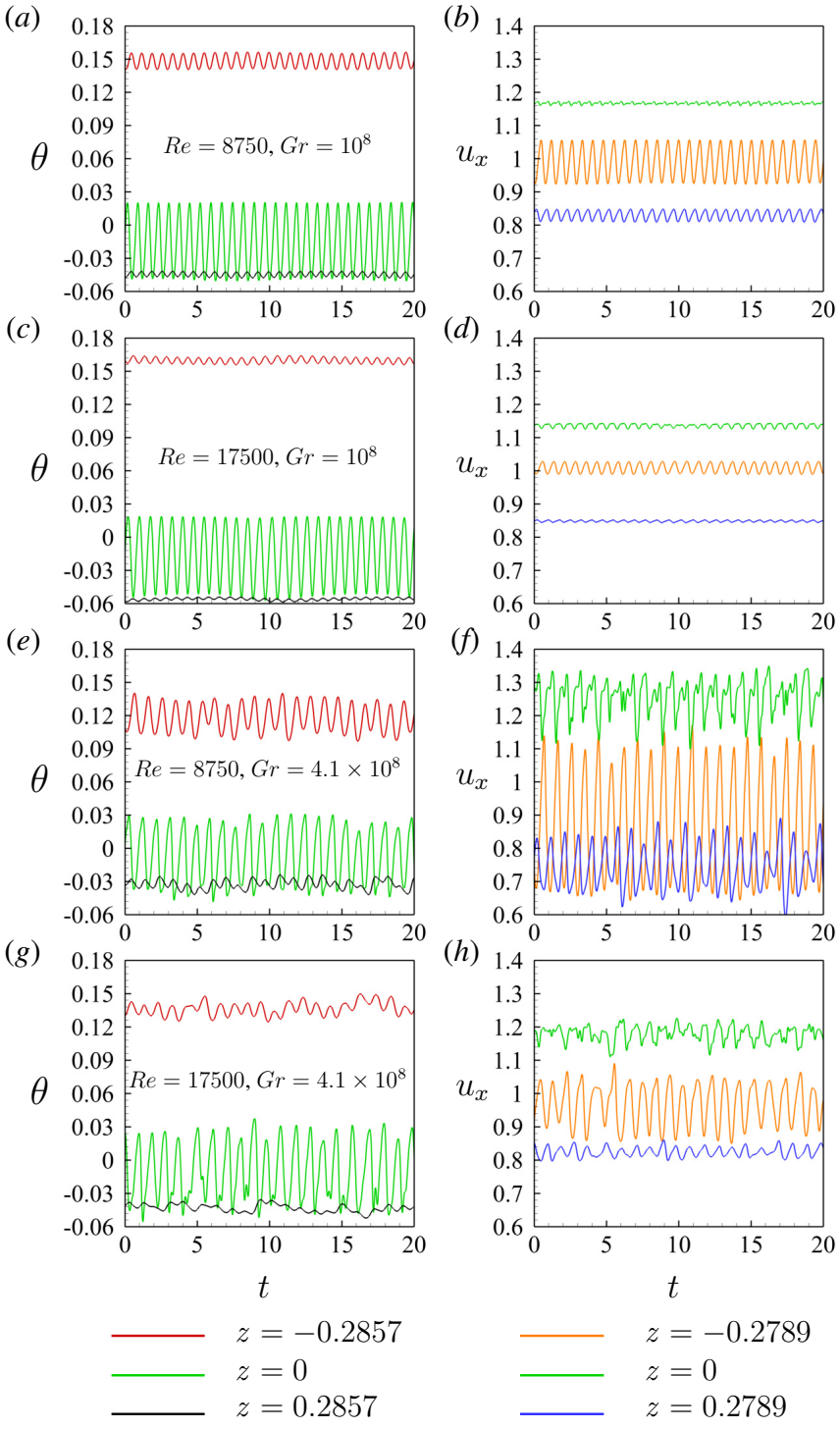

Figure 3.23: Time signals of temperature and streamwise velocity in the nonlinear regime at $Ha = 1225$ are shown in the left and right columns, respectively. The regimes at $Re = 8750$ are shown in (a, b) and (e, f) for $Gr = 10^8$ and $Gr = 4.1 \times 10^8$, respectively. The regimes at $Re = 17500$ are shown in (c, d) and (g, h) for $Gr = 10^8$ and $Gr = 4.1 \times 10^8$, respectively. The parameters Re and Gr are indicated in the left column.

reactor components. The most dangerous modes of the instability have the form of rolls localized in the lower half of the duct and having the streamwise wavelength measured in horizontal half-widths of the duct, approximately, between 0.8 and 1.4 at $Gr = 10^8$, 0.6 at $Gr = 10^9$, and 0.4 at $Gr = 10^{10}$ for $Re = 5000$.

Another conclusion concerns applicability of the two-dimensional approximation in [21] to flows with thermal convection. It has been found that the approximation may become inaccurate at high values of Gr even though the flow remains quasi-two-dimensional. Full reasons of this phenomenon remain to be understood. One of the reasons is, clearly, the geometry of the flow. The 2D model tends to be less accurate if applied to flows in ducts with larger aspect ratios and the magnetic field parallel to the long side. In general, the conclusion is important as a warning against application of the model without a proper verification.

It is pertinent to stress that the conclusions are obtained based on a single configuration of a horizontal duct flow with bottom heating and transverse magnetic field. At the same time, there are multiple indications that similar behaviors can be observed in other configurations related to the existing designs of liquid metal blankets of fusion reactors. This will need to be explored in future studies.

CHAPTER 4

Modal Analysis of Magnetoconvection

4.1 Motivation and Review

A variety of flow configurations are characterized by a wide range of spatiotemporal features caused by turbulence, nonlinearities, and instabilities. The analysis of such flows requires access to highly resolved data that capture the dynamics at the smallest length and time scales. The rapid progress in experimental measurement techniques and computational hardware over the last few decades made it possible to explore them. Nevertheless, it has become widespread practice in the analysis of such flows to seek for and retrieve physically essential characteristics [78, 79]. This procedure usually utilizes a modal decomposition that is a mathematical technique to extract energetically and dynamically important features of fluid flows. The spatial features of the flow are called spatial modes. They are accompanied by characteristic values that reflect either the energy content levels or growth rates and frequencies. The spatial modes can be determined from an experimental or numerical dataset of the flow field. The modal decomposition techniques that take flow field data as input to the analysis are referred as data-based techniques.

There have been many studies revealing that many flows share low-dimensional features integrated into high-dimensional dynamics across a wide spectrum of non-dimensional flow parameters (Re, Pr, Gr, Ra, etc.). The common examples of these prominent features include the von Kármán vortex shedding, Kelvin–Helmholtz instability, and vortex pair-

(a)

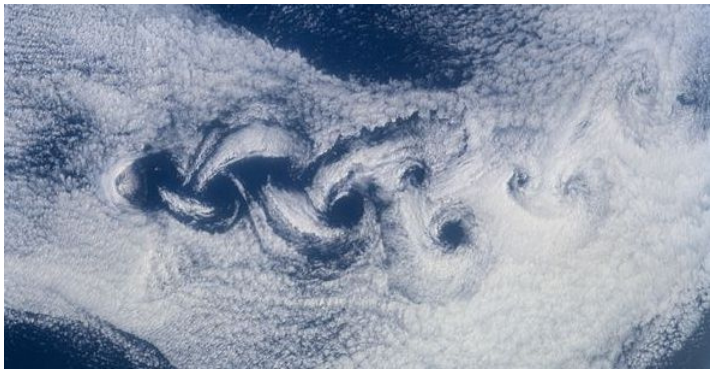

(b)

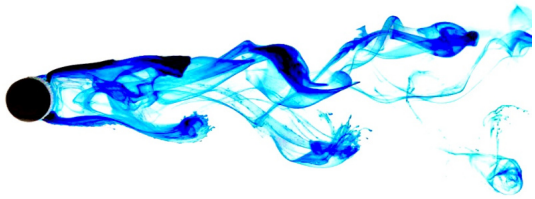

Figure 4.1: Von Kármán vortex street generated by the Rishiri Island in Hokkaido, Japan (www.images.nasa.gov) (a) and a 3D Kármán vortex street behind a cylinder produced at a low Re in water (www.flowvis.org) (b).

ing/merging (see, e.g., [80–82]). A particularly striking example is the qualitative similarity between the von Kármán vortex street generated by the Rishiri Island in Japan and the 2D low-Re flow over a circular cylinder illustrated in figure 4.1. It implies the presence of the common spatial features that capture the fundamentals of the flow physics at vastly different Reynolds numbers. One may anticipate that these prominent features will give a way to characterize a complex high-dimensional flow in a low-dimensional form. Moreover, as research methodologies enhance their capacity to produce large-scale high-fidelity data, the compression of a huge amount of flow field data to a low-dimensional form becomes increasingly relevant. It is helpful in the analysis of complex fluid flows and the development of models to investigate and simulate their dynamical behavior.

In addition to flow analysis, the modal decomposition techniques can be utilized to facilitate reduced-order flow modeling. They provide an efficient approach to determine

an effective low-dimensional coordinate system for capturing dominant flow processes. The selection of a proper coordinate system to describe the fluid flow is related to the reduction of the system order. There are many approaches for modeling and controlling fluid flows that have been implemented to investigate complex physics phenomena in different flow configurations (see, e.g., [83–87]). The well-established techniques of spatial modal representations used in such investigations include the proper orthogonal decomposition (POD), dynamic mode decomposition (DMD), linear stability analysis and others. One of the most extensively utilized techniques for a low-dimensional basis among them is the POD (discussed in section 4.2). Fundamental analysis of fluid flows, reduced-order modelling (ROM), flow control, data compression and reconstruction are just a few of the applications for the POD technique.

The results in Chapters 2 and 3 have shown us the dramatic way magnetoconvection changes the nature of flows of electrically conducting fluids. A notable example of such changes is the suppression of flow at strong magnetic fields in PRBC that results in the flow regime dominated by Q2D convection rolls aligned with the field. They appear in a wide range of non-dimensional flow parameters and, as indicated by our results and the results of earlier works (see, e.g., [9, 16–18]), in various duct and pipe geometries. One can anticipate that these regimes might be prominent candidates for the modal decomposition techniques for extracting physically important features. Although, the roll-like structures can be accurately and effectively approximated with the modal decomposition technique, its applicability to magnetoconvection nowadays remains poorly explored, setting up the motivation for the present study.

To the best of my knowledge, this study is the first to analyze modal decomposition in application to magnetoconvection. The focus of the investigation is on the magnetoconvection in the range of very high Gr and Ha including the values typical for a reactor blanket and divertor. This study follows the results reported in Chapter 3. Modal decomposition analysis based on the snapshot POD is performed for the Q2D regimes of the flow

in a horizontal duct with bottom heating and strong transverse magnetic field (see section 3.3.1).

4.2 Proper Orthogonal Decomposition

The POD, also known by many other names including the Karhunen–Loéve procedure [88, 89], originates from the field of turbulence. It was first introduced to the fluid-dynamics community as a mathematical technique to extract coherent structures from turbulent flowfields several decades ago in [90]. The POD is a modal decomposition technique for extracting modes. It provides an algorithm for decomposing a set of data into the fewest possible basis functions (modes) in order to capture as much energy as possible [78,79,91].

The general idea behind the POD is to assume that the fluctuating component of a vector field can be decomposed in the following way

$$\boldsymbol{q}(\boldsymbol{x},t) - \bar{\boldsymbol{q}}(\boldsymbol{x}) = \sum_k a_k(t)\boldsymbol{\Phi}_k(\boldsymbol{x}) \tag{4.1}$$

where $\boldsymbol{q}(\boldsymbol{x},t)$ and $\bar{\boldsymbol{q}}(\boldsymbol{x})$ are a vector field and its temporal mean, respectively. $\boldsymbol{\Phi}_k(\boldsymbol{x})$ and $a_k(t)$ are a set of orthogonal modes and with their corresponding temporal coefficients, respectively.

4.2.1 Algorithm

There are inputs and output in the POD. For the former, snapshots of any scalar (e.g., pressure, temperature) or vector (e.g., velocity) field over one-, two-, or three-dimensional discrete spatial points x at discrete times t_k are used. It needs to be mentioned that the term snapshot is used to refer to flowfield data collected at an instance in time. For the outputs, we have a set of orthogonal modes $\boldsymbol{\Phi}_k(\boldsymbol{x})$ with their time coefficients $a_k(t)$ and energy levels λ_k arranged in the order of their relative amount of energy.

Two main approaches to perform the POD of the flowfield data are discussed: the

spatial POD in section 4.2.1.1 and the snapshot POD in section 4.2.1.2. Let us illustrate the algorithms for $n = nx \times nz -$ dimensional problem of the pressure field p calculated by DNS.

4.2.1.1 Spatial POD

The POD is used to determine the set of basis functions that best describes the provided flowfield data. The first step in the decomposition method is to prepare snapshots of the given flowfield $p(\boldsymbol{x}, t)$ by reordering them into a set of finite-dimensional column vectors $p'(\boldsymbol{x}, t)$ each representing a given flowfield:

$$p'(\boldsymbol{x}, t) = p(\boldsymbol{x}, t) - \bar{p}(\boldsymbol{x}) = \sum_k a_k(t)\boldsymbol{\Phi}_k(\boldsymbol{x}) \in \mathbb{R}^n. \tag{4.2}$$

Assume that there is a set of m fluctuating fields. The dataset is reordered by concatenating each individual pressure field into one single $1 \times n$ row and those rows are stacked onto each other for each instant t_k. The data of the fluctuating pressure field can be summarized into one $m \times n$ snapshot matrix P:

$$P_{m,n} = \begin{pmatrix} p_{1,1} & \cdots & p_{1,n} \\ p_{2,1} & \cdots & p_{2,n} \\ \vdots & \ddots & \vdots \\ p_{m,1} & \cdots & p_{m,n} \end{pmatrix} = \begin{pmatrix} p'(x_1, z_1, t_1) & \cdots & p'(x_{nx}, z_{nz}, t_1) \\ p'(x_1, z_1, t_2) & \cdots & p'(x_{nx}, z_{nz}, t_2) \\ \vdots & \ddots & \vdots \\ p'(x_1, z_1, t_m) & \cdots & p'(x_{nx}, z_{nz}, t_m) \end{pmatrix}, \tag{4.3}$$

where each row represents one snapshot at a particular time calculated by DNS.

The objective of the POD is to find the vectors $\boldsymbol{\Phi}_k(\boldsymbol{x})$ in equation (4.2) that can optimally represent $p'(\boldsymbol{x}, t)$, i.e., with the least number of modes. The solution to this problem can be resolved by finding the eigenvectors $\boldsymbol{\Phi}_k$ and the eigenvalues λ_k from

$$C\boldsymbol{\Phi}_k = \lambda_k \boldsymbol{\Phi}_k, \tag{4.4}$$

where $\mathbf{\Phi}_k \in \mathbb{R}^n$, $\lambda_1 \geq \lambda_2 \ldots \lambda_n \geq 0$ and C is the covariance matrix of vector $p'(\boldsymbol{x}, t)$. The size of the covariance matrix based on the number of spatial degrees of freedom of the data n, so it is, generally, large:

$$C = \frac{1}{m-1} P^T P \in \mathbb{R}^{n \times n}. \tag{4.5}$$

It should be mentioned that the eigenvectors found in equation (4.10) are called the POD spatial modes. The modes are orthonormal which means that in a suitable function space one can write

$$\iiint_x \mathbf{\Phi}_{k1}(\boldsymbol{x}) \mathbf{\Phi}_{k2}(\boldsymbol{x}) d\boldsymbol{x} = \begin{cases} 1, & k_1 = k_2 \\ 0, & k_1 \neq k_2 \end{cases}. \tag{4.6}$$

The orthonormality property implies that each time coefficient $a_k(t)$ can be determined as

$$a_k(t) = \iiint_x p'(\boldsymbol{x}, t) \mathbf{\Phi}_k(\boldsymbol{x}) d\boldsymbol{x}. \tag{4.7}$$

The eigenvalues indicate how effectively each eigenvector in the L_2 sense matches the original data. When a vector field is used for P, the kinetic energy captured by the individual POD modes is represented by the eigenvalues. The POD modes are ranked in order of relevance in terms of capturing the kinetic energy of the flowfield if the eigenvalues are ordered from the biggest to the lowest in decreasing order. Considering the eigenvalues, we can keep only the first r modes which represent the fluctuations in the flowfield data so that

$$\sum_j^r \lambda_j / \sum_j^n \lambda_j \approx 1. \tag{4.8}$$

Therefore, the flowfield can be represented in terms of the truncated series

$$p'(\boldsymbol{x}, t) = p(\boldsymbol{x}, t) - \bar{p}(\boldsymbol{x}) \approx \sum_{k=1}^{r} a_k(t) \mathbf{\Phi}_k(\boldsymbol{x}). \tag{4.9}$$

4.2.1.2 Snapshot POD

The method of the snapshot POD was originally introduced in [92]. The spatial POD uses the decomposition involving deterministic spatial modes and random time coefficients as it was shown in section 4.2.1.1. Since mathematically there is no fundamental difference between the temporal variable t and the spatial variable $\boldsymbol{x}$, we could also see it as a decomposition in deterministic temporal modes with random spatial coefficients. This alternative approach is useful when the spatial size of the data n is very large, so the size of the correlation matrix C becomes very large. The number of snapshots m is usually much smaller than n.

The snapshot approach is based on solving a much smaller eigenvalue problem:

$$PP^T\boldsymbol{\Psi}_k = \lambda_k\boldsymbol{\Psi}_k, \tag{4.10}$$

where $\boldsymbol{\Psi}_k \in \mathbb{R}^m$ and $m \ll n$.

The covariance matrix is in $R^{m\times m}$ thus the decomposition is performed in m-dimensional space. As a result, there is a set of m eigenvalues and eigenvectors. The eigenvectors are temporal modes now that play the same role as the m time coefficients of the spatial POD. The spatial modes can be obtained by projecting the data onto the temporal modes by $\boldsymbol{\Phi s}_k = P^T\boldsymbol{\Psi}_k$. The new matrix consists of the m spatial coefficients ordered from the 'strongest' in the first column to the 'weakest' in the last column.

The eigenvalues calculated using the snapshot approach are identical to those calculated using the spatial method, while the spatial coefficients and temporal modes differ by a multiplicative factor. In the spatial POD, the spatial modes are orthonormal since they result from the eigendecomposition of the symmetric covariance matrix but the time coefficients are not. The situation is different in the snapshot POD. In order to match the results of both methods, each spatial coefficient of the snapshot POD needs to be normalized and temporal modes need to be scaled accordingly. This will ensure that the results of the snapshot POD

are identical to those of the snapshot method.

The MATLAB code of the n-dimensional snapshot POD with the normalization procedure as described above is shown in figure 4.2 [93]. The raw pressure data is organized as a 3D array $S(i, j, k)$ where the first and second indexes correspond to the z and x coordinates, respectively, and the third corresponds to time.

```
% 1 - Upload the high-resolution flowfield data

S = load('DNS.dat');

% 2 - Create the snapshot matrix
Nt = length(S(1,1,:));
S = reshape(permute(S, [3 2 1]), Nt, [ ]);
    % Reshape data into a matrix S with Nt rows
P = S - repmat(mean(S,1), Nt, 1);
    % Subtract the temporal mean from each row

% 3 - Create the correlation matrix
C_s = (P*P')/(Nt-1);

% 4 - Solve the eigenvalue problem
[A_s, LAM_s] = eig(C_s,'vector');

% 5 - Sort eigenvalues and eigenvectors in the descending order
[lambda_s,ilam_s] = sort(LAM_s,'descend');

% 6 - Assign the temporal modes
A_s = A_s(:, ilam_s);

% 7 - Calculate the spatial coefficients
PHI_s = P'*A_s;

% 8 - Reconstruct the k-th snapshot POD mode
k = 1;
Utilde_k_s = A_s(:,k)*PHI_s(:,k)';

% 9 - Normalization in order to match spatial and snapshot POD modes
PHI = normc(PHI_s);             % Spatial modes
A = P*PHI;                      % Time coefficients
Utilde_k = A(:,k)*PHI(:,k)';    % Reconstruction on k-th mode

```

Figure 4.2: The MATLAB code of the n-dimensional snapshot POD [93].

4.2.2 Strengths and Weaknesses

There are pros and cons in using the POD in the analysis of magnetoconvection that need to be mentioned. The main strengths are the following: 1 - the POD produces a low

dimensional orthogonal set of basis vectors. It is an attractive property for constructing ROMs. The prominent example is the use of the Galerkin projection-based ROM [94, 95]; 2 - POD modes are simple to compute and use for high-dimensional spatial datasets; 3 - by simply removing the high-order modes from the expansion (4.2), the POD analysis can be used to drastically reduce noise in the dataset and focus the analysis on the coherent structures dominating the flow; 4 - the POD analysis is very widely used in a broad spectrum of studies as it has been mentioned earlier.

Nevertheless, there are some weaknesses: 1 - the temporal coefficients of spatial POD modes comprise a mixture of frequencies in most cases, however, this can be addressed by the spectral POD [96]; 2 - the POD organizes modes according to their energy contents rather than their dynamical relevance. Balanced POD and DMD analyses can be used to tackle this problem [97, 98]; 3 - it is not always apparent how many POD modes should be kept while there are many different truncation criteria.

4.3 Results

All the results of the modal analysis carried out for Q2D regimes are presented in table 4.1 and in the figures $4.3 - 4.11$. The flow fields of velocity, temperature and pressure in these regimes are analyzed with the snapshot POD.

The evolution of the fully developed flow that is computed for at least 1000 time units and 2500 snapshots are utilized for the modal decomposition analysis. The problem is $n = nx \times nz = 385 \times 97 = 37345 -$ dimensional with a set of $m = 2500$ flow fields. The covariance matrix is an $m \times m$ matrix which contains 6.25 million elements. At the same time, the covariance matrix would have been an $n \times n$ with about 1.4 billion elements in the spatial POD. For such large-dimensional flowfields, the use of the snapshot approach is not just beneficial, but is a necessity.

The instantaneous distributions of flowfields in Q2D regimes with the most dominant spatial modes at $Ha = 10000$ for $Gr = 10^8$ and 10^9 are shown in figures $4.4 - 4.10$.

Number of modes	Flow field	Gr	% of $\lambda_i / \sum_k \lambda_k$	Gr	% of $\lambda_i / \sum_k \lambda_k$
5	u_x	10^8	89.11	10^9	70.99
10		10^8	96.19	10^9	85.27
20		10^8	99.23	10^9	92.69
50		10^8	99.99	10^9	97.98
100		10^8	100	10^9	99.27
200		10^8	–	10^9	99.82
300		10^8	–	10^9	99.95
5	u_z	10^8	75.80	10^9	31.98
10		10^8	86.44	10^9	52.82
20		10^8	96.44	10^9	68.36
50		10^8	99.94	10^9	87.88
100		10^8	100	10^9	96.10
200		10^8	–	10^9	99.44
300		10^8	–	10^9	99.88
5	θ	10^8	91.26	10^9	67.47
10		10^8	96.91	10^9	84.09
20		10^8	99.33	10^9	92.73
50		10^8	99.99	10^9	97.45
100		10^8	100	10^9	99.19
200		10^8	–	10^9	99.88
300		10^8	–	10^9	99.98
5	p	10^8	93.57	10^9	73.92
10		10^8	98.73	10^9	91.53
20		10^8	99.79	10^9	98.21
50		10^8	100	10^9	99.48
100		10^8	100	10^9	99.85
200		10^8	–	10^9	99.98
300		10^8	–	10^9	99.99

Table 4.1: Snapshot POD analysis of the horizontal duct flow with bottom heating and transverse magnetic field (see Chapter 3): amount of KE of fluctuations captured by the POD modes in u_x, u_z, θ and p at $Ha = 10000$ for $Gr = 10^8$ and 10^9. Total amount of the snapshots is $m = 2500$.

The mode shapes associated with the POD modes reveal the dominant energetic spatial structures in the flow. The POD modes exhibit a top-down asymmetry, indicating that the main energy structures are associated with the horizontal duct flow asymmetry (see, e.g.,

figures 4.4 or 4.5).

Interestingly, the shape and amplitude of the spatial modes is nearly insensitive to increase of Gr. At the same time, the noticeable difference is found in regard of the required modes for representing the flowfield data in two regimes. The leading modes at the lower Gr number capture about twice as much of the flow fluctuations in terms of the kinetic energy (see figure 4.3). Based on the results shown in the table 4.1 and in the figure 4.3, one can conclude that around 20 and 200 POD modes are sufficient for reconstructing, for example, the vertical velocity field at $Ha = 10000$ for $Gr = 10^8$ and 10^9, respectively. The dramatic difference can be attributed to increase of Gr leading to higher non-dimensional amplitudes of the velocity fluctuations and significant change in the flow structure, particularly in the convection rolls (see, e.g., figures 4.6a and 4.7a). The total amount of kinetic energy contained in 20 spatial modes is 96.44% at $Gr = 10^8$ while the value is just 68.36% at $Gr = 10^9$ for the vertical velocity field (see table 4.1).

4.4 Concluding Remarks

Modal analysis of magnetoconvection in a liquid metal flow in a duct with bottom heating and transverse magnetic field based on the snapshot POD has been performed. The results are performed at very high Gr and Ha typical for blanket and divertor of future nuclear fusion reactors.

The main conclusion of the work is that the snapshot POD can be applied for the Q2D regimes in a horizontal duct flow. It allows us to extract physically important features of the flows by drastically reducing the amount of the data in about 125 and 12.5 times for $Gr = 10^8$ and $Gr = 10^9$ at $Ha = 10000$, respectively, in comparison to the 2500 snapshots taken as the output for the snapshot POD. The spatial modes can be utilized for reconstruction of the original flow very effectively and accurately in future studies.

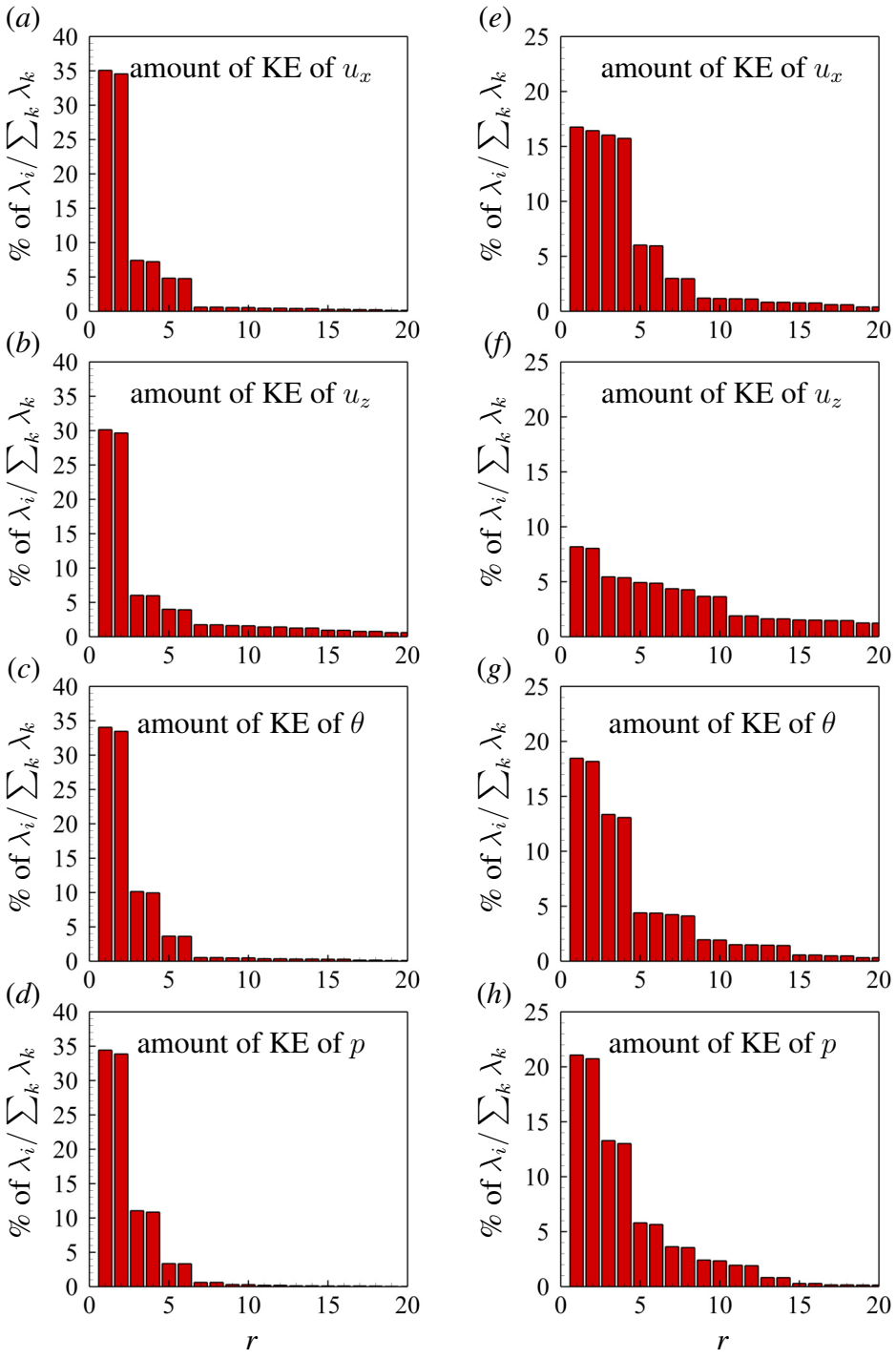

Figure 4.3: Snapshot POD analysis of the horizontal duct flow: amount of fluctuation KE captured by the first $r = 20$ POD modes in the streamwise velocity (a, e), vertical velocity (b, f), temperature (c, g) and pressure (d, h) fields in nonlinear regime at $Ha = 10000$ for $Gr = 10^8$ (left column) and $Gr = 10^9$ (right column).

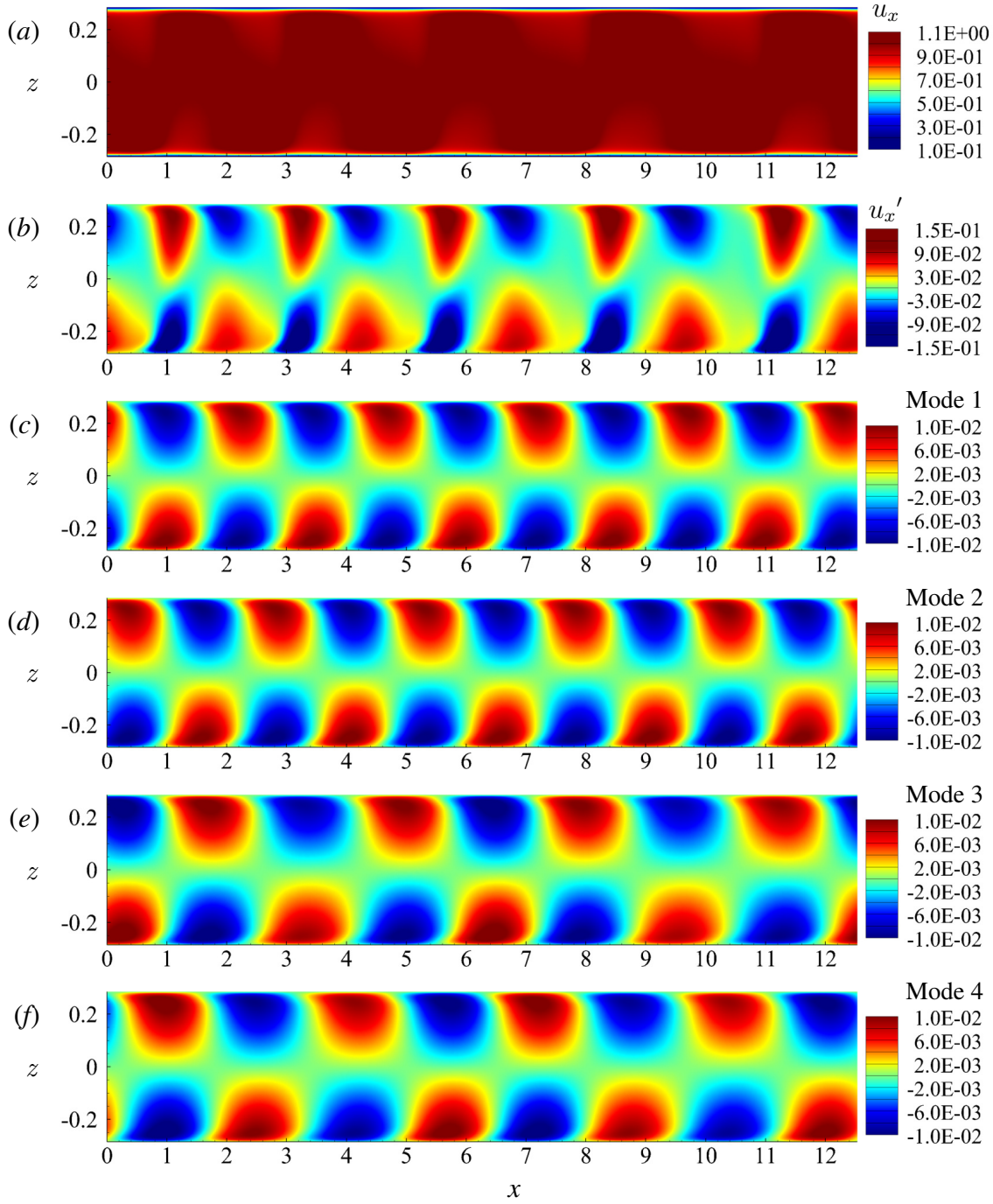

Figure 4.4: Snapshot POD analysis of the horizontal duct flow: the instantaneous distribution of u_x (a) and $u_x{}'$ (b) in nonlinear regime at $Ha = 10000$ for $Gr = 10^8$; $(c - f)$ first four spatial modes obtained in the snapshot POD for the streamwise velocity field.

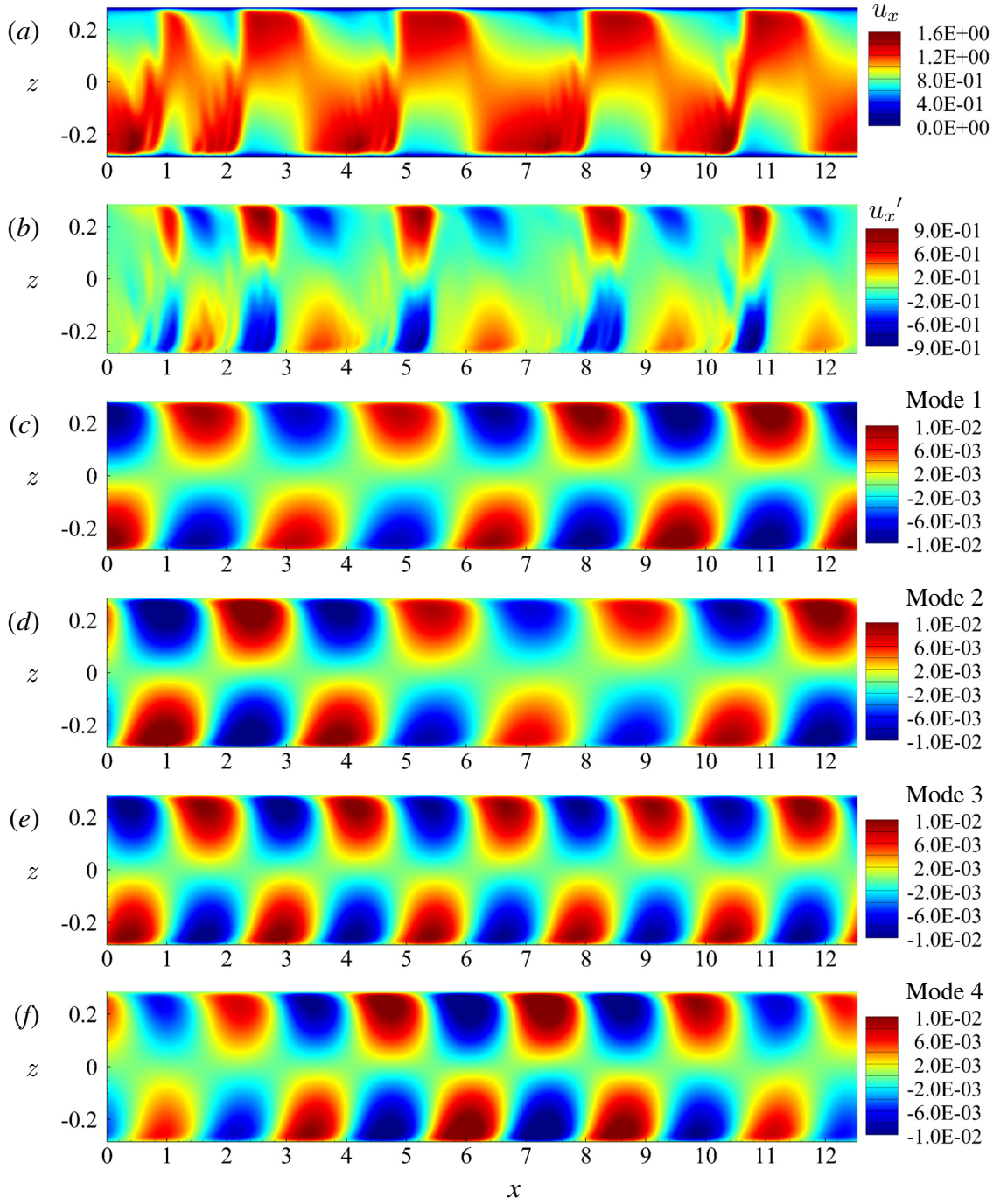

Figure 4.5: Snapshot POD analysis of the horizontal duct flow: the instantaneous distribution of u_x (a) and $u_x{}'$ (b) in nonlinear regime at $Ha = 10000$ for $Gr = 10^9$; $(c - f)$ first four spatial modes obtained in the snapshot POD for the streamwise velocity field.

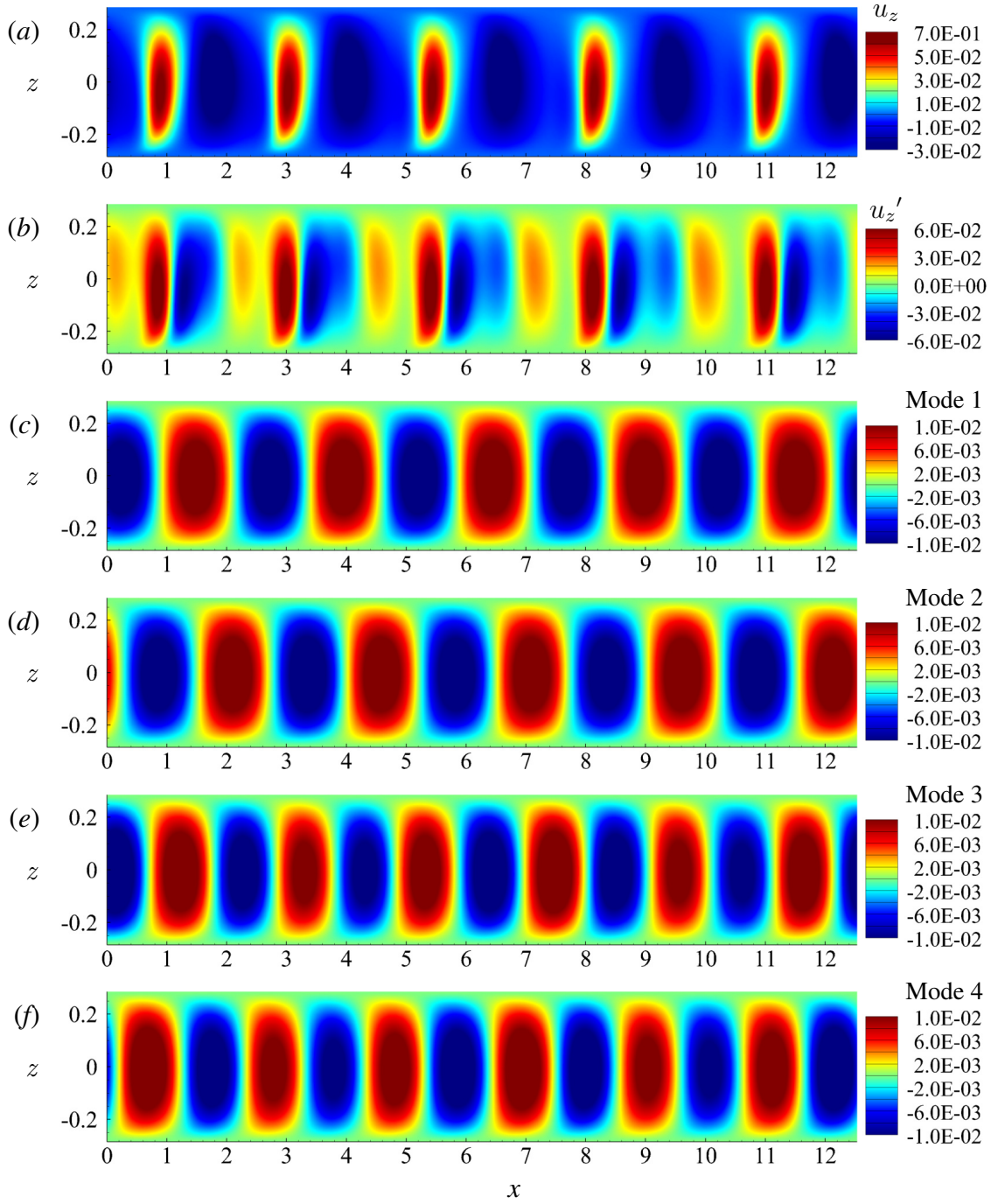

Figure 4.6: Snapshot POD analysis of the horizontal duct flow: the instantaneous distribution of u_z (a) and $u_z{}'$ (b) in nonlinear regime at $Ha = 10000$ for $Gr = 10^8$; $(c - f)$ first four spatial modes obtained in the snapshot POD for the vertical velocity field.

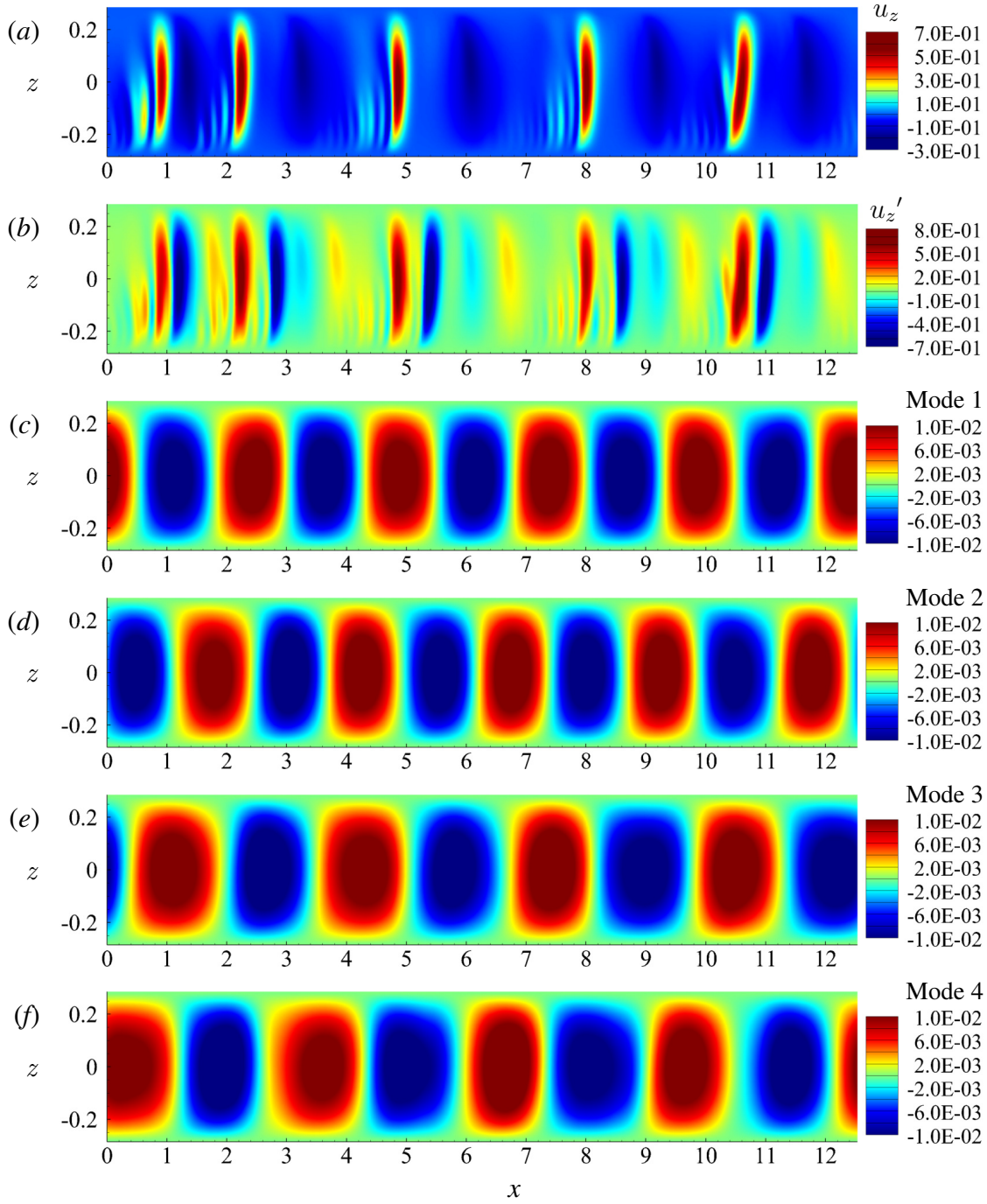

Figure 4.7: Snapshot POD analysis of the horizontal duct flow: the instantaneous distribution of u_z (a) and $u_z{}'$ (b) in nonlinear regime at $Ha = 10000$ for $Gr = 10^9$; $(c - f)$ first four spatial modes obtained in the snapshot POD for the vertical velocity field.

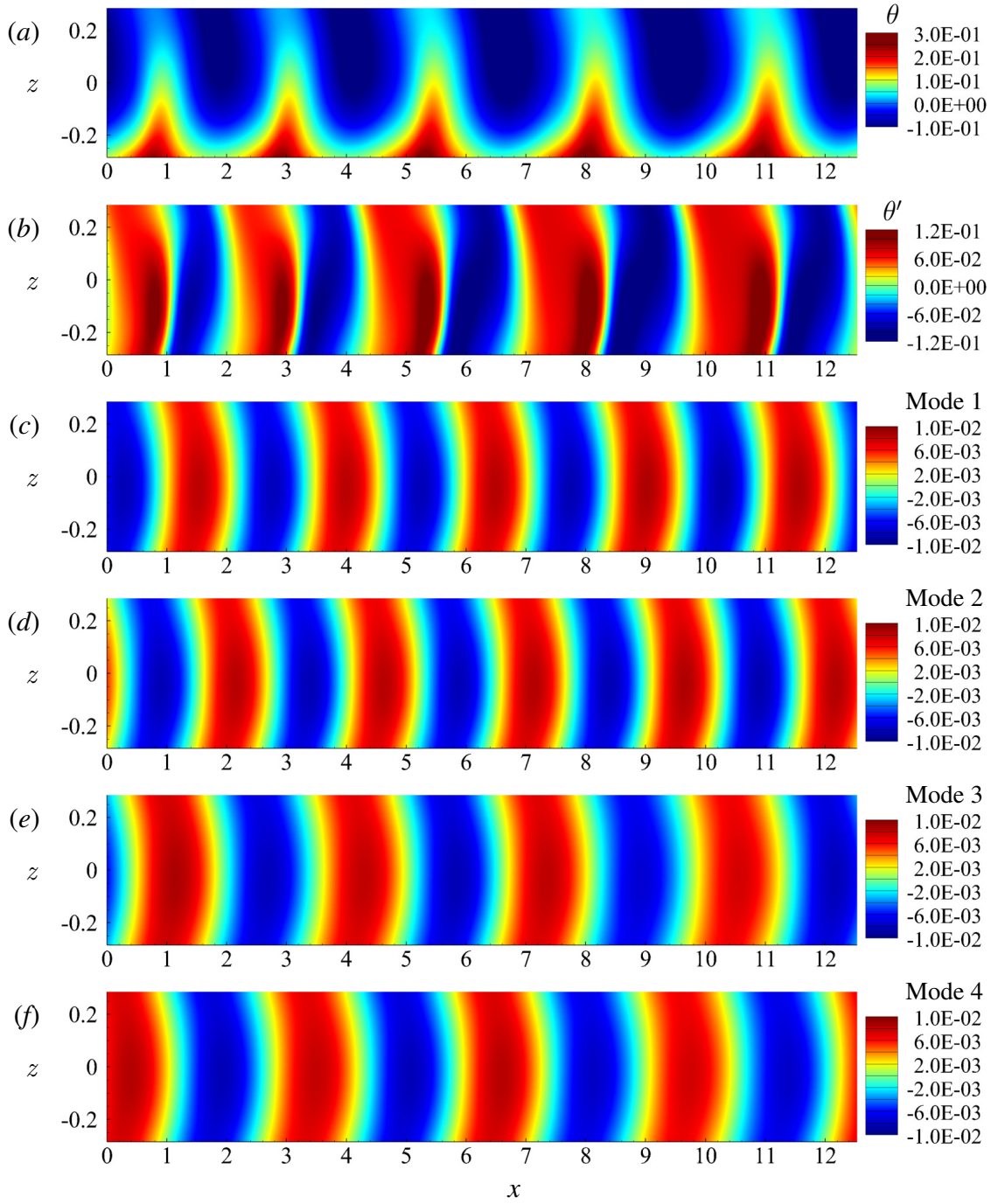

Figure 4.8: Snapshot POD analysis of the horizontal duct flow: the instantaneous distribution of θ (a) and θ' (b) in nonlinear regime at $Ha = 10000$ for $Gr = 10^8$; $(c - f)$ first four spatial modes obtained in the snapshot POD for the temperature field.

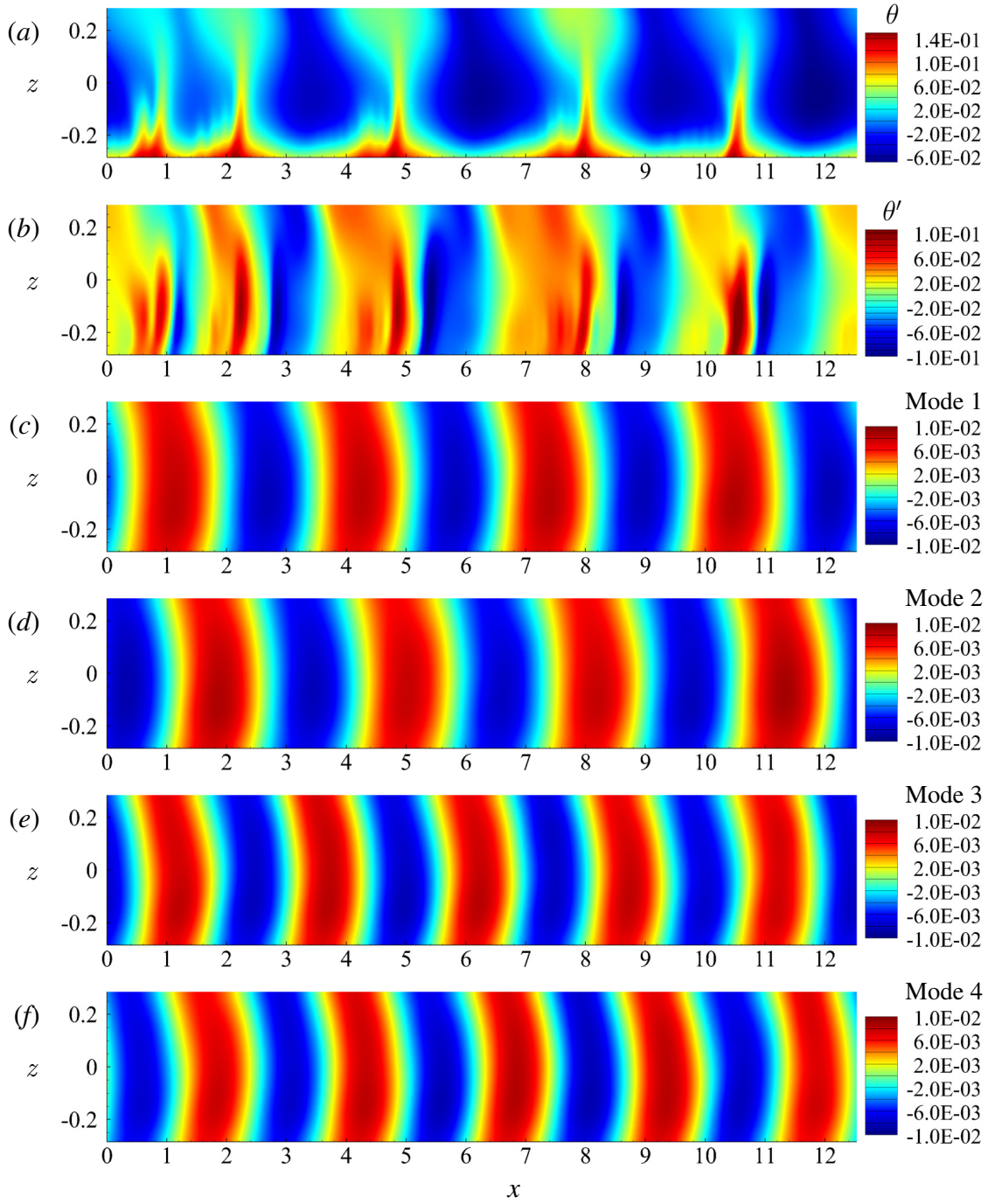

Figure 4.9: Snapshot POD analysis of the horizontal duct flow: the instantaneous distribution of θ (a) and θ' (b) in nonlinear regime at $Ha = 10000$ for $Gr = 10^9$; $(c - f)$ first four spatial modes obtained in the snapshot POD for the temperature field.

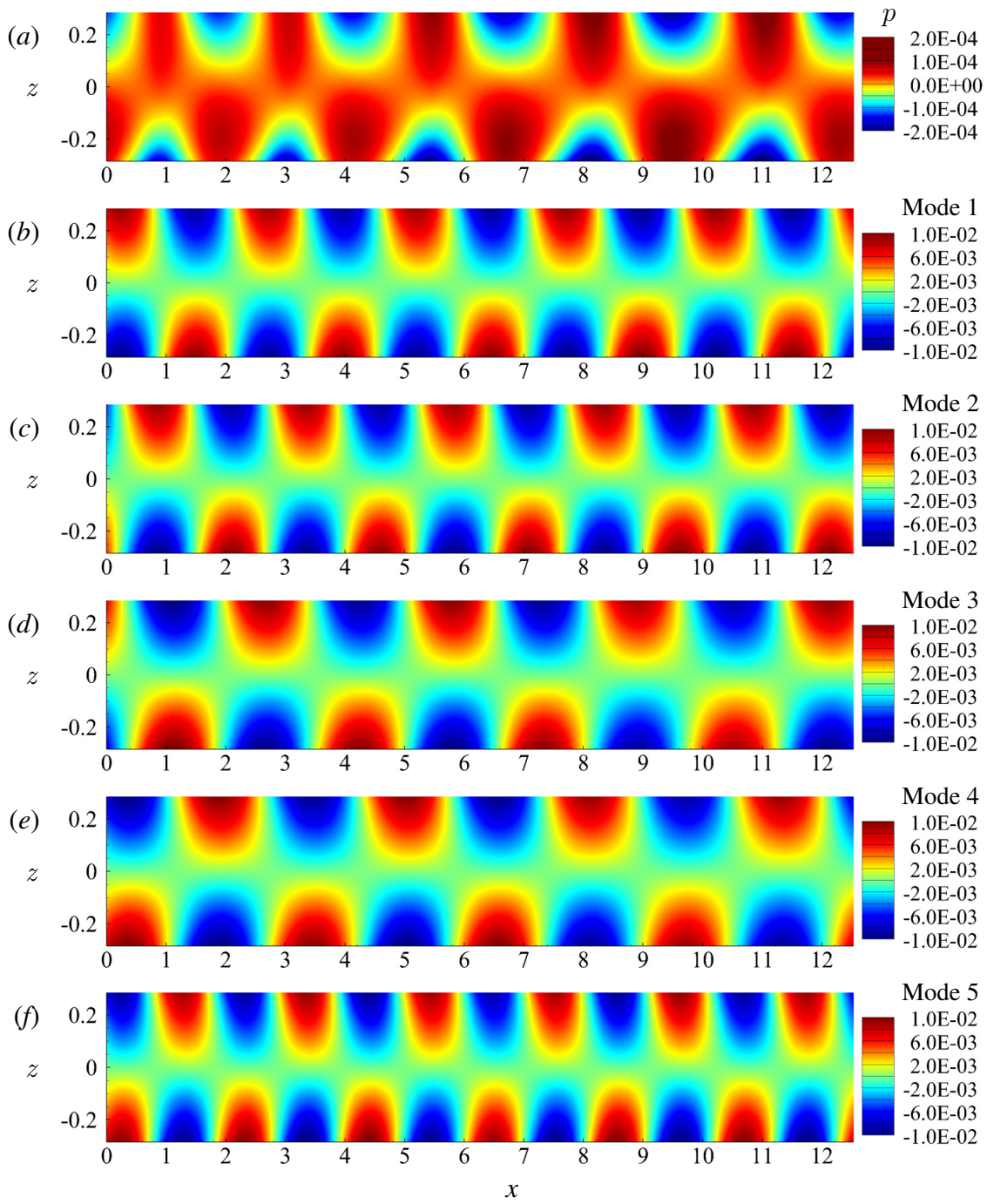

Figure 4.10: Snapshot POD analysis of the horizontal duct flow: (a) the instantaneous distribution of p in nonlinear regime at $Ha = 10000$ for $Gr = 10^8$; $(b - f)$ first five spatial modes obtained in the snapshot POD for the pressure field.

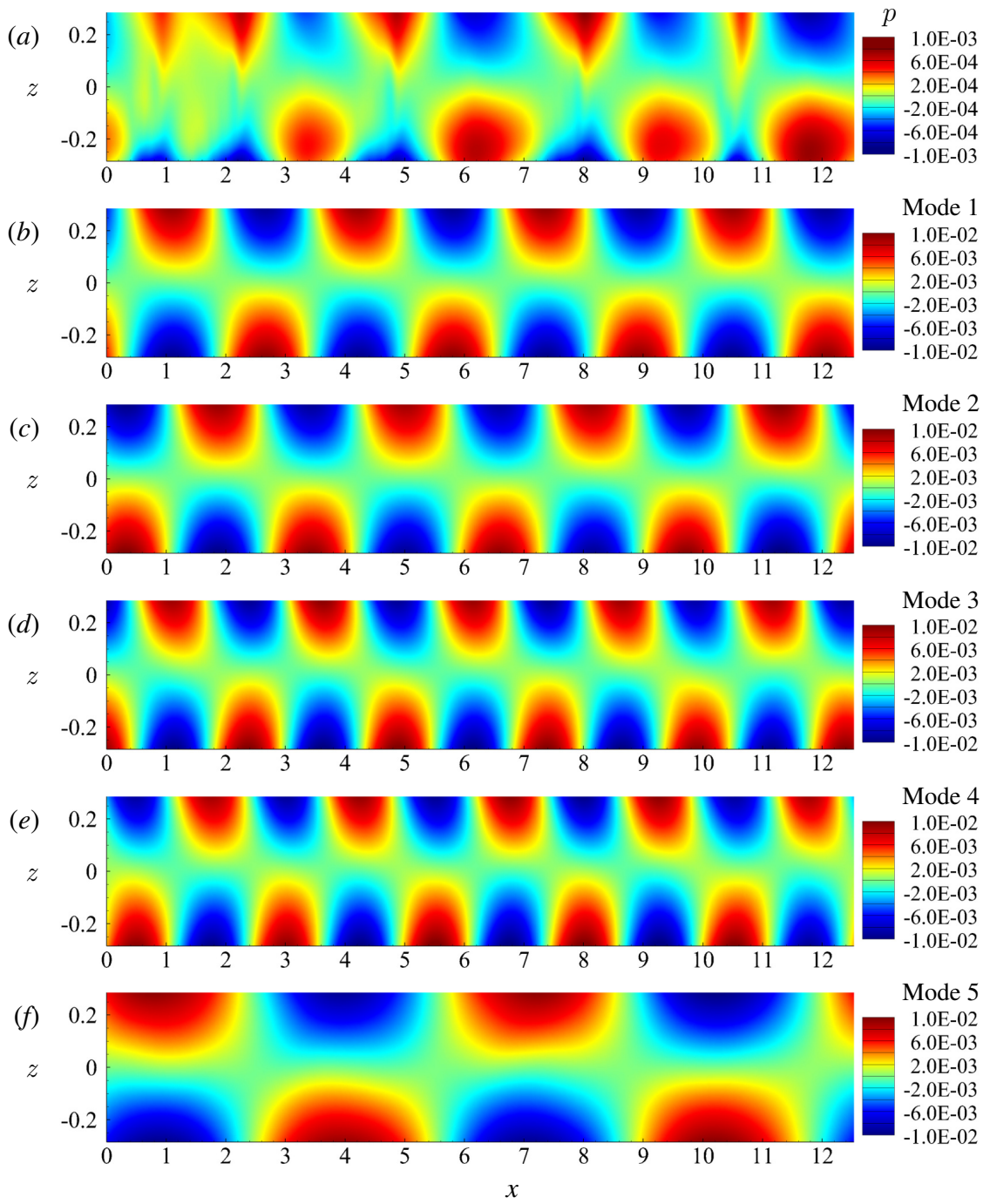

Figure 4.11: Snapshot POD analysis of the horizontal duct flow: (a) the instantaneous distribution of p in nonlinear regime at $Ha = 10000$ for $Gr = 10^9$; $(b - f)$ first five spatial modes obtained in the snapshot POD for the pressure field.

CHAPTER 5

Conclusion and Future work

The effect of magnetoconvection at very strong magnetic fields has been analyzed for two configurations: the Rayleigh-Bénard convection in a vertical cylinder and the Poiseuille-Rayleigh-Bénard flow in a horizontal duct. The applicability of the modal analysis and the accuracy of the 2D approximation have also been explored. The results of the studies are presented below.

5.1 Rayleigh-Bénard Convection

Rayleigh-Bénard convection in a vertical cylinder with imposed vertical magnetic field has been analyzed. All the concluding remarks are reported in section 2.4. The most notable findings include:

1. Identification of the new flow regime with nearly Q2D upward and downward planar jets originating at the sidewalls and extending into the flow domain is identified.

2. Existence of rotating tongue-like wall modes at $Ra \rightarrow Ra_c$.

3. Faster growth of Nu and Re with Ra in flows with strong magnetic fields.

The presented work is considered by the author as the first part of a larger and more detailed study. Future investigations of the system are undoubtedly warranted. The most

important of them are as follows: (i) to analyze the properties and physical mechanisms of the newly discovered Q2D regime; (ii) to explore the behavior of wall modes; (iii) to investigate the transport properties at much higher Ra and Ha; (iv) to study the similarities between the RBC flows with magnetic field and rotation.

5.2 Poiseuille-Rayleigh-Bénard Flow

Poiseuille-Rayleigh-Bénard flow in a horizontal duct with bottom heating and transverse magnetic field has been analyzed. All the concluding remarks are reported in section 3.4. The main findings are:

1. Magnetoconvective fluctuations appear at the parameters anticipated for operational regimes of blankets and divertors of future fusion rectors.

2. The amplitude of fluctuations remains high, reaching tens or hundreds degrees K (depending on the value of Gr and Re) in a typical duct of fusion reactor blanket.

3. The two-dimensional approximation corresponding to the asymptotic limit of a very strong magnetic field effect is validated and applied in the previously unexplored range of control parameters corresponding to typical conditions of a liquid metal blanket of a nuclear fusion reactor.

Further study of MCFs at high Hartmann and Grashof numbers is warranted by their practical importance and theoretical significance. Many interesting possible directions of future work can be suggested. Two of them appear particularly important. One is the exploration of the phenomenon for other geometries, where strong MCFs are known to exist, for example for downward flow in vertical and inclined ducts. Another particularly interesting direction is the analysis of the effects of finite thermal and electrical conductivities of the walls.

5.3 Modal Analysis of Magnetoconvecction

Modal analysis of magnetoconvection has been explored for the PRBC flow in a horizontal duct with bottom heating and transverse magnetic field. The snapshot POD is shown to be an effective technique in decomposing a complex high-dimensional flows into low-dimensional coordinate systems. The results of the investigated parameters are quite promising showing us that the magnetoconvective flows share low-dimensional features embedded in high-dimensional dynamics.

Possible directions of future work with the snapshot POD can be listed as follows: (i) investigation of the modal analysis in regard of other practical configurations in magnetoconvection; (ii) realization of accurate and effective reduced-order models based, for example, on the Galerkin projection algorithm.

BIBLIOGRAPHY

[1] P. A. Davidson, *Introduction to Magnetohydrodynamics*, 2nd ed. Cambridge, United Kingdom: Cambridge University Press, 2016.

[2] N. O. Weiss and M. R. E. Proctor, *Magnetoconvection*. Cambridge, United Kingdom: Cambridge University Press, 2014.

[3] D. H. Kelley and T. Weier, "Fluid mechanics of liquid metal batteries," *Appl. Mech. Rev*, vol. 70, no. 2, p. 020801, 2018.

[4] H. Ozoe, *Magnetic Convection*. London, United Kingdom: Imperial College Press, 2005.

[5] K. Cukierski and B. G. Thomas, "Flow control with local electromagnetic braking in continuous casting of steel slabs," *Met. Mat. Trans. B.*, vol. 39, no. 1, pp. 94–107, 2008.

[6] M. Abdou, N. B. Morley, S. Smolentsev, A. Ying, S. Malang, A. Rowcliffe, and M. Ulrickson, "Blanket/first wall challenges and required R&D on the pathway to DEMO," *Fusion Eng. Des.*, vol. 100, pp. 2–43, 2015.

[7] T. J. Dolan, R. W. Moir, W. Manheimer, L. C. Cadwallader, and M. J. Neumann, *Magnetic fusion technology*. London, United Kingdom: Springer, 2013.

[8] D. Maisonnier, I. Cook, P. Sardain, R. Andreani, L. D. Pace, R. Forrest, L. Giancarli, S. Hermsmeyer, P. Norajitra, N. Taylor, and D. Ward, "Evaluation of temperature fluctuations influence in the structure of tokamak-reactor liquid metal blanket module." *EFDA*, vol. 1, pp. 1–212, 2005.

[9] O. Zikanov, Y. Listratov, N. Razuvanov, I. Belyaev, P. Frick, and V. Sviridov, "Mixed convection in pipe and duct flows with strong magnetic fields," *Appl. Mech. Rev.*, vol. 73, no. 1, p. 010801, 2021.

[10] R. J. Moreau, *Magnetohydrodynamics*. Dordrecht, Netherlands: Springer, 1990.

[11] H. Branover, *Magnetohydrodynamic Flow in Ducts*. New York, NY, USA: Wiley, 1978.

[12] P. Kirillov, *Thermophysical properties of materials for nuclear engineering*. Moscow, Russia: IzdAT, 2007.

[13] D. Krasnov, O. Zikanov, and T. Boeck, "Comparative study of finite difference approaches to simulation of magnetohydrodynamic turbulence at low magnetic Reynolds number," *Comp. Fluids*, vol. 50, pp. 46–59, 2011.

[14] ——, "Numerical study of magnetohydrodynamic duct flow at high Reynolds and Hartmann numbers," *J. Fluid Mech.*, vol. 704, pp. 421–446, 2012.

[15] Y. Zhao and O. Zikanov, "Instabilities and turbulence in magnetohydrodynamic flow in a toroidal duct prior to transition in Hartmann layers," *J. Fluid Mech.*, vol. 692, pp. 288–316, 2012.

[16] O. Zikanov, Y. Listratov, and V. G. Sviridov, "Natural convection in horizontal pipe flow with strong transverse magnetic field," *J. Fluid Mech.*, vol. 720, pp. 486–516, 2013.

[17] X. Zhang and O. Zikanov, "Mixed convection in a horizontal duct with bottom heating and strong transverse magnetic field," *J. Fluid Mech.*, vol. 757, pp. 33–56, 2014.

[18] ——, "Convection instability in a downward flow in a vertical duct with strong transverse magnetic field," *Phys. Fluids*, vol. 30, p. 117101, 2018.

[19] A. Y. Gelfgat and O. Zikanov, "Computational modeling of magnetoconvection: effects of discretization method, grid refinement and grid stretching," *Comp. Fluids*, vol. 175, pp. 66–82, 2018.

[20] M.-J. Ni, R. Munipalli, P. Huang, N. B. Morley, and M. A. Abdou, "A current density conservative scheme for incompressible MHD flows at a low magnetic Reynolds number. Part I: On a rectangular collocated grid system," *J. Comp. Phys.*, vol. 227, pp. 174–204, 2007.

[21] J. Sommeria and R. Moreau, "Why, how and when MHD-turbulence becomes two-dimensional," *J. Fluid Mech.*, vol. 118, pp. 507–518, 1982.

[22] O. Zikanov, *Essential Computational Fluid Dynamics*, 2nd ed. Hobooken, NJ, USA: Wiley, 2019.

[23] K. Moffatt, "On the suppression of turbulence by a uniform magnetic field." *J. Fluid Mech.*, vol. 23, pp. 571–592, 1967.

[24] O. Zikanov and A. Thess, "Direct numerical simulation of forced MHD turbulence at low magnetic Reynolds number," *J. Fluid Mech.*, vol. 358, p. 299–333, 1998.

[25] A. Vorobev, O. Zikanov, P. A. Davidson, and B. Knaepen, "Numerical study of the instability of the Hartmann layer," *Phys. Fluids.*, vol. 17, no. 12, p. 125105, 2005.

[26] W. Liu, D. Krasnov, and J. Schumacher, "Wall modes in magnetoconvection at high Hartmann numbers," *J. Fluid Mech.*, vol. 849, p. R2, 2018.

[27] M. Yan, M. A. Calkins, S. Maffei, K. Julien, S. M. Tobias, and P. Marti, "Heat transfer and flow regimes in quasi-static magnetoconvection with a vertical magnetic field," *J. Fluid Mech.*, vol. 877, pp. 1186–1206, 2019.

[28] R. Akhmedagaev, O. Zikanov, D. Krasnov, and J. Schumacher, "Rayleigh-Bénard convection in strong vertical magnetic field: flow structure and verification of numerical method," *Magnetohydrodynamics*, vol. 56, no. 2/3, pp. 157–166, 2020.

[29] ——, "Turbulent Rayleigh-Bénard convection in a strong vertical magnetic field," *J. Fluid Mech.*, vol. 895, p. R4, 2020.

[30] Y. Nakagawa, "Experiments on the inhibition of thermal convection by a magnetic field," *Proc. R. Soc. London*, vol. 240, no. 1220, pp. 108–113, 1957.

[31] S. Cioni, S. Chaumat, and J. Sommeria, "Effect of a vertical magnetic field on turbulent Rayleigh-Bénard convection," *Phys. Rev. Lett.*, vol. 62, no. 4, 2000.

[32] J. M. Aurnou and P. L. Olson, "Experiments on Rayleigh–Bénard convection, magnetoconvection and rotating magnetoconvection in liquid gallium," *J. Fluid Mech.*, vol. 430, pp. 283–307, 2001.

[33] U. Burr and U. Müller, "Rayleigh–Bénard convection in liquid metal layers under the influence of a vertical magnetic field," *Phys. Fluids*, vol. 13, no. 11, p. 3247, 2001.

[34] E. M. King and J. M. Aurnou, "Magnetostrophic balance as the optimal state for turbulent magnetoconvection," *Proc. Natl. Acad. Sci. USA*, vol. 112, no. 4, pp. 990–994, 2015.

[35] T. Zürner, F. Schindler, T. Vogt, S. Eckert, and J. Schumacher, "Flow regimes of Rayleigh-Bénard convection in a vertical magnetic field," *J. Fluid Mech.*, vol. 894, p. A1, 2020.

[36] S. Chandrasekhar, *Hydrodynamic and hydromagnetic stability*. New York, NY, USA: Dover Publications, 1961.

[37] B. C. Houchens, L. M. Witkowski, and J. S. Walker, "Rayleigh–Bénard instability in a vertical cylinder with a vertical magnetic field," *J. Fluid Mech.*, vol. 469, pp. 189–207, 2002.

[38] F. H. Busse, "Asymptotic theory of wall-attached convection in a horizontal fluid layer with a vertical magnetic field," *Phys. Fluids*, vol. 20, no. 2, p. 024102, 2008.

[39] T. Zürner, F. Schindler, T. Vogt, S. Eckert, and J. Schumacher, "Combined measurement of velocity and temperature in liquid metal convection," *J. Fluid Mech.*, vol. 876, pp. 1108–1128, 2019.

[40] R. Verzicco and R. Camussi, "Transitional regimes of low-Prandtl thermal convection in a cylindrical cell," *Phys. Fluids*, vol. 9, no. 5, pp. 1287–1295, 1997.

[41] R. H. T., "A study of Benard convection with and without rotation," *J. Fluid Mech.*, vol. 36, pp. 309–335, 1969.

[42] F. Zhong, R. Ecke, and V. Steinberg, "Asymmetric modes and the transition to vortex structures in rotating Rayleigh-Bénard convection," *Phys. Rev. Lett.*, vol. 67, no. 18, p. 2473, 1991.

[43] R. Ecke, F. Zhong, and E. Knobloch, "Hopf bifurcation with broken reflection symmetry in rotating Rayleigh-Bénard convection," *Europhys. Lett.*, vol. 19, no. 3, pp. 177–182, 1992.

[44] X. Zhang, D. P. M. van Gils, S. Horn, M. Wedi, L. Zwirner, G. Ahlers, R. E. Ecke, S. Weiss, E. Bodenschatz, and O. Shishkina, "Boundary zonal flow in rotating turbulent Rayleigh-Bénard convection," *Phys. Rev. Lett.*, vol. 124, p. 084505, 2020.

[45] Z. L. Lim, K. L. Chong, G. Ding, and K. Xia, "Quasistatic magnetoconvection: heat transport enhancement and boundary layer crossing," *J. Fluid Mech.*, vol. 870, pp. 519–542, 2019.

[46] J. D. Scheel and J. Schumacher, "Global and local statistics in turbulent convection at low Prandtl numbers," *J. Fluid Mech.*, vol. 802, pp. 147–173, 2016.

[47] X. Zhang and O. Zikanov, "Two-dimensional turbulent convection in a toroidal duct of a liquid metal blanket of a fusion reactor," *J. Fluid Mech.*, vol. 779, pp. 36–52, 2015.

[48] X. Lv and O. Zikanov, "Mixed convection in horizontal duct flow with transverse magnetic field and heating of side wall," *Phys. Fluids*, vol. 26, no. 9, p. 097106, 2014.

[49] S. Grossmann and D. Lohse, "Thermal convection for large Prandtl numbers," *Phys. Rev. Lett.*, vol. 86, p. 3316, 2001.

[50] E. M. King and J. M. Aurnou, "Turbulent convection in liquid metal with and without rotation," *Proc. Natl. Acad. Sci. USA*, vol. 110, no. 17, pp. 6688–6693, 2013.

[51] J. D. Scheel and J. Schumacher, "Predicting transition ranges to fully turbulent viscous boundary layers in low Prandtl number convection flows," *Phys. Rev. Fluids*, vol. 2, no. 12, p. 123501, 2017.

[52] J. A. Glazier, T. Segawa, A. Naert, and M. Sano, "Evidence against 'ultrahard' thermal turbulence at very high Rayleigh numbers," *Nature*, vol. 398, pp. 307–310, 1999.

[53] T. Takeshita, T. Segawa, J. A. Glazier, and M. Sano, "Thermal Turbulence in Mercury," *Phys. Rev. Lett.*, vol. 76, no. 9, pp. 1465–1468, 1996.

[54] R. Akhmedagaev, O. Zikanov, and Y. Listratov, "Magnetoconvection in a horizontal duct flow at very high Hartmann and Grashof numbers," *J. Fluid Mech.*, vol. 931, p. A29, 2022.

[55] I. Belyaev, P. Sardov, I. Melnikov, and P. Frick, "Limits of strong magneto-convective fluctuations in liquid metal flow in a heated vertical pipe affected by a transverse magnetic field," *Int. J. Therm. Sci.*, vol. 101, p. 106773, 2021.

[56] I. Belyaev, I. Poddubnyi, N. Razuvanov, and V. Sviridov, "Evaluation of temperature fluctuations influence in the structure of tokamak-reactor liquid metal blanket module." *PAST*, vol. 41, no. 1, pp. 41–52, 2018.

[57] A. Kolmakov, V. Terent'ev, D. Prosvirnin, V. Chernov, and M. Leont'eva-Smirnova, "Fatigue strength of low-activation ferritic–martensitic high-chromium ek-181 steel." *Russ. Metall.*, vol. 2016, pp. 394–398, 2016.

[58] I. Kirillov and E. Muraviev, "Review of liquid metal divertor concepts for tokomak reactors," *Fusion Technology 1996*, pp. 251–254, 1997.

[59] L. G. Genin, V. G. Zhilin, Y. P. Ivochkin, N. G. Razuvanov, I. A. Belyaev, Y. I. Listratov, and V. G. Sviridov, "Temperature fluctuations in a heated horizontal tube affected by transverse magnetic field," in *Proc.* 8^{th} *PAMIR Conf. Fund. Appl. MHD*, Borgo, Corsica, France, 2011, pp. 37–41.

[60] I. Belyaev, Y. P. Ivochkin, Y. I. Listratov, N. Razuvanov, and V. Sviridov, "Temperature fluctuations in a liquid metal MHD-flow in a horizontal inhomogeneously heated tube," *High Temp.*, vol. 53, no. 5, pp. 734–741, 2015.

[61] S. Sahu, C. Courtessole, A. Ranjan, R. Bhattacharyay, T. Sketchley, and S. Smolentsev, "Thermal convection studies in liquid metal flow inside a horizontal duct under the influence of transverse magnetic field," *Phys. Fluids*, vol. 32, no. 6, p. 067107, 2020.

[62] T. Vo, A. Pothérat, and G. J. Sheard, "Linear stability of horizontal, laminar fully developed, quasi-two-dimensional liquid metal duct flow under a transverse magnetic field and heated from below," *Phys. Rev. Fluids*, vol. 2, p. 033902, 2017.

[63] Y. I. Listratov, D. Ognerubov, O. Zikanov, and V. Sviridov, "Numerical simulations of mixed convection in liquid metal flow within a horizontal pipe with transverse magnetic field," *Fluid Dyn. Res.*, vol. 50, no. 5, p. 051407, 2018.

[64] S. Smolentsev, R. Moreau, and M. Abdou, "Characterization of key magnetohydrodynamic phenomena for PbLi flows for the US DCLL blanket," *Fusion Eng. Des.*, vol. 83, pp. 771–783, 2008.

[65] S. Smolentsev, R. Moreau, L. Bühler, and C. Mistrangelo, "MHD thermofluid issues of liquid-metal blankets: Phenomena and advances," *Fusion Eng. Des.*, vol. 85, no. 7-9, pp. 1196–1205, 2010.

[66] I. A. Belyaev, V. G. Sviridov, V. M. Batenin, D. A. Biryukov, I. S. Nikitina, S. P. Manchkha, N. Y. Pyatnitskaya, N. G. Razuvanov, and E. V. Sviridov, "Test facility for investigation of heat transfer of promising coolants for the nuclear power industry," *Therm. Eng.*, vol. 64, no. 11, pp. 841–848, 2017.

[67] T. Alboussière, J. P. Garandet, and R. Moreau, "Buoyancy-driven convection with a uniform magnetic field. Part 1. Asymptotic analysis," *J. Comp. Phys.*, vol. 253, pp. 545–563, 1993.

[68] T. P. Lyubimova, D. V. Lyubimov, V. A. Morozov, R. V. Scuridin, H. B. Hadid, and D. Henry, "Stability of convection in a horizontal channel subjected to a longitudinal temperature gradient. Part 1. Effect of aspect ratio and Prandtl number," *J. Comp. Phys.*, vol. 2009, pp. 275–296, 2009.

[69] X. Zhang and O. Zikanov, "Thermal convection in a toroidal duct of a liquid metal blanket. Part II. Effect of axial mean flow," *Fusion Eng. Des.*, vol. 116, pp. 40–46, 2017.

[70] A. Pothérat, J. Sommeria, and R. Moreau, "An effective two-dimensional model for MHD flows with transverse magnetic field," *J. Fluid Mech.*, vol. 424, pp. 75–100, 2000.

[71] ——, "Numerical simulations of an effective two-dimensional model for flows with a transverse magnetic field," *J. Fluid Mech.*, vol. 534, pp. 155–143, 2005.

[72] A. Pothérat, "Numerical simulations of an effective two-dimensional model for flows with a transverse magnetic field," *Phys. Fluids*, vol. 19, no. 7, p. 074104, 2007.

[73] S. Smolentsev, N. Vetcha, and R. Moreau, "Study of instabilities and transitions for a family of quasi-two-dimensional magnetohydrodynamic flows based on a parametrical model," *Phys. Fluids*, vol. 24, p. 024101, 2012.

[74] N. Vetcha, S. Smolentsev, M. Abdou, and R. Moreau, "Study of instabilities and quasi-two-dimensional turbulence in volumetrically heated magnetohydrodynamic flows in a vertical rectangular duct," *Phys. Fluids*, vol. 25, no. 2, p. 024102, 2013.

[75] A. Y. Gelfgat and S. Molokov, "Quasi-two-dimensional convection in a three-dimensional laterally heated box in a strong magnetic field normal to main circulation," *Phys. Fluids*, vol. 23, p. 034101, 2011.

[76] A. Pothérat and R. Klein, "Why, how and when MHD turbulence at low rm becomes three-dimensional," *J. Fluid Mech.*, vol. 761, pp. 168–205, 2014.

[77] ——, "Do magnetic fields enhance turbulence at low magnetic reynolds number?" *Phys. Rev. Fluids*, vol. 2, p. 063702, 2017.

[78] K. Taira, S. L. Brunton, S. T. M. Dawson, C. W. Rowley, T. Colonius, B. J. McKeon, O. T. Schmidt, S. Gordeyev, V. Theofilis, and L. S. Ukeiley, "Modal analysis of fluid flows: An overview." *AIAA Journal*, vol. 55, no. 12, pp. 4013–4041, 2017.

[79] K. Taira, M. S. Hemati, S. L. Brunton, Y. Sun, K. Duraisamy, S. Bagheri, S. T. M. Dawson, and C. Yeh, "Modal analysis of fluid flows: Applications and outlook." *AIAA Journal*, vol. 58, no. 3, pp. 998–1022, 2020.

[80] D. Canuto and K. Taira, "Two-dimensional compressible viscous flow around a circular cylinder." *J. Fluid Mech.*, vol. 785, pp. 349–371, 2015.

[81] L. Rosenhead and H. Jeffreys, "The formation of vortices from a surface of discontinuity," *Proc. R. Soc. London*, vol. 134, no. 823, pp. 170–192, 1931.

[82] M. Melander, N. Zabusky, and J. Mcwilliams, "Symmetric vortex merger in two dimensions: Causes and conditions." *J. Fluid Mech.*, vol. 195, pp. 303–340, 1988.

[83] L. Soucasse, B. Podvin, P. Riviére, and A. Soufiani, "Proper orthogonal decomposition analysis and modelling of large-scale flow reorientations in a cubic Rayleigh–Bénard cell." *J. Fluid Mech.*, vol. 881, pp. 23–50, 2019.

[84] L. Abreu, A. Cavalieri, P. Schlatter, R. Vinuesa, and D. Henningson, "Spectral proper orthogonal decomposition and resolvent analysis of near-wall coherent structures in turbulent pipe flows." *J. Fluid Mech.*, vol. 900, p. A11, 2020.

[85] S. E. Ahmed, O. San, A. Rasheed, and T. Iliescu, "Nonlinear proper orthogonal decomposition for convection-dominated flows." *Phys. Fluids.*, vol. 33, p. 121702, 2021.

[86] R. S. Reichert, F. F. Hatay, S. Biringen, and A. Huser, "Proper orthogonal decomposition applied to turbulent flow in a square duct." *Phys. Fluids.*, vol. 6, pp. 3086–3092, 1994.

[87] L. H. O. Hellström and A. J. Smits, "Structure identification in pipe flow using proper orthogonal decomposition." *Phil. Trans. R. Soc. A*, vol. 375, no. 2089, p. 20160086, 2017.

[88] K. Karhunen, "Zur spektraltheorie stochasticher prozesse." *Annales Academiae Scientiarum Fennicae*, vol. 37, pp. 1–7, 1987.

[89] M. Loéve, *Probability Theory*. Princeton, NJ, USA: Princeton, 1955.

[90] J. L. Lumley, "The structure of inhomogeneous turbulence." *Proceedings of the International Colloquium on the Fine Scale Structure of the Atmosphere and Its Influence on Radio Wave Propagation*, 1967.

[91] G. Berkooz, P. Holmes, and J. L. Lumley, "The proper orthogonal decomposition in the analysis of turbulent flows." *Annual Review of Fluid Mechanics*, vol. 25, no. 1, pp. 539–575, 1993.

[92] L. Sirovich, "Turbulence and the dynamics of coherent structures, Parts I–III." *Quart. Appl. Math.*, vol. 45, no. 3, pp. 561–571, 1987.

[93] J. Weiss, "A tutorial on the proper orthogonal decomposition." *American Institute of Aeronautics and Astronautics*, pp. AIAA 2019–3333, 2019.

[94] N. Aubry, P. Holmes, J. L. Lumley, and E. Stone, "The dynamics of coherent structures in the wall region of a turbulent boundary layer." *J. Fluid Mech.*, vol. 192, pp. 115–173, 1988.

[95] B. R. Noack, P. Papas, and P. A. Monkewitz, "The need for a pressure-term representation in empirical Galerkin models of incompressible shear flows." *J. Fluid Mech.*, vol. 523, pp. 339–365, 2005.

[96] J. L. Lumley, *Stochastic Tools in Turbulence*. Cambridge, MA, USA: Academic Press, 1970.

[97] C. W. Rowley, "Model reduction for fluids using Balanced Proper Orthogonal Decomposition." *International Journal of Bifurcation and Chaos*, vol. 15, no. 3, pp. 997–1013, 2005.

[98] P. J. Schmid, "Dynamic mode decomposition of numerical and experimental data." *J. Fluid Mech.*, vol. 656, pp. 5–28, 2010.